Method for Measuring CP Violation in Top Quark Pair Production at ATLAS

by

Fredric Kalen Martens

A thesis submitted in conformity with the requirements
for the degree of Doctor of Philosophy
Graduate Department of Physics
University of Toronto

Abstract

Method for Measuring CP Violation in Top Quark Pair Production at ATLAS

Fredric Kalen Martens

Doctor of Philosophy

Graduate Department of Physics

University of Toronto

2007

The Standard Model (SM) predicts that a large fraction of top quark pairs produced in 14 TeV center-of-mass pp collisions will have correlated helicities, and the number of $t_L\bar{t}_L$ and $t_R\bar{t}_R$ pairs produced will be approximately equal. Unequal numbers of these pairs are an indication that CP symmetry is violated and there is new physics beyond the Standard Model. A method to measure CP violation in $t\bar{t}$ pair production at the Large Hadron Collider is presented. In particular, the value of $\Delta N_{LR} = [\sigma(t_L\bar{t}_L) - \sigma(t_R\bar{t}_R)]/\sigma(t\bar{t})_{TOT}$ is found to be best measured in the lepton-plus-jets channel of $t\bar{t}$ decay. In this channel, the top pair can be reconstructed and the angular distribution of the leptons with respect to the top quark momentum can be determined. The ATLAS experiment can measure ΔN_{LR} with a statistical uncertainty on the order of 1.5% after only 30 fb^{-1} integrated luminosity. The sources of a number of systematic uncertainties were also studied. A method to detect CP violation in the dimuon decay channel using the p_T asymmetry of oppositely charged muons was also investigated.

For my family and friends.

Contents

Chapter 1

Introduction

The field of particle physics is the study of the smallest particles in the universe, as well as the interactions between these particles. Much has been accomplished in the last century starting around the time when E. Rutherford determined in 1911 that the atom consists of a very small, positively charged nucleus surrounded by a cloud of negatively charged electrons [1]. Electrons were discovered fourteen years earlier by J.J. Thomson [2]. While experiments have shown that electrons are small enough to be considered as point-like objects, that is, not made of smaller particles, we now know that atomic nuclei are composed of protons and neutrons, which in turn are composed of point-like particles called quarks.

Much of this progress is due to advances in particle accelerator technology for two reasons. First, higher energy particle beams mean that matter can be probed at smaller distance scales since a particle's wavelength λ is inversely proportional to its momentum p according to the de Broglie relation,

$$\lambda = \frac{h}{p}, \tag{1.1}$$

where h is Planck's constant. Second, particles can be created in particle collisions if enough energy is available in the center-of-momentum frame. To create a particle of

mass, m, the amount of energy, E, needed to create it is given by

$$E = mc^2, \tag{1.2}$$

where c is the speed of light.

Examining cosmic ray showers and using accelerators to collide particles together at high energy, physicists discovered a wide variety of particles: heavier versions of the electron, and particles with properties that could not be immediately explained. A theory was needed to explain the relationships between the newly discovered particles and the strength of their interactions. Such a theory finally emerged in the 1970's after decades of effort by many people.

1.1 Standard Model

As technology progressed, experimentalists and theorists worked together to develop physical models and test their predictions. The result is a very successful theory known as the Standard Model, which does not contradict current experimental results.

The fundamental particles of the SM are considered as point-like and have no sub-structure. Properties of these particles include mass, charge, and an intrinsic angular momentum known as *spin*. These particles can have either integer or half-integer values of spin in units of $\hbar$. Particles with half-integer spin are known as fermions, and those with integer spin are known as bosons.

Table 1.1 lists all of the spin-1/2 particles in the Standard Model. Each particle belongs to one of three generations. Virtually all of the matter that we find in the universe is made of the quarks and leptons found in the first generation. Particles in the second and third generations are progressively more massive and can be created in collisions if enough energy is available. However, they do not exist for very long and eventually decay back into first generation particles.

Gener-	Quarks			Leptons		
ation	Symbol	Name	Charge	Symbol	Name	Charge
1	u	up	$+2/3e$	e	electron	-1e
	d	down	-1/3e	ν_e	electron neutrino	0
2	c	charm	$+2/3e$	μ	muon	-1e
	s	strange	-1/3e	ν_μ	muon neutrino	0
3	t	top	$+2/3e$	τ	tau	-1e
	b	bottom	-1/3e	ν_τ	tau neutrino	0

Table 1.1: The fermions of the Standard Model. Every particle listed here has spin-1/2 and has a corresponding antiparticle.

The Lagrangian density $\mathcal{L}_{\text{Dirac}}$ that describes the propagation of a free fermion of mass m is given by[1]

$$\mathcal{L}_{\text{Dirac}} = i\bar{\psi}\gamma^\mu\partial_\mu\psi - m\bar{\psi}\psi, \tag{1.3}$$

where ψ is a spinor describing the fermion field, $\bar{\psi}$ is the adjoint spinor and the γ^μ are the Dirac matrices. The Dirac equation,

$$(i\gamma^\mu\partial_\mu - m)\psi = 0, \tag{1.4}$$

is the equation of motion of the fermion field which results from applying the Euler-Lagrange equations to $\mathcal{L}_{\text{Dirac}}$.

Fields that represent particles that mediate forces between fermions arise when $\mathcal{L}_{\text{Dirac}}$ is required to be invariant under certain local transformations of the field ψ. For example, under a local U(1) transformation,

[1]The convention that $\hbar = 1$ and $c = 1$ will be used.

$$\psi \rightarrow \psi' = \exp^{i\Lambda(x)}\,\psi, \tag{1.5}$$

a single vector field, A_μ, is needed, and a term equal to $-q\psi\gamma^\mu\bar{\psi}A_\mu$ must be added to $\mathcal{L}_{\text{Dirac}}$, where A_μ transforms as

$$A_\mu \rightarrow A'_\mu = A_\mu + \frac{1}{q}\partial_\mu\Lambda(x). \tag{1.6}$$

The added term represents the interaction between the fermion and the A_μ field, and q is a real number that indicates the strength of the interaction. The locally invariant Dirac Lagrangian density is then given by the original Lagrangian density describing the propagation of a free fermion, the interaction term, plus a term describing the propagation of the free vector field. The new Lagrangian is written as

$$\mathcal{L}_{\text{Dirac}} = i\bar{\psi}\gamma^\mu\partial_\mu\psi - m\bar{\psi}\psi - q\bar{\psi}\gamma^\mu\psi A_\mu - \frac{1}{16\pi}F^{\mu\nu}F_{\mu\nu}, \tag{1.7}$$

where $F^{\mu\nu} = \partial^\mu A^\nu - \partial^\nu A^\mu$. The third term describes the propagation of a massless spin-1 particle. The Lagrangian density can be written more simply as

$$\mathcal{L}_{\text{Dirac}} = i\bar{\psi}\gamma^\mu\mathcal{D}_\mu\psi - m\bar{\psi}\psi - \frac{1}{16\pi}F^{\mu\nu}F_{\mu\nu}, \tag{1.8}$$

where $\mathcal{D}_\mu$ is given by

$$\mathcal{D}_\mu = \partial_\mu + iqA_\mu. \tag{1.9}$$

For this local U(1) transformation, A_μ represents the spin-1 particle known as the photon which is the mediator for the electromagnetic force. The parameter, q, is the electric charge of the fermion. When ψ represents an electron, the new $\mathcal{L}_{\text{Dirac}}$ is the Lagrangian density that describes the theory of quantum electrodynamics. The U(1) transformation is an example of what is commonly referred to as a *gauge transformation.* The particle or particles that are required for local invariance are called *gauge bosons.*

The theory of the strong force also requires the original $\mathcal{L}_{\text{Dirac}}$ to be invariant under local SU(3) gauge transformations. The resulting theory, known as quantum chromodynamics (QCD), has 8 spin-1 particles that correspond to mediators of the strong force and are called gluons. The Lagrangian density of the gauge invariant field is

$$\mathcal{L}_{\text{QCD}} = \bar{\psi}(i\gamma^\mu \partial_\mu - m)\psi - \alpha_s(\bar{\psi}\gamma^\mu T_a \psi)G_\mu^a - \frac{1}{4}G_\mu^a \nu G_a^\mu \nu \tag{1.10}$$

where α_s is the strong coupling constant, G_μ^a $(a = 1, 2...8)$ are the gluons, T^a are the generators of SU(3), and

$$G_\mu^a \nu = \partial_\mu G_\nu^a - \partial_\nu G_\mu^a - \frac{1}{4}\alpha_s f_{abc} G_\mu^b G_\nu^c. \tag{1.11}$$

In addition to electric charge, quarks have a different kind of charge as a result of the SU(3) symmetry. Quarks can have one of three charges commonly called colour charge and are referred to as red, blue and green. Anti-quarks have the corresponding anti-colour charge. No experiment has seen a free quark, or particle with a net colour charge. Only particles that are colour singlets have been observed: quarks are confined in bound states where there is no overall colour charge. The property of QCD that accounts for this behavior is known as asymptotic freedom [3, 4], which means that the strong force gets weaker at shorter distance scales, and stronger at larger distance scales. As a consequence, three quarks each with a different colour can form a bound state (qqq) known as a *baryon*, and three anti-quarks, each with a different anti-colour, can form an *anti-baryon* ($\bar{q}\bar{q}\bar{q}$). A coloured quark and an anti-quark with the corresponding anti-colour can also form a bound state ($q\bar{q}$) called a *meson*. The baryons and mesons are collectively known as *hadrons*.

If a quark gets enough energy to leave a hadron, enough energy is available to create a quark—anti-quark pair due to asymptotic freedom. The new anti-quark joins with the outgoing quark to form a meson, and the new quark replaces the missing quark in the hadron.

For $\mathcal{L}_{\text{Dirac}}$ to be invariant under a local SU(2) transformation, 3 massless spin-1 particles B_i^μ $(i = 1, 2, 3)$ are required. These cannot represent the weak bosons, W^+, W^-, and Z^0, because they are known to have non-zero mass. To address this problem, the electroweak theory [5, 6, 7] was developed which unifies descriptions of the electromagnetic and weak interactions into a single theory. To accomplish this, a complex doublet of scalar fields is added to the SU(2)×U(1) theory. The Lagrangian density for this field ϕ is given by

$$\mathcal{L}_{\text{KG}} = \frac{1}{2}(\mathcal{D}_\mu\phi)^\dagger(\mathcal{D}^\mu\phi) - V(\phi^\dagger\phi), \tag{1.12}$$

where

$$\mathcal{D}_\mu = \partial_\mu + \frac{ig'}{2}\mathcal{A}_\mu + \frac{ig}{2}\vec{\sigma}\vec{B}_\mu, \tag{1.13}$$

$\mathcal{A}$ is the U(1) field, and $\vec{\sigma}$ are the Pauli matrices. The potential is given by

$$V(\phi^\dagger\phi) = \mu^2(\phi^\dagger\phi) + |\lambda|(\phi^\dagger\phi)^2. \tag{1.14}$$

This Lagrangian density retains the U(1)×SU(2) symmetry. If $\mu^2 < 0$, the potential no longer has a minimum at zero and the U(1)×SU(2) symmetry of the vacuum is broken. The vacuum expectation value of the scalar field can be chosen as

$$\langle\phi\rangle = \begin{pmatrix} 0 \\ v/\sqrt{2} \end{pmatrix} \tag{1.15}$$

where $v = \sqrt{-\mu^2/|\lambda|}$. Expanding the Lagrangian about the vacuum state, the scalar field acquires a mass of $-\mu^2 > 0$ and is known as the Higgs boson [8]. When the U(1) and SU(2) gauge fields, $\mathcal{A}_m u$ and B_μ^i, are mixed, the resulting particle spectrum has the three massive gauge bosons $(W_\mu^+, W_\mu^-, Z_\mu^0)$ and the massless photon $(A_m u)$ that are observed in nature.

Force	Carrier	Relative Strength
Strong	gluon (g)	1
Electromagnetic	photon (γ)	10^{-2}
Weak	W^+,W^-,Z^0	10^{-13}
Gravitational	graviton	10^{-38}

Table 1.2: The gauge bosons that mediate the strong, weak and electromagnetic interactions between the particles in the Standard Model. The gravitational force is included to show the relative strengths of all four forces in nature. The relative strengths listed are approximate because they are dependent on the energy of the interaction and the particles involved.

The forces of the Standard Model and their relative strengths are summarized in Table 1.2. Gravity is not included in the SM and is rather weak, but is included for comparison.

1.2 CP Violation in the Standard Model

The weak force violates parity, P, a symmetry that reverses all three spatial coordinates. It does so to the maximal degree and was first experimentally seen in 1956 [9]. Parity violation is observed because the bosons that carry the weak force couple only to left-handed fermions; that is, to fermions with their spin in the opposite direction of their momentum vector. The charge conjugation operator, C, changes a particle to its corresponding antiparticle. When the charge conjugation and parity operations are combined, it is found that C and P together are a good, but not perfect, symmetry for the weak interactions.

The first experiment to show CP violation was performed in 1964 using beams of neutral, strange-flavoured mesons called kaons [10]. CP violation has now been observed

in B-mesons, as well [11, 12].

In the Standard Model, CP violation can be explained with the Cabibbo-Kobayashi-Masakwa (CKM) matrix [13, 14] which mixes the mass eigenstates of the quarks (d,s,b) found in Table 1.1 with the weak eigenstates (d',s',b'):

$$\begin{pmatrix} d' \\ s' \\ b' \end{pmatrix} = \begin{pmatrix} V_{ud} & V_{us} & V_{ub} \\ V_{cd} & V_{cs} & V_{cb} \\ V_{td} & V_{ts} & V_{tb} \end{pmatrix} \begin{pmatrix} d \\ s \\ b \end{pmatrix}. \tag{1.16}$$

Since this is a 3x3 matrix, there is a single complex phase that cannot be removed by a redefinition of the fields. The complex phase is non-zero and explains all of the results seen in the kaon and B-meson data. CP violation is not otherwise seen in particle physics experiments at the present time.

The Standard Model predicts, however, that CP symmetry is violated in the strong interactions. The QCD Lagrangian density has a CP violating term that must be introduced in order to solve what is known as the U(1)$_A$ problem [15]:

$$\mathcal{L}_{QCD}^{eff} = \mathcal{L}_{QCD} + \frac{\Theta\alpha^2}{32\pi^2}\epsilon^{\mu\nu\sigma\lambda}G_{a\mu\nu}G^a_{\sigma\lambda}. \tag{1.17}$$

The variable, Θ, is a parameter that gives the degree of CP violation in QCD. However, CP has been seen experimentally to be a good symmetry of the strong interaction, so Θ must be zero or very close to zero. The most sensitive test is the measurement of the neutron electric dipole moment, which has a limit of $|d_n| < 6.3\times10^{-26}$ e·cm [16]. The corresponding limit on the theta parameter is $\Theta < 5 \times 10^{-10}$ [17].

The incredibly small value of Θ is hard to explain. There is no known reason why it should be so small. This is known as the "strong CP problem". One solution to this dilemma was proposed that introduces a new particle called the axion [18]. Axions, if they exist, interact very weakly and experiments are searching for this hypothetical particle [19].

Popular extensions to the Standard Model introduce additional particles and couplings. If these coupling are complex, then additional ways for CP violation to occur are possible. In some cases, it might be possible to discover new physics first through measurements of CP violation, rather than direct observation of new particles. Considering the interesting possibilities concerning CP violation, it makes sense to look for it in different processes in the search for physics beyond the Standard Model.

1.3 Large Hadron Collider

The Large Hadron Collider (LHC) [20, 21, 22, 23] is being assembled in the tunnel that held the Large Electron-Positron collider (LEP). The LHC will provide pp collisions at an energy of 14 TeV in the center-of-mass frame with high luminosity. The LHC is expected to produce the first collisions in 2007, but will initially be running at a fraction of its design luminosity.

The most interesting physics come from parton–parton collisions with a large momentum transfer. In this case, the outgoing particles can have a large transverse momentum with respect to the beam axis.

The high luminosity and large energy of the Large Hadron Collider (LHC) will result in the annual production of $\sim 8 \times 10^7$ $t\bar{t}$ quark pairs. Even with the large backgrounds to the $t\bar{t}$ signal, the LHC can be considered as a top factory.

1.4 CP Violation and Top Pair Production

The most recent discovery of a Standard Model particle is that of the top quark at the Tevatron. The CDF and DØ collaborations announced their results in 1995 [24, 25]. The Tevatron remains currently the only place where the top quark is produced and studied.

The current world average of the top quark mass is 172.5 ± 2.3 GeV/c^2 [26]. The top has $Q = +2/3$ and, along with the bottom quark ($Q = -1/3$), form the third generation

of quarks in the Standard Model. The large mass of the top has important consequences for the properties of other particles. For example, the radiative corrections from top quark loops affect the masses of other particles. Indeed, these corrections are used to constrain the mass of the undiscovered Higgs boson. The large mass of the top quark is also close to the electroweak symmetry breaking scale which makes it an ideal candidate to study for obtaining clues if there is new physics beyond the Standard Model.

The helicity, h, of a particle is the projection of its spin angular momentum, $\vec{S}$, onto its momentum, $\vec{p}$. That is,

$$h = \frac{\vec{S} \cdot \vec{p}}{|\vec{p}|}. \tag{1.18}$$

For spin-1/2 particles, h can equal either $+1/2$ or $-1/2$. It is common to describe particles as having right- or left-handed helicity, if $h = +1/2$ or $h = -1/2$, respectively.

Top pairs produced at the LHC will have correlated helicities ($t_R\bar{t}_R$ or $t_L\bar{t}_L$) approximately 70–80% of the time, where the subscripts R and L denote the helicity of the quark. QCD interactions, which are found experimentally to respect CP symmetry, are responsible for the production of $t\bar{t}$ pairs. Since the states $t_R\bar{t}_R$ and $t_L\bar{t}_L$ go into each other via a CP operation, it is expected that equal numbers of pairs with correlated helicities should be produced. The quantity usually defined to indicate a number asymmetry between $t_R\bar{t}_R$ and $t_L\bar{t}_L$ is

$$\Delta N_{LR} = \frac{\sigma(t_L\bar{t}_L) - \sigma(t_R\bar{t}_R)}{\sigma(t\bar{t})_{TOT}}. \tag{1.19}$$

Some extensions of the Standard Model allow for CP violation to occur in $t\bar{t}$ production.

Quarks cannot exist as free particles, but top quarks decay on a time scale much faster than hadronization can take place, so its helicity is unaffected during its lifetime. Therefore, the top helicity state can be analyzed from the properties of its daughters and that can be used in a measurement of CP violation.

The top quark decays into a b-quark and W almost 100% of the time. The b-quark

hadronizes and forms a jet and the W decays either leptonically, or hadronically into two jets. The decay of a $t\bar{t}$ pair can be classified by the decays of the two intermediate W bosons. The case where both Ws decay leptonically is known as the dilepton channel. The all-jets channel is the case where both Ws decay hadronically. The lepton-plus-jets channel is where one W decays leptonically and the other hadronically. Each of these decay channels has features that can be exploited to study top quark physics. The most useful of these will be the lepton-plus-jets channel because the $t\bar{t}$ pair can be reconstructed.

The ATLAS experiment is a general purpose detector being built to observe the pp collisions at the LHC. With large coverage in both tracking and calorimetry, ATLAS is designed to observe a large range of physics including the discovery the SM Higgs boson. It will also be one of two detectors that will measure or place a useful upper limit on ΔN_{LR} due to the large number of $t\bar{t}$ pairs produced at the LHC. Measurements made at a second detector at the LHC, the Compact Muon Solenoid (CMS), will complement the results found with ATLAS.

The ability of the ATLAS spectrometer to measure CP violation in top pair production is the subject of this thesis. The study is comprised chiefly of simulations and methods are presented to measure ΔN_{LR} in the dilepton and lepton-plus-jets channels.

The production of $t\bar{t}$ pairs including possible sources of CP violation is discussed in Chapter 2. The strategies proposed to measure ΔN_{LR} are also presented.

Chapter 3 gives a brief description of the ATLAS spectrometer, with emphasis on those systems that are important with respect to the measurement ΔN_{LR}.

Chapter 4 describes the software used for the generation and simulation of events in ATLAS. How sets of data were created with varying amounts of CP violation is also discussed.

Chapter 5 examines the detection of CP violation in the dilepton channel. In this channel, the asymmetry in the momentum of oppositely charged leptons can indicate that

$\Delta N_{LR} \neq 0$. The signal-to-background ratio for event selection cuts was investigated. The ability of the ATLAS spectrometer to detect the type of CP violation arising from the 2HDM model was examined.

The most useful results come from the lepton-plus-jets channel and are explored in Chapter 6. This channel benefits from higher statistics and much lower backgrounds than the dilepton channel. The $t\bar{t}$ system can be fully reconstructed which allows the angle of the lepton with respect to the top momentum to be determined for each event. A method is presented which uses the angular distributions of the leptons to find a value for ΔN_{LR}. A number of systematic effects are also considered.

A number of conclusions will be drawn in Chapter 7. It will be shown that this measurement of CP violation can be performed at ATLAS. At the very least, some useful upper limits on ΔN_{LR} can be made.

v

Chapter 2

Top Quark Pair Production and CP Violation

The production and decay of $t\bar{t}$ pairs are described in this chapter. The physics that could generate the CP violating signal of interest is also presented. The strategies to measure ΔN_{LR} are outlined at the end of the chapter with emphasis on a method that allows one to make a measurement as a function of $t\bar{t}$ center of mass energy, $\sqrt{s}$, in a model independent way.

2.1 Top Pair Production and Spin Correlation

The Large Hadron Collider (LHC) [20, 21, 22, 23] will have two 7 TeV proton beams circulating in opposite directions providing proton-proton collisions with an unprecedented center of mass energy of 14 TeV. At this energy, the cross section for top pair production is approximately 830 pb (NLO) [27]. The LHC will have a large luminosity (10^{34} cm^{-2}s^{-1}) and will effectively be a "top factory" with approximately 80 million top pairs produced each year.

Hard interactions between the partonic constituents of the protons create top quark pairs. Specifically, top pair production can be from gluon–gluon or quark–anti-quark

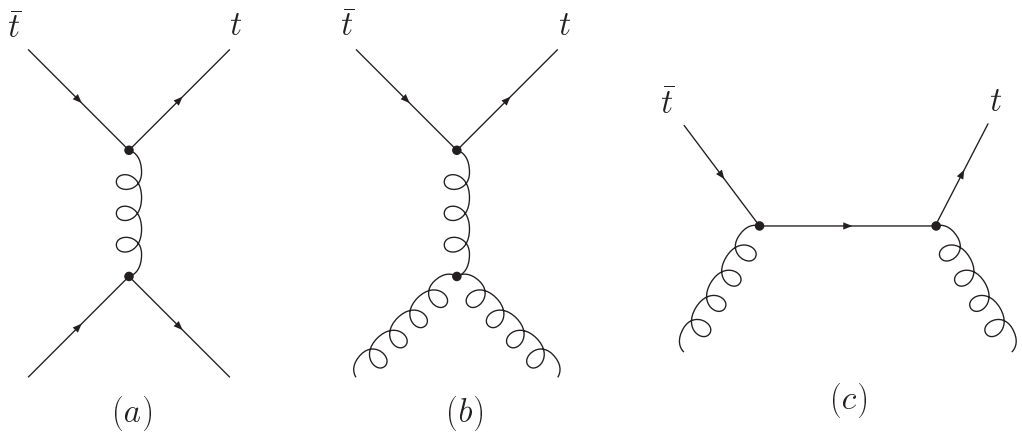

Figure 2.1: Tree level Feynman diagrams for $t\bar{t}$ production: (a) $q\bar{q} \to t\bar{t}$ and (b) and (c) $gg \to t\bar{t}$.

interactions. The tree level Feynman diagrams for top pair production are shown in Figure 2.1. The cross section for the $gg \to t\bar{t}$ process is approximately 90% of the total $t\bar{t}$ production cross-section at the LHC; the $q\bar{q} \to t\bar{t}$ process accounts for the remaining 10%. There is no CP violation at tree level, but it is a result of higher order diagrams or due to physics beyond the Standard Model.

At LHC energies, top pairs are also produced with their helicities highly correlated [28]. The dominant mechanism for top pair production is $gg \to t\bar{t}$ via a gluon in the s-channel. Near threshold, and assuming zero angular momentum of the $t\bar{t}$ pair, the t and $\bar{t}$ must be produced in a spin-1 state at threshold with $|S, S_z >= |1, 0 >$. The t and $\bar{t}$ travel in opposite directions in the CM frame so, if each has the opposite spin, they will have the same helicity. Hence, in the $gg \to t\bar{t}$ process, the helicities of the $t\bar{t}$ pair will be strongly correlated, that is, mostly $t_R\bar{t}_R$ or $t_L\bar{t}_L$, where the subscripts denote the helicity of the quark. For the $q\bar{q} \to t\bar{t}$ process, the s-channel gluon can take on an S_z of -1, 0 or $+1$, and the $t\bar{t}$ pair will have correlated helicities only for the $S_z = 0$ case.

One can quantify the degree of spin correlation by the correlation coefficient

$$C = \frac{\sigma(RR + LL) - \sigma(RL + LR)}{\sigma(RR + LL) + \sigma(RL + LR)}. \tag{2.1}$$

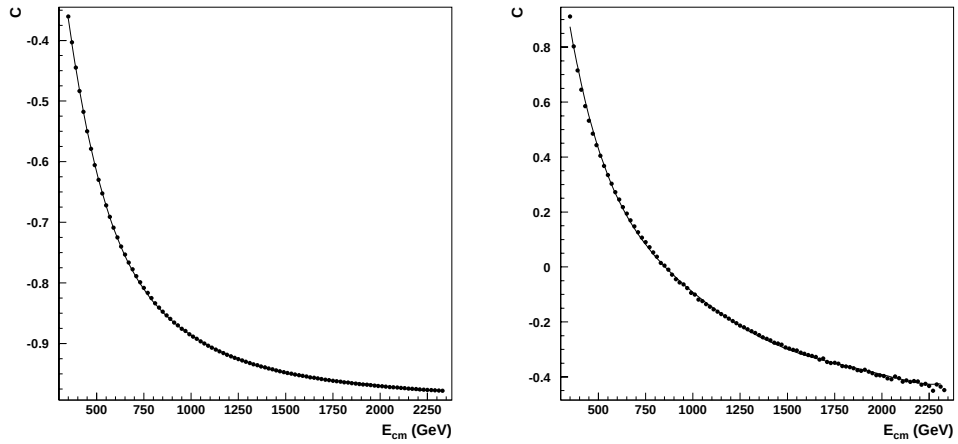

Figure 2.2: Correlation factor C for the processes $q\bar{q} \to t\bar{t}$ (left) and $gg \to t\bar{t}$ (right) as a function of the center-of-mass energy of the $t\bar{t}$ system from proton-proton collisions at the LHC.

The matrix elements and cross-sections for the production of correlated (RR+LL) and anti-correlated (RL+LR) states at the tree level have been calculated by Mahlon and Parke [29]. The correlation factor, C, was calculated for top pairs coming from pp collisions at 14 TeV and is shown in Figure 2.2 as a function of the center of mass of the $t\bar{t}$ system for the $gg \to t\bar{t}$ and $q\bar{q} \to t\bar{t}$ processes. A top mass of 175 GeV/c^2 was used for this calculation. The correlation is the largest near the threshold for top pair production and falls off due to helicity conservation at high energies.

The CP violating signal of interest is a number asymmetry between the number of $t_R\bar{t}_R$ and $t_L\bar{t}_L$ pairs. Therefore, the large average correlation at the LHC ($C = +0.31$) will make the detection of CP violation easier than at the Tevatron, where the predominant process is $q\bar{q} \to t\bar{t}$ and $C = -0.40$.

2.2 Top Decays

The top quark decays into a W boson and a down-flavoured quark. Since unitarity constraints on the CKM matrix imply $|V_{tb}|$ to be close to one, the branching ratio for

Decay		BR
$W \to l\nu$	(leptonic)	0.107
$W \to qq'$	(hadronic)	0.690

Table 2.1: Branching ratios for the W boson. The lepton, l, can represent an electron, muon, or tau.

$t \to bW$ is very close to 100%. The branching ratios for $t \to sW$ and $t \to dW$ are predicted to be about 10^{-3} and 10^{-5}, respectively.

2.2.1 Decay Modes

Decays of $t\bar{t}$ pairs are classified depending on the decays of the W^+ and W^-. The branching ratios of the W are shown in Table 2.1. If both Ws decay leptonically, then the $t\bar{t}$ pair is said to decay into the *dilepton* channel. When one of the Ws decays leptonically and the other W decays hadronically, this is termed the *semileptonic* or *lepton-plus-jets* channel. The *hadronic*, or *all-jets*, channel describes the case where both Ws decay hadronically.

Approximately one third of the leptonic decays of the W will involve $W \to \tau\nu$. The τ decays quickly with a lifetime of 2.91×10^{-13} s and has a branching ratio of 0.352 into final states with a μ or e and neutrinos. Since these products of τ decay do not come directly from a W, events with $W \to \tau\nu$ are considered background. Therefore, the term *lepton* will refer to electrons and muons only from this point on unless otherwise stated. The branching ratios for the various channels of top pair decays are given in Table 2.2.

2.2.2 Angular Distributions

For top quarks of mass $m_t = 175$ GeV/c^2, the lifetime is on the order of 10^{-25} s [30]. Due to their large mass, top quarks decay on a time scale much shorter than hadronization can

Decay	BR(%)	Channel Name
$t\bar{t} \to (bl\nu)(bl\nu)$	4.5	(dilepton)
$t\bar{t} \to (bl\nu)(bjj)$	29.5	(lepton-plus-jets)
$t\bar{t} \to (bjj)(bjj)$	47.6	(all-jets)
$t\bar{t} \to (b\tau\nu)(bjj)$	14.7	(tau-plus-jets)
$t\bar{t} \to (b\tau\nu)(bl\nu)$	4.6	(tau-plus-lepton)

Table 2.2: Branching ratios for the possible decays of a $t\bar{t}$ pair. The channels involving the tau are considered backgrounds in this study and are therefore listed separately from the other leptonic channels.

take place ($\Lambda_{QCD}^{-1} \sim 10^{-23}$ s) [31]. Consequently, the helicity is preserved in the angular distributions of its decay products.

At tree level, the decay products from a left-handed top quark have angular distributions with respect to the top spin in the top rest frame according to

$$\frac{1}{N}\frac{dN}{d\cos\theta} = \frac{1}{2}(1 + \alpha\cos\theta), \tag{2.2}$$

where $\alpha = -1$ for positively charged leptons (including τ^+) as well as for the $\bar{s}$ and $\bar{d}$ quarks, $\alpha = +0.41$ for b quarks from $t \to Wb$, and $\alpha = +0.31$ for u and c quarks, and neutrinos. The signs are reversed for the case of an anti-top decaying into the corresponding anti-particles.

2.3 CP Violation

The origin of CP violation in the Standard Model is the result of a single parameter in the CKM matrix which relates the mass eigenstates of the quarks to their corresponding weak eigenstates [14]. However, the production of $t\bar{t}$ pairs is governed by QCD which is seen to respect CP symmetry in experiments. Top pairs with right-handed helicity

($t_R\bar{t}_R$) and with left-handed helicity ($t_L\bar{t}_L$) will be produced in pp collisions at the LHC. Since these states transform into each other under a CP operation,

$$t_R\bar{t}_R \overset{CP}{\Longleftrightarrow} t_L\bar{t}_L, \tag{2.3}$$

it follows that the cross-section for producing a $t_R\bar{t}_R$ state is the same as the cross section for producing a $t_L\bar{t}_L$ state.

The parameter ΔN_{LR} is used to quantify the number asymmetry and hence the amount of CP violation and is given as

$$\Delta N_{LR} = \frac{N_{LL} - N_{RR}}{N_{RR+LL} + N_{RL+LR}} = \frac{N_{LL} - N_{RR}}{N_{TOT}}, \tag{2.4}$$

where the subscripts denote the helicity of the t and $\bar{t}$, respectively. Dividing top and bottom by $\int \mathcal{L} dt$ yields an equivalent equation in terms of cross-sections:

$$\Delta N_{LR} = \frac{\sigma(t_L\bar{t}_L) - \sigma(t_R\bar{t}_R)}{\sigma(t\bar{t})_{TOT}}. \tag{2.5}$$

A non-zero result indicates that CP symmetry is violated, and physics beyond the Standard Model may be present. Three examples of theories that may exhibit $\Delta N_{LR} \neq 0$ use popular extensions of the Standard Model and are presented next.

2.3.1 CP Violating Models

Extensions to the Standard Model include more particles than supplied by the SM. Additional particles means that the couplings of these particles could carry complex phases which could lead to CP violation. The following three theories incorporate popular extensions of the Standard Model and may exhibit CP violation in $t\bar{t}$ production.

Peskin–Schmidt Model (2HDM)

Peskin and Schmidt proposed a possible way of obtaining CP violation in $t\bar{t}$ production in the two-Higgs doublet model (2HDM) [32]. In their theory, the lightest Higgs (h^0) couples to the top quark with a vertex factor

$$\frac{-im_t}{v}(AP_L + A^*P_R)t\bar{t}h^0 \tag{2.6}$$

where v is the electroweak scale, A is a complex number that is a combination of mixing angles, and P_L and P_R are the left and right projection operators, respectively. The parameter A has a theoretical constraint of $|Im(A^2)| < \sqrt{2}$ [33] which limits the maximum amount of CP violation exhibited by this theory. The lightest Higgs in the theory will be the largest contributor to the CP violating amplitude and the propagator term for the heavier Higgs of the doublet suppresses its contribution. CP violation in this model appears due to the interference between Feynman diagrams shown in Figure 2.3 and the tree level diagrams for $t\bar{t}$ production in Figure 2.1.

The size of the signal is a function of the partonic center of mass energy; Figure 2.4 shows the dependence of ΔN_{LR} on $\sqrt{s}$ assuming a top mass of 175 GeV/c^2. For the case where $m_{h^0} > 2m_t$, a pole appears for the gg process and is shown in Figure 2.5 for the case of $m_{h^0} = 400$ GeV/c^2.

The maximum value of ΔN_{LR} (averaged over $\sqrt{s}$) that can be generated by this model is $\Delta N_{LR} \sim 0.003$. It will be shown that this level of CP violation can not be detected with ATLAS even after several years of high luminosity operation. However, there are other models with new physics that allow for a larger signal of CP violation and are presented below.

Schmidt Model (SUSY)

Supersymmetry (SUSY) is another extension of the Standard Model. One problem in the Standard Model is that corrections to the Higgs mass from loops containing a fermion

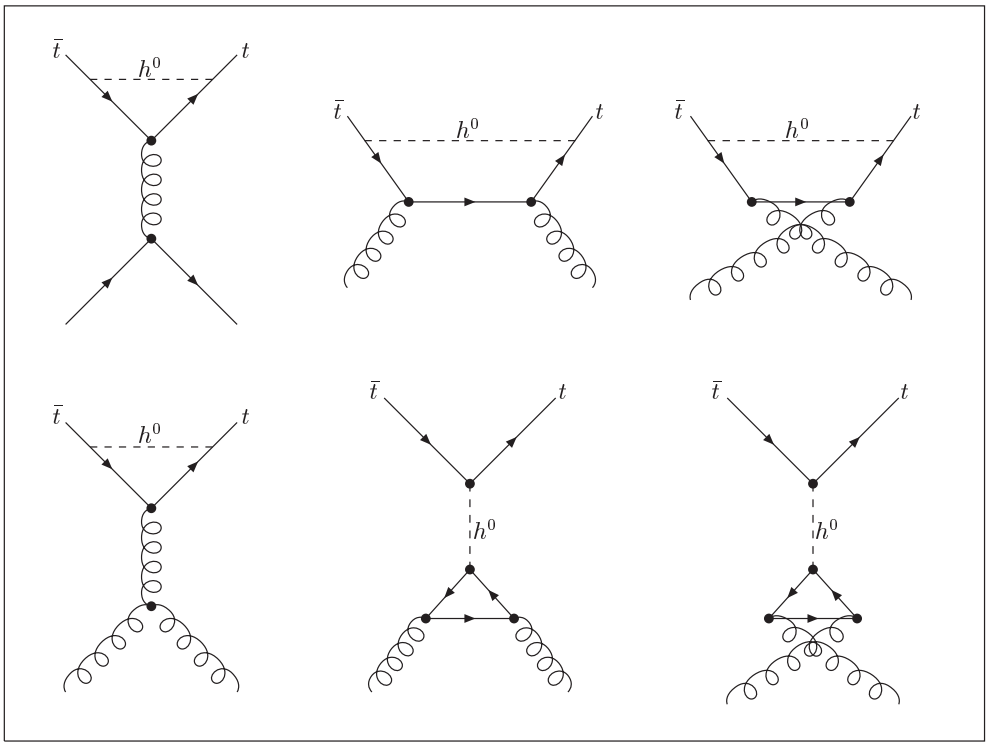

Figure 2.3: Feynman diagrams that contribute to CP violation in $t\bar{t}$ production in the Peskin–Schmidt model.

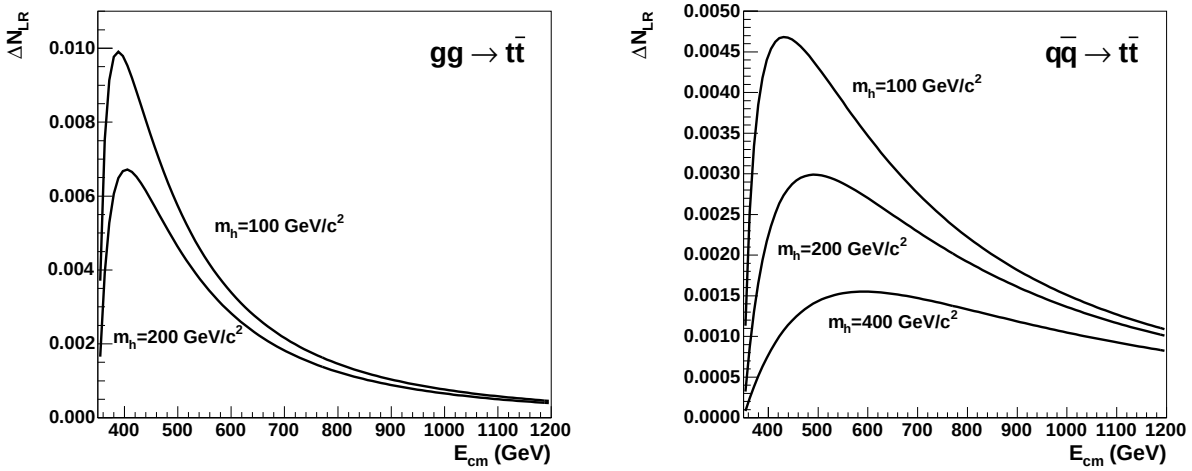

Figure 2.4: Dependence of ΔN_{LR} on the center of mass energy $\sqrt{s}$ of the $t\bar{t}$ system for several values of the (light) Higgs mass and $m_t = 175$ GeV/c^2 according to the Peskin-Schmidt model. The plot on the left(right) corresponds to $gg \to t\bar{t}$ ($q\bar{q} \to t\bar{t}$).

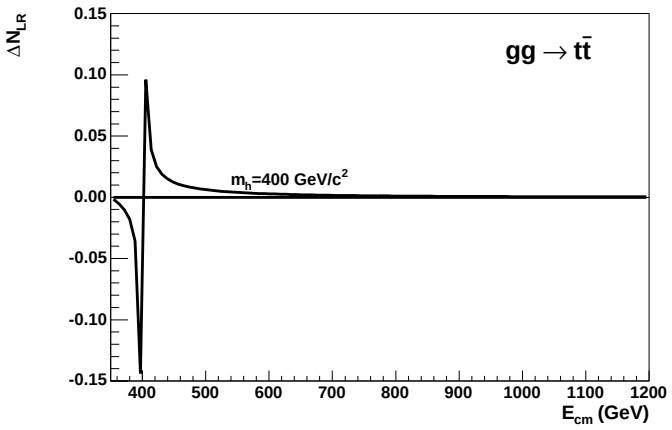

Figure 2.5: Dependence of ΔN_{LR} on the center of mass energy $\sqrt{s}$ of the $t\bar{t}$ system for $m_{h^0} =$ 400 GeV/c^2 and $m_t = 175$ GeV/c^2 according to the Peskin-Schmidt model for $gg \to t\bar{t}$. The resonance effect appears for values $m_{h^0} > 2m_t$ due to the constructive interference of the diagrams with the Higgs in the s-channel. The asymmetry in the vertical scale is a result of the sensitivity to how the numerical integration was performed.

make the Higgs mass increase quadratically with the cut-off scale. To solve this problem, a new symmetry is introduced where each Standard Model particle has a supersymmetric partner; quarks have bosonic partners called *squarks*. The supersymmetric partner of a top quark is a *stop* ($\tilde{t}$), and the partner of the gluon is the *gluino* (λ) which is a fermion. The quadratic divergence to the Higgs mass is canceled out by the additional corrections from the supersymmetric particles.

In the Schmidt model [34], a number of complex parameters are collected into a single phase, ϕ. The quark-squark-gluino vertex factor in this case is

$$ig\sqrt{2}[e^{i\phi}\tilde{t}_L^* T^a(\bar{\lambda}^a t_L) + e^{-i\phi}\tilde{t}_R^* T^a(\bar{\lambda}^a t_R)] + h.c., \tag{2.7}$$

where g is a coupling constant.

The stops can be written in terms of mass eigenstates, $\tilde{t}_1$ and $\tilde{t}_2$, with a mixing angle, α:

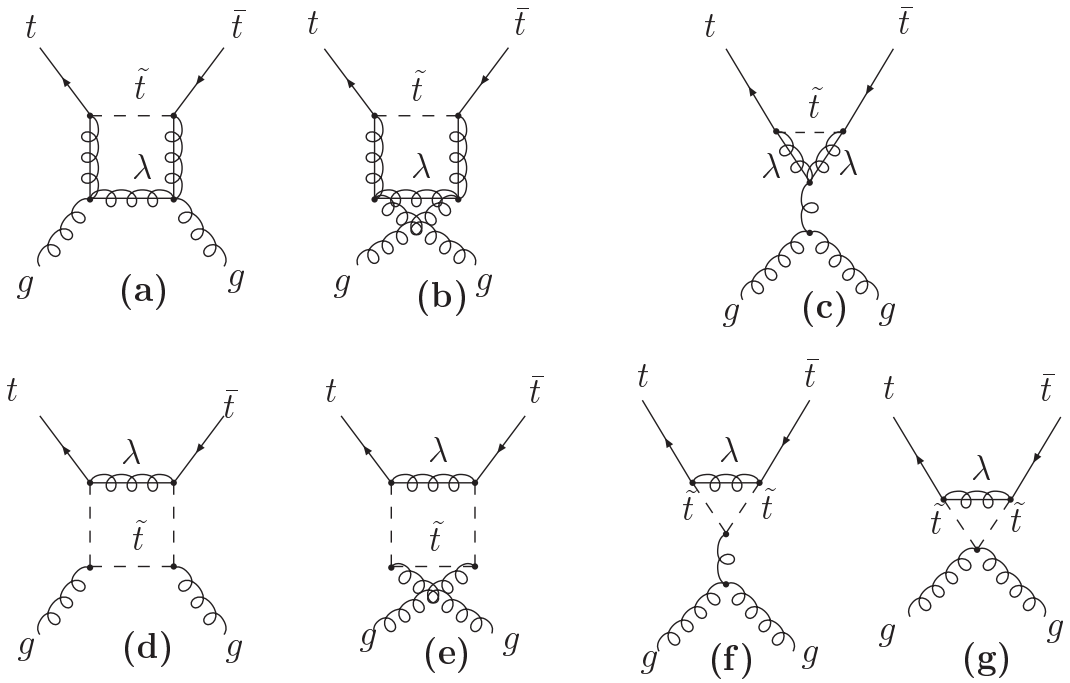

Figure 2.6: One loop diagrams in SUSY interfere with the tree level diagrams for $t\bar{t}$ production and can lead to CP violation.

$$\tilde{t}_L = \tilde{t}_1 \cos\alpha + \tilde{t}_2 \sin\alpha \tag{2.8}$$

$$\tilde{t}_R = -\tilde{t}_1 \sin\alpha + \tilde{t}_2 \cos\alpha. \tag{2.9}$$

The one-loop diagrams shown in Figure 2.6, with intermediate gluinos (λ) and stops ($\tilde{t}$), interfere with the amplitudes of the tree-level diagrams of Figure 2.1. The CP violating asymmetry for this model is proportional to

$$\sin 2\alpha \sin 2\phi. \tag{2.10}$$

The CP violating effect disappears when $|m_{t1} - m_{t2}|$ goes to zero.

The diagrams of Figure 2.6(a)–(c) provide the largest contribution to the CP violating effect for energies $\sqrt{s} > 2m_\lambda$, and do not contribute at all for smaller energies. The diagrams of Figure 2.6(d)–(f) contribute for all energies above the threshold for top pair

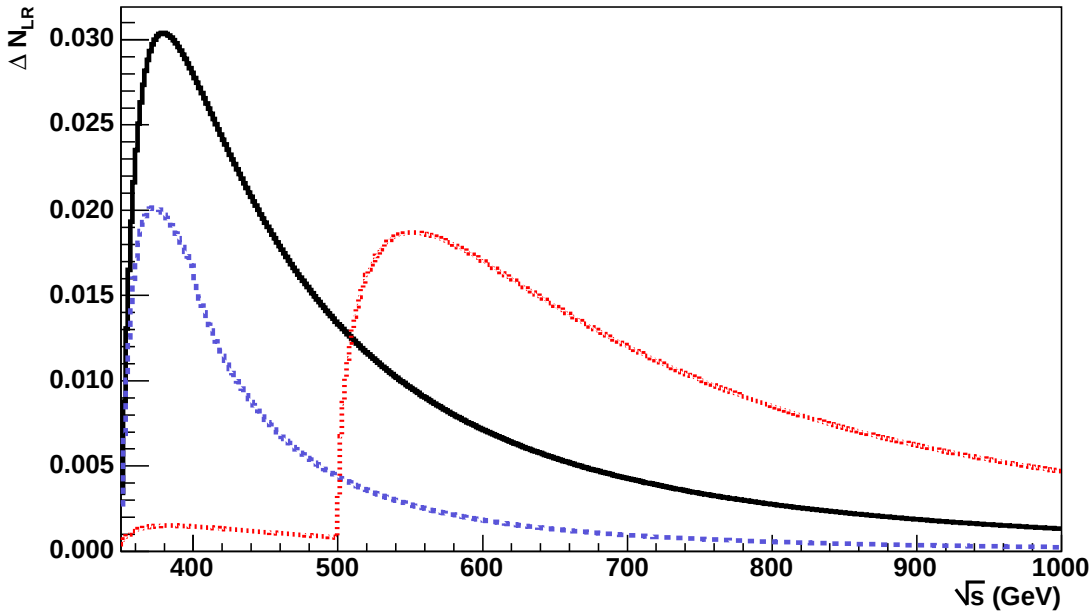

Figure 2.7: The maximum possible values for ΔN_{LR} as a function of partonic center-of-mass energy predicted in SUSY for various values of m_λ, m_{t1}, and m_{t2}. The black/solid line corresponds to $m_\lambda = 175$ GeV/c^2, with stop masses of 100 GeV/c^2 and 500 GeV/c^2. The blue/dashed line results from $m_\lambda = 175$ GeV/c^2 and stop masses of 100 GeV/c^2 and 200 GeV/c^2. The green/dotted line corresponds to $m_\lambda = 250$ GeV/c^2 and stop masses of 100 GeV/c^2 and 500 GeV/c^2. The top mass is taken to be 175 GeV/c^2.

production, $\sqrt{s} > 2m_t$. The largest CP violating signal was calculated for a number of different values of m_λ, m_{t1}, and m_{t2} are shown in Figure 2.7. A top mass $m_t = 175$ GeV/c^2 was used.

It is possible that ΔN_{LR} averaged over $\sqrt{s}$ can be as large 1–2% in this model.

Beccaria-Renard-Verzegnassi Model (MSSM)

A prediction of CP violation is made in the framework of the minimal supersymmetric model [35]. The minimal supersymmetric model (MSSM) is a supersymmetric model where only superpartners of Standard Model particles are included.

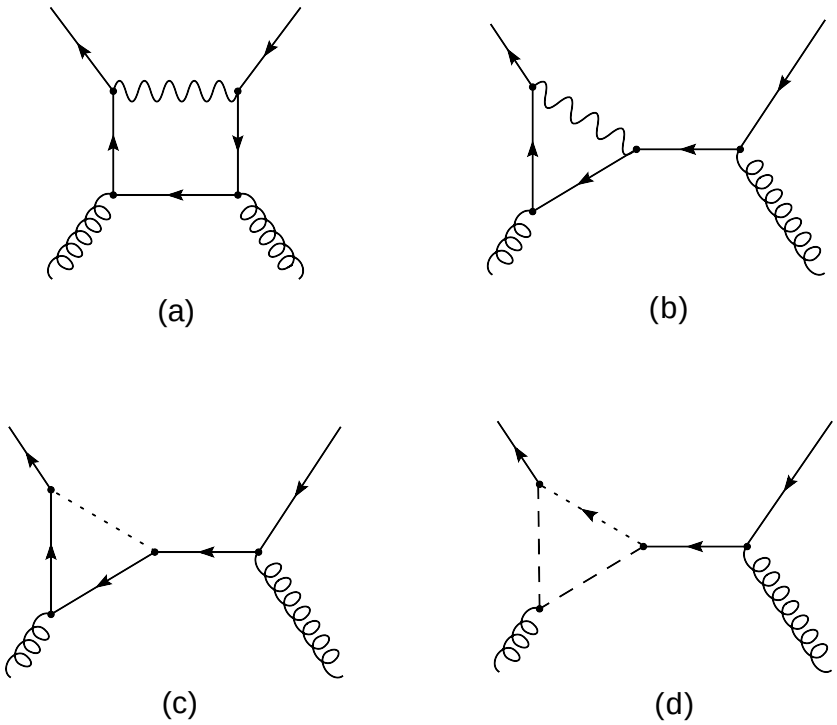

Figure 2.8: One-loop corrections to $gg \to t\bar{t}$ that contribute to CP violation in $t\bar{t}$ production. The gauge bosons in (a) and (b) can be either a Z^0 or $W^{\pm}$. The dotted line in (c) represents a Higgs boson (H^0, $H^{\pm}$, h^0, A^0). In (d), the dashed line represents a sbottom or a stop, and the dotted fermion line represents a chargino or a neutralino.

Next-to-leading linear logarithmic order accuracy corrections are calculated at the one-loop level for the $gg \to t\bar{t}$ process. The diagrams used for the corrections are shown in Figure 2.8. Moderately light supersymmetric particles (~ 350 GeV/c^2) are assumed.

At the one-loop level, the cross sections σ_{LL} and σ_{RR}, gain an additional dependence on the parameter $\tan\beta$. The amount of CP violation that can be produced at this order only depends on the value of $\tan\beta$. The largest possible signals from this theory give $\Delta N_{LR} \approx 5 - 6\%$ for $\tan\beta = 50$.

2.3.2 Model Independent Approach

Since there is always the possibility that a non-zero value of ΔN_{LR} can come from one of the previously mentioned mechanisms, or from a new kind of physics, it is preferable that the measurement be independent of any model that makes a prediction for $\Delta N_{LR} \neq 0$.

In all the models mentioned above, the value of ΔN_{LR} in general depends on the center of mass energy of the interacting partons, so any measurement should also measure this dependency. In doing so, and with enough data, one may be able to identify which model is responsible for the CP violation and preclude those that definitely are not. A method to measure ΔN_{LR} that achieves this objective is presented in Section 2.4.2. This method is used in Chapter 6 in the context of the ATLAS experiment.

2.4 Strategies for a CP Violation Measurement

In this section, the methods for detecting and measuring CP violation in $t\bar{t}$ production will be outlined as would apply in an ideal situation to illustrate the principles involved. The discussion of how these analysis strategies will be implemented in an experimental situation with the ATLAS detector will take place in Chapters 5 and 6.

2.4.1 Momentum Asymmetries in the Dilepton Channel

The idea that ΔN_{LR} could be measured in the dilepton channel was initially investigated because it follows up on the method described in [32] and [34] by Schmidt and Peskin. They suggest the momentum asymmetry between the positively and negatively charged leptons be used to observe CP violation in top pair production.

The momentum distribution for leptons coming from a top in its rest frame does not depend on the helicity of the top. However, the top quarks that are produced in a collider experiment are observed in the lab frame. Depending on the helicity of the $t\bar{t}$ pair, the lepton will be preferentially emitted either forward or backward with respect

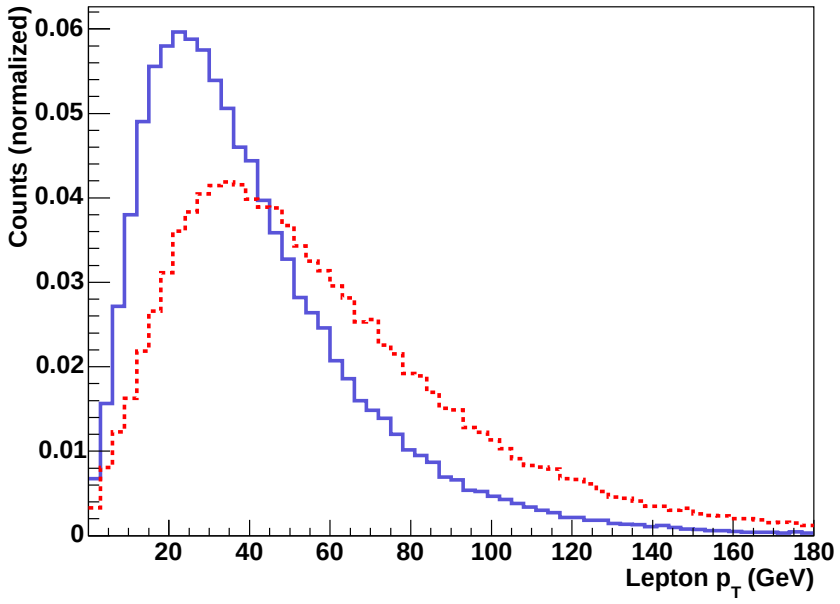

Figure 2.9: Transverse momentum distributions for leptons from $t_L\bar{t}_L$ events. The distribution for positively charged leptons is shown in red (dotted) and the distribution for negatively charged leptons is shown in blue (solid).

to the motion of the top. The angular distribution of leptons coming from top decays is described in 2.2.2. Leptons emitted forward of the top quark will have a larger p_T on average in the lab frame than leptons emitted behind the top. Specifically, the $l^+(l^-)$ from the $t_R(\bar{t}_L)$ will get the greater boost and *vice versa*. Figure 2.9 shows the p_T distributions of positively charged leptons from $t_L\bar{t}_L$ pairs produced in pp collisions at 14 TeV. It follows that an excess of $t_L\bar{t}_L$ events, for example, will result in the $p_T(l^-)$ distribution being shifted to larger momentum. Figure 2.10 illustrates how the $p_T(l^\pm)$ distributions and transverse momentum asymmetry would appear in an ideal experiment for an integrated luminosity of 0.8 fb^{-1} and $\Delta N_{LR} = 0.10$. Momentum asymmetries are briefly investigated in Chapter 5.

A sufficiently large CP violating signal will be apparent using this method but measuring an actual value for ΔN_{LR} will be extremely difficult. First, it will not be clear which physics is responsible for producing the asymmetry, and second, the detector reso-

lution will distort the leptonic p_T distributions. Another disadvantage of this approach is that the dependence of ΔN_{LR} on $\sqrt{s}$ can not easily be determined because the $t\bar{t}$ system cannot be reconstructed in the dilepton channel, and that the momenta of the leptons are not correlated directly to $\sqrt{s}$. Another approach using the lepton-plus-jets channel is more promising and is presented next.

2.4.2 Direct Measurement of ΔN_{LR} in the Lepton-Plus-Jets Channel

A direct measurement of ΔN_{LR} can be made using the lepton-plus-jets channel. In this channel, the leptonically decaying top can be reconstructed to determine the angle $\cos\theta$ of the lepton momentum with respect to the top momentum in the top rest frame. Also, the reconstruction of the $t\bar{t}$ system can be performed using the lepton-plus-jets channel to find the partonic center of mass energy, $\sqrt{s}$. Therefore, a measurement of ΔN_{LR} as a function of $\sqrt{s}$ can also be made.

The method for directly determining ΔN_{LR} is straightforward in principle. Reconstruction of the $t\bar{t}$ pair can be done since there will be a b-jet and two light quark jets from the hadronically decaying top, and a b-jet, lepton, and missing energy due to the neutrino from the leptonically decaying top. The angle $\cos\theta$ can be found for each event. More details regarding the reconstruction can be found in Chapter 6. By comparing the $\cos\theta$ distributions for oppositely charged leptons, a quantitative measurement of ΔN_{LR} can be made.

To illustrate, consider the ideal case where all top pairs are selected and $\cos\theta$ can be measured perfectly. When $\Delta N_{LR} = 0$, the angular distributions for l^+ and l^- will be flat, but an excess of $t_L\bar{t}_L$ or $t_R\bar{t}_R$ events will sit atop that flat distribution as shown in Figure 2.11. The number of excess events allows one to measure ΔN_{LR}. If the asymmetry of the two $\cos\theta$ distributions are taken, and the slope, m, is found as illustrated in Figure 2.12(a), the commonalities in the distributions cancel out and only the effect due

to excess $t_L\bar{t}_L$ or $t_R\bar{t}_R$ pairs remains. Taking equal numbers of $l^+$and l^-events, N_{l^+} and N_{l^-}, the measured value of ΔN_{LR} is given by

$$\Delta N_{LR} = \frac{mN_{bins}}{N_{TOT}}, \tag{2.11}$$

where $N_{TOT} = N_{l^+} + N_{l^-}$, and N_{bins} is the number of bins in the histogram.

In practice, experimental limitations will distort the $\cos\theta$ distributions as a result of cuts in the event selection process, backgrounds, and the detector acceptance. As long as the distortions in the $\cos\theta$ distributions can be well characterized and corrected, the measurement of ΔN_{LR} can still be made.

It will be seen in Chapter 6, where the lepton-plus-jets channel is considered, that a measurement of $\cos\theta$ has a poor resolution. When only two bins in the asymmetry are used as illustrated in Figure 2.12(b), a measurement of ΔN_{LR} can still be made using

$$\Delta N_{LR} = \frac{2(\delta_1 + \delta_2)}{N_{TOT}}, \tag{2.12}$$

where δ_1 and δ_2 are the absolute values of areas under the left and right hand side of the asymmetry, respectively.

To summarize, the measurement of ΔN_{LR} will best be done in the lepton-plus-jets channel because it is not sensitive to the physics that produces the CP violation which may exist in $t\bar{t}$ production. Therefore, the dilepton approach is only briefly considered in Chapter 5 while the method using the lepton-plus-jets channel is investigated more fully in Chapter 6.

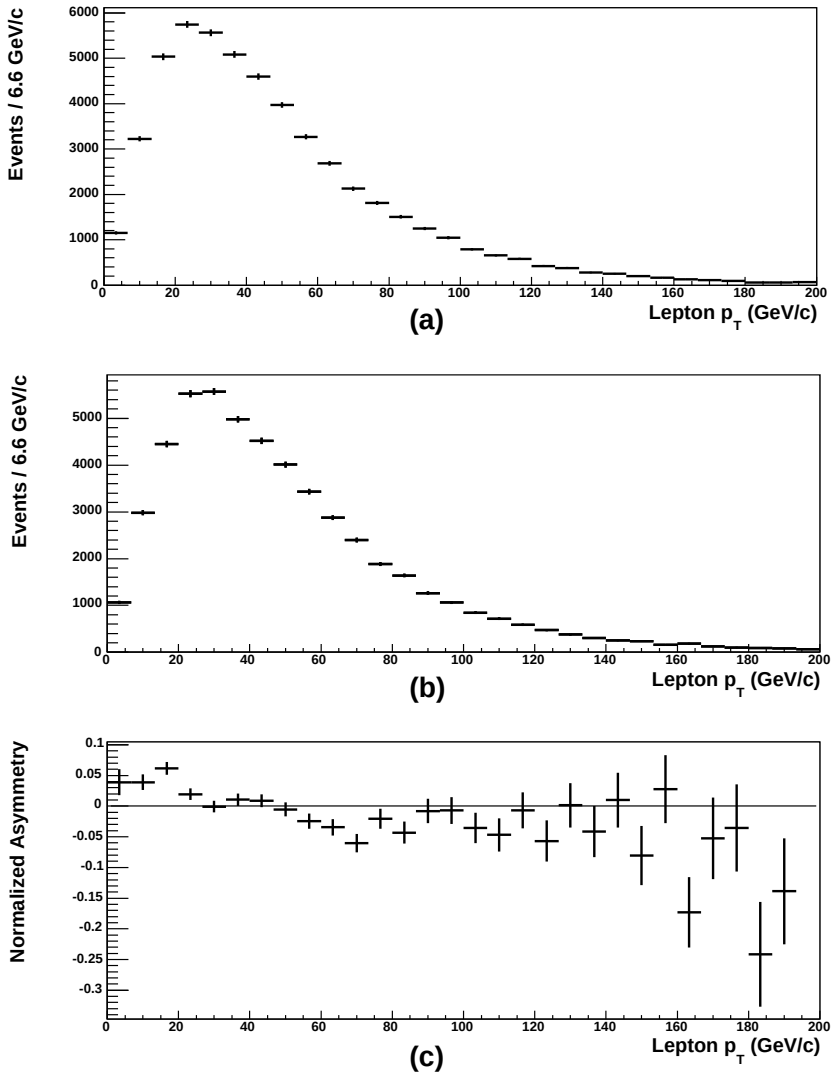

Figure 2.10: The dilepton channel result expected if an idealized experiment with pp collisions at 14 TeV were carried out with an integrated luminosity of 0.8 fb^{-1} and $\Delta N_{LR} = 0.10$. The p_T distributions for positive and negative leptons are shown in (a) and (b), respectively. The normalized asymmetry is shown in (c).

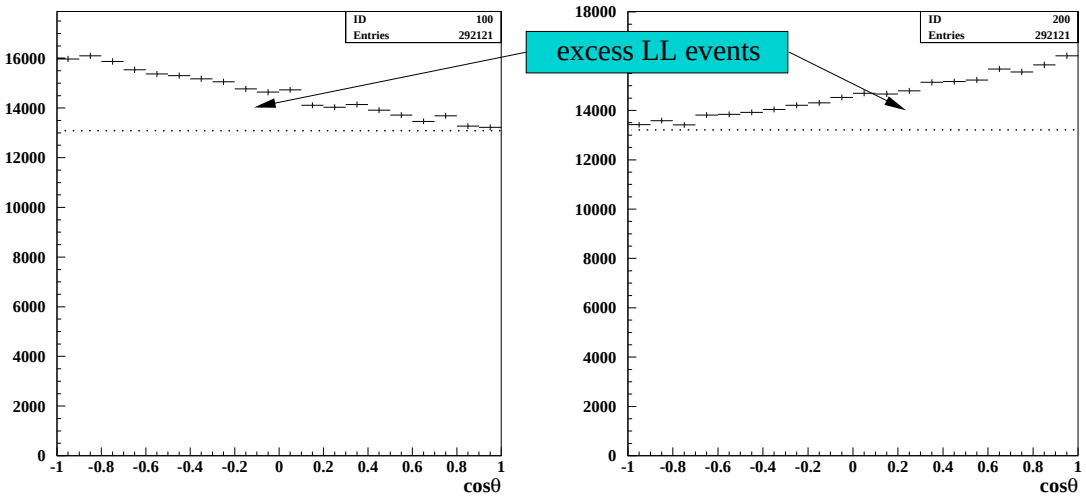

Figure 2.11: Angular distributions of l^+ (left) and l^- (right) that are expected if an idealized experiment were carried out using the lepton-plus-jets channel and $\Delta N_{LR} = 0.10$.

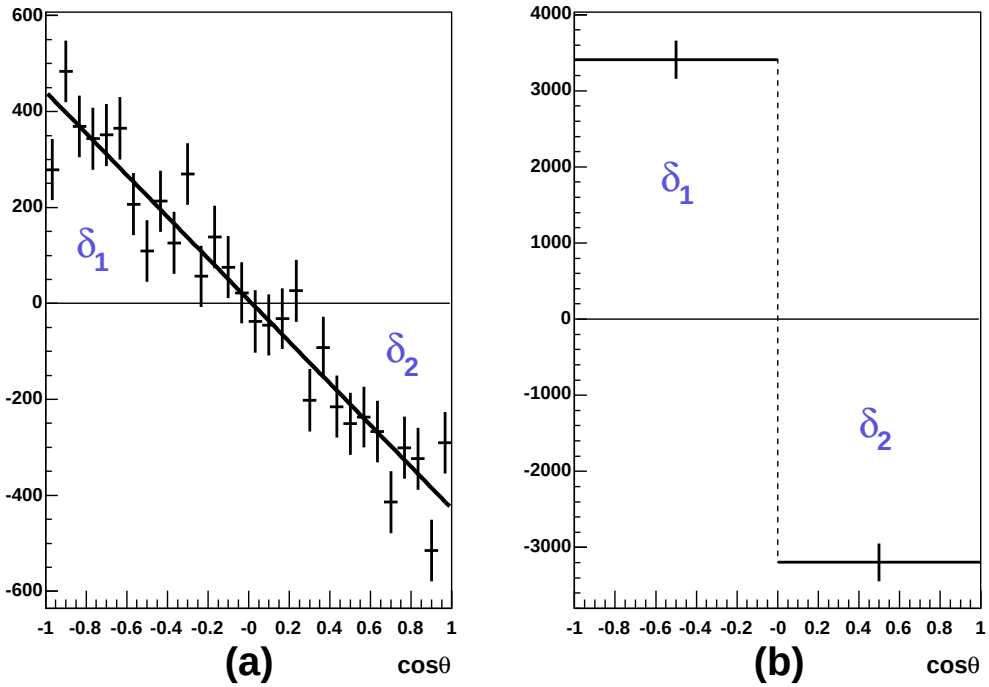

Figure 2.12: The resulting asymmetries if an idealized experiment were carried out for an integrated luminosity of 0.8 fb^{-1} and $\Delta N_{LR} = 0.10$ for distributions with (a) 30 bins and (b) 2 bins.

Chapter 3

The ATLAS Spectrometer

The ATLAS experiment is a general purpose detector being built to observe pp collisions at the LHC. With good coverage in both tracking and calorimetry, ATLAS is well designed to observe a large range of particle physics phenomena. Bunches of protons cross every 25 ns with a high luminosity, so components must survive a high radiation environment and the detectors must have good time resolution. The detector components of ATLAS are described below starting at the region closest to the interaction point.

Like many other detectors in high energy collider experiments, the ATLAS spectrometer has a cylindrical symmetry about the beam axis as can be seen in Figure 3.5. The z-axis is taken to be along the beam direction. It is necessary to describe the angle, θ_{lab}, between the beam axis and a particle's momentum as it travels away from the interaction point. The pseudorapidity, η, given by

$$\eta = -\ln(\tan\frac{\theta_{lab}}{2}) \tag{3.1}$$

is commonly used.

This study assumes the ATLAS experiment has all of its components as described in the Technical Design Reports. However, the detector will not be in its final configuration when collisions at the LHC begin in 2007. These differences are summarized in Section 3.5

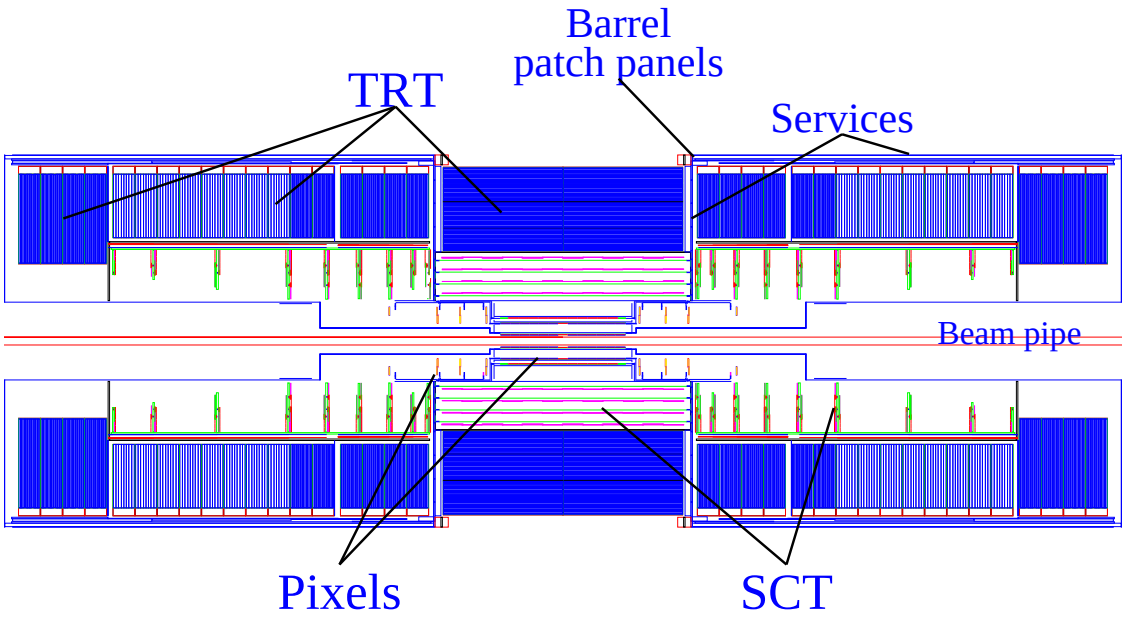

Figure 3.1: Section through the ATLAS inner detector. The inner detector has a diameter of 2300 mm, has a length of 7000 mm, and covers the region $|\eta| < 2.5$.

and the impact on detector performance is briefly discussed there.

3.1 Inner Detector

Particles originating from the interaction point encounter the inner detector region first. This part of the detector consists of the pixel detector, the semiconductor trackers, and the transition radiation tracker (TRT) and is shown in Figure 3.1 [36, 37, 38].

The magnetic field is supplied by a superconducting solenoid located in the cryostat that contains the electromagnetic barrel calorimeter. The central field is 2 T and is orientated in the z-direction along the beam axis. Near the ends of the solenoid, deviations from the infinite-length solenoid approximation become important; B_z falls to 1 T and the radial component of the field grows to about 0.5 T.

3.1.1 Pixel Detector

The pixel detector is located closest to the beam axis and is the key to accurately reconstructing the primary vertex of the interaction point. It is also needed for secondary vertex reconstruction which is critical for the identification of b-jets and jets from τ-leptons. The pixel detector has 80×10^6 channels and is 1.4 m long and 0.500 m in diameter.

The pixel detector has a high granularity which leads to lower occupancy and therefore good pattern recognition. The active elements of the detector are arrays of pixels on 16.4×60.8 mm^2 silicon wafers with each silicon wafer containing 46080 pixels. The pixels themselves are 50×400 μm with the larger dimension parallel to the beam axis. These wafers are arranged in three concentric layers in the barrel region at nominal distances of 50.5, 88.5, and 122.5 mm from the beam axis. The innermost layer is also called the B-layer due to its importance in b-jet tagging. The detector covers a larger region up to $|\eta| < 2.5$ with four disks in each of the forward regions.

3.1.2 Semiconductor Tracker

After the pixel detector, particles originating from the interaction point encounter the semiconductor tracker (SCT). The SCT measures the position of 8 points along the path of a charged particle.

The SCT consists of p-on-n silicon microstrip detectors with a pitch of 80 μm. A detector element has 768 strips on a substrate of size 6.36×6.40 cm^2. These elements are taken four at a time and assembled into modules. The detectors are glued back-to-back onto a substrate that provides cooling. To achieve a position measurement in the longitudinal direction, the strips on either side of the cooling substrate are oriented at an angle of 40 mrad with respect to each other.

The spatial resolution of the SCT is 16 μm in the azimuthal direction and 580 μm

in the z-direction resulting in a high granularity to provide the same advantages as the pixel detector. Two tracks can be resolved if they are more than 200 μm apart.

The barrel modules are positioned at radii of 30.0, 37.3, 44.7, and 52.0 cm. The endcaps are arranged as 9 wheels in the forward region on either side of the interaction point and provide coverage down to $|\eta| < 2.5$.

3.1.3 Transition Radiation Tracker

The transition radiation tracker (TRT) occupies the outermost part of the inner detector region. The TRT is used for tracking and has the capacity to distinguish between electrons and heavier charged particles.

The basic elements of the detector are drift tubes known as straws. Each straw is 4 mm in diameter, less than 150 cm in length, and has a gold plated W-Re wire in the center. For the purposes of tracking, the straws act as a drift tube as each channel provides a drift time measurement. The spatial resolution for a single straw is 170 μm.

In the barrel region, 50 000 straws are aligned parallel to the beam axis such that the position of an average particle will measured 36 times. The barrel straws are divided in two at the center to reduce occupancy, and the signals are read out at both ends of the detector.

The TRT also provides particle identification information for charged particles traversing it. Transition radiation can be produced when a charged particle with a velocity v travels across the interface between two media with differing dielectric constants. The radiation has an energy in the X-ray region around 2–20 keV and the total energy of TR radiation produced is proportional to the relativistic factor $\gamma = (1 - \frac{v^2}{c^2})^{1/2}$ which is useful for distinguishing electrons from other particles [39]. The probability of TR photons being produced by an electron is only $\sim$0.5% for one boundary crossing, so polypropylene/polyethylene foils and fibres are used in the end-caps and barrel, respectively, so that a particle experiences many dielectric transitions between air and the foils/fibres.

The gas in the straws is a mixture of Xe(70%), CO_2(20%), and CF_4(10%) and chosen for the efficient detection of the X-rays produced.

In addition to the drift time measurement, the signal in each channel is sent to a discriminator with one low and one high threshold setting: the lower threshold is used for tracking purposes and the higher threshold signals a TR hit in that channel.

The pion rejection factor at 90% electron efficiency for particles with $p_T = 20$ GeV/c varies from 20 to 100 depending on η, with the poorest performance in the transition region between barrel and end-cap.

3.1.4 Inner Detector Performance

The selection of $t\bar{t}$ events and the measurement of lepton p_T depends on the overall performance of the inner detector. The important issues for the present analysis are the quality of track parameter measurements, charge misidentification, and b-jet tagging performance.

The transverse impact parameter, d_0, is the distance of the closest approach of a track to the beam axis. The transverse momentum and impact parameter resolutions have been studied using the full Monte Carlo simulation of the detector [38]. The track parameter resolutions for muons can be parameterized as

$$\sigma(\tfrac{1}{p_T}) \approx (0.36 \oplus \tfrac{13}{p_T\sqrt{\sin\theta}}) \times 10^{-3} \tag{3.2}$$

$$\sigma(d_0) \approx (11 \oplus \tfrac{73}{p_T\sqrt{\sin\theta}}) \tag{3.3}$$

where p_T is in GeV/c and d_0 is in μm. The angle θ is the angle between the momentum vector of the track and the beam axis.

The rate of obtaining the wrong sign for the charge of a particle increases with p_T. For electrons with $p_T < 500$ GeV/c, the fraction of events where the sign of the charge is incorrect is 1.4%. For muons in the same p_T range, the fraction is 0.2%. The vast majority

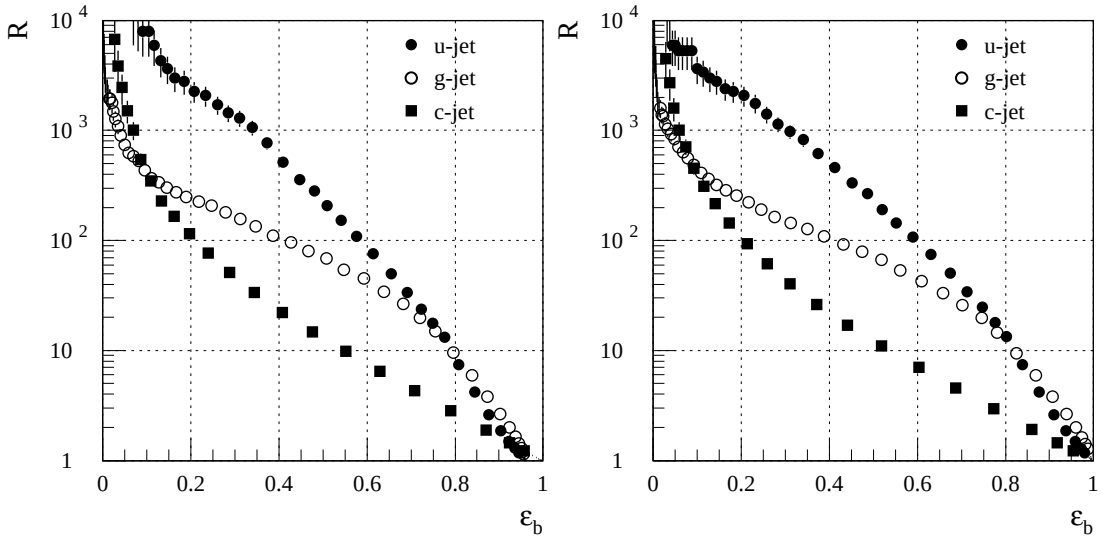

Figure 3.2: Rejection factors as a function of b-jet efficiency for the track reconstruction algorithms (a) xKalman and (b) iPatRec.

of leptons coming from $t\bar{t}$ events have a p_T less than 500 GeV/c (see Figure 6.1(a).

The tagging of b-jets can be carried out by examining tracks within a jet to see if a significant number have large impact parameters, possibly indicating the decay of a B meson. For each jet, a weight W is determined indicating the likelihood that the jet is a b-jet. A jet with a larger value of W indicates a larger probability of being a b-jet. In practice, a value of W_0 is chosen, and all jets with $W > W_0$ are tagged as b-jets. The particular value of W_0 will determine the efficiency and rejection factor for different types of jets. Figure 3.2 [38] shows the rejection factor R as a function of b-jet efficiency, ϵ_b, for two different reconstruction algorithms: xKalman [40] and iPatRec [41].

3.2 Calorimeters

The calorimeters measure the energy of electrons, photons, jets and missing transverse energy. It must provide good energy resolution, excellent angular coverage, and be thick enough so that showers are contained and punch-through to the muon spectrometer is minimized. Figure 3.3 [38] shows the calorimeter system surrounding the elements of the

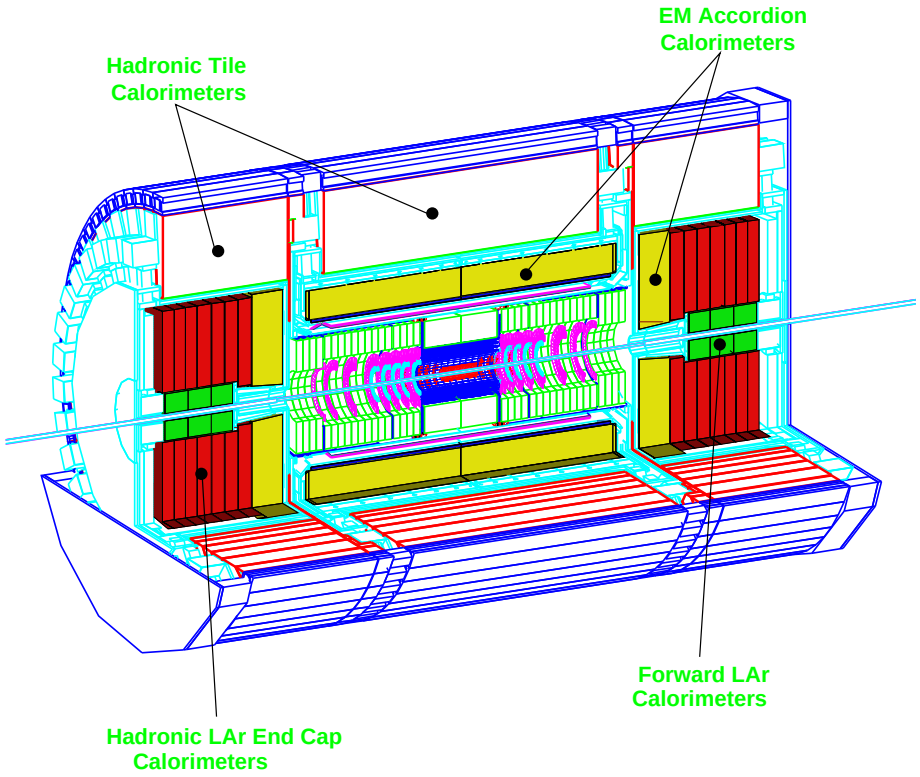

Figure 3.3: Cutaway view of the ATLAS calorimeter system. The various components are indicated in the figure. Overall, the the calorimeter is 11.46 m in length and has a radius of 4.25 m.

inner detector. All calorimeters are located in liquid argon (LAr) cryostats except for the hadronic tile calorimeter. The calorimeter components are described in the following sections along with a brief discussion of the overall expected performance.

3.2.1 Liquid Argon Calorimeter

The LAr calorimeter[42] consists of many subsystems: the barrel and endcap EM calorimeters, the hadronic endcap calorimeters, and the forward EM and hadronic calorimeters.

The barrel EM calorimeter is in a separate cryostat that also contains the presampler and the superconducting solenoid. The endcap and forward calorimeters are in cryostats located at each end of the barrel.

The LAr calorimeters differ in the absorber material used, but the sensitive medium in every case is liquid argon. Some of the particles produced in a shower travel through the LAr and ionize it. In a well-designed calorimeter, the amount of charge collected will be proportional to the energy of the incident particle.

LAr EM Calorimeter

The LAr barrel calorimeter measures the energy of electrons and photons in the central region covering $0 < |\eta| < 1.4$. It is 6.8 m long, has an inner radius of 1.15 m, and an outer radius of 1.15 m and 2.25 m. The absorbers are lead sheets that are 1.5 mm thick and bent into an accordion shape and sandwiched in between two thin layers of stainless steel. There are 1024 of these sheets arranged around the beam axis.

Readout is done with thin copper/polyimide multilayer material that are centered in between the lead sheets with a honeycomb spacer. The outer layer of copper has the high voltage applied to create the electric field in the LAr gap. The inner copper layer carries the signal from induced currents. The middle layer is etched such that the calorimeter is segmented into cells in η and ϕ as well as into 3 compartments radially. There are $\sim 10^5$ channels in the barrel EM calorimeter.

The materials and technology used in the LAr endcap calorimeters are similar to those used in the barrel. It is located in a separate cryostat and the configuration of the accordion shaped absorbers is different as this calorimeter covers the region $1.4 < |\eta| < 3.2$.

The LAr EM Calorimeter will have a good energy resolution with a sampling term of approximately $10\%/\sqrt{E}$. Calibration can be done with very little integrated luminosity using $Z \rightarrow ee$ events, because this process has a high cross-section. The resulting constant

term for the resolution is expected to be 0.7%.

Hadronic Endcap Calorimeter

The hadronic endcap calorimeter (HEC) shares the same cryostat as the LAr EM calorimeter. It measures the energy of hadronic showers and showers in the range $1.5 < |\eta| < 3.2$ not contained by the EM endcap. Copper absorbers are employed with plates 25 mm and 50 mm thick. The former are closer to the interaction point. The plates have a 8.5 mm gap in between them for the liquid argon and the structures required for the readout of signals.

Forward Calorimeters

The forward calorimeters are located very near the beampipe to provide energy measurements in the rapidity range $3.1 < |\eta| < 4.9$. There are three calorimeters in the forward region, the calorimeter closest to the interaction point is made of copper and is more adapted for EM energy measurements. The second 2 modules have tungsten absorbers and are suited for energy measurements of hadronic showers not contained by the first.

3.2.2 Tile Calorimeter

The tile calorimeter [43] measures the energy from hadronic showers which are not contained by the LAr EM calorimeter. It is constructed of steel and scintillating tiles and comes in three pieces: a barrel and on either end, two extensions to the barrel and can clearly be seen in Figure 3.3. The inner and outer radii of the tile calorimeter are 2280 mm and 4230 mm, respectively. The barrel section is 5640 mm long to cover $|\eta| < 1.0$ in pseudo-rapidity, and the extensions go out to ± 6110 mm in the z-coordinate to cover the region not covered by the barrel or hadronic endcaps.

The barrel and extensions are each composed of 64 wedged shaped modules. Each module has scintillating tiles inserted into the steel structure at regular intervals. Optical

fibres are attached to the scintillating tiles take the light signals to PMTs which are located on the outer edge of the calorimeter.

3.2.3 Calorimeter Performance

The calorimeters are expected to meet several criteria which are important for physics studies at the LHC [44]. Among these are a fast response time, high radiation resistance, and a thickness of at least 9 λ_{int} to contain showers from high energy pions.

The energy resolution of the EM calorimeters is

$$\frac{\sigma}{E} = \frac{10\%}{\sqrt{E}} \oplus 0.7\% \tag{3.4}$$

for electrons and photons. The response to hadronic jets is

$$\frac{\sigma}{E} = \frac{50\%}{\sqrt{E}} \oplus 3\% \tag{3.5}$$

in the central rapidity region.

The light jet energy scale can be calibrated to the 1% level using an *in situ* calibration technique using jets from a W resonance coming from $t\bar{t}$ events decaying into the lepton plus jets channel [45].

The calorimeters provide good coverage up to $|\eta| \approx 5$ which is important for missing E_T measurements. The reconstruction of $t\bar{t}$ events requires good E_T^{miss} measurements because there is a neutrino in the final state for the lepton-plus-jets channel. The E_T^{miss} resolution depends on the how well the calorimeter is calibrated and degrades with the total transverse energy measured in the calorimeters and can be approximated by $\sigma(E_T^{miss}) = 0.46 \cdot \sqrt{\sum E_T}$ [38]. The resolution is also affected adversely by minimum bias events. For each bunch crossing, there are 24 such minimum bias events which together contribute ~12 GeV to $\sigma(E_T^{miss})$.

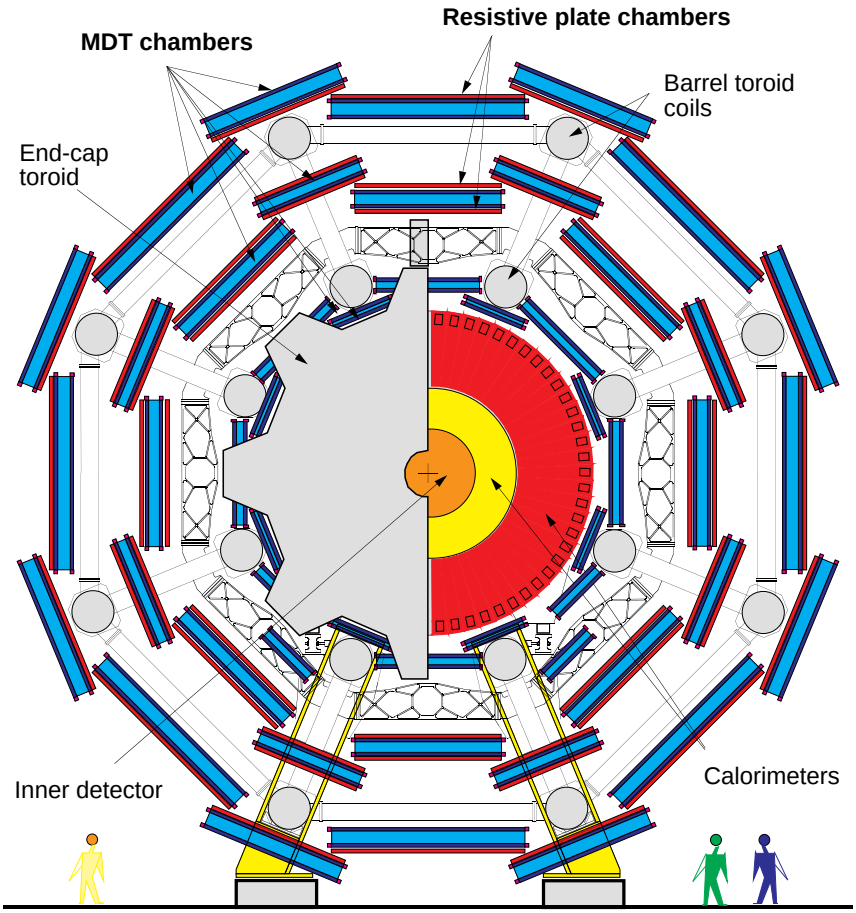

Figure 3.4: Transverse view of the ATLAS detector with components of the muon spectrometer shown.

3.3 Muon Spectrometer

Charged particles that are not contained by the calorimeters are detected in the muon spectrometer [46]. The spectrometer consists of trigger chambers, precision tracking chambers and its own magnet system so that momentum measurements can be made independently of the inner detector. The various elements of the muon spectrometer in relation to the rest of experiment can be seen in Figures 3.5 and 3.4 [46].

The magnetic fields of the muon spectrometer are provided by large superconducting toroids in the barrel region ($|\eta| < 1.0$) and the endcap region ($1.4 < |\eta| < 2.7$). Particles traveling in the "transition region" between the barrel and the endcap will experience

the fields from both magnets.

3.3.1 Tracking Chambers

Precision measurements of the muon tracks in the region $|\eta| < 2$ are made by three stations of monitored drift tubes (MDT). The stations in the barrel region are located between positions approximately 4.5 m and 10.5 m away from the beam axis. Each station consists of 3 layers of tubes mounted on both sides of an spacer frame as seen in Figure 3.6 [46]. The tubes are 30 mm in diameter and have a 50 μm W-Re wire in the center. A gas mixture of Ar(93%) and CO_2(7%) at a pressure of 3 bar is used.

Cathode strip chambers (CSC) are used for tracking in the region $2.0 < |\eta| < 2.7$ because they can better handle the higher rates and radiation found in the forward region. The CSCs are multi-wire proportional chambers where the cathode strips are read out. The gas mixture used is Ar(30%), CO_2(20%) and CF_4(20%). The position resolution is expected to be 80 μm [47]. The drift time is $\approx$30 ns. The time resolution is 7 ns, so hits in the chamber can be identified with specific bunch crossings.

3.3.2 Trigger Chambers

The muon system has dedicated detectors to trigger on events with muons. Resistive plate chambers (RPC) are used in the barrel region for this purpose. These chambers provide a position resolution of 1 cm which allows the trigger to discriminate on the basis of momentum; the time resolution is 1 ns, which is small compared to the time between bunch crossings (25 ns).

Thin gap chambers (TGC) are used for the muon trigger in the endcap region. They are similar to MWPCs in their design and serve two purposes. The anode wires aligned parallel to the MDT tubes are used to provide the trigger. Readout strips that are

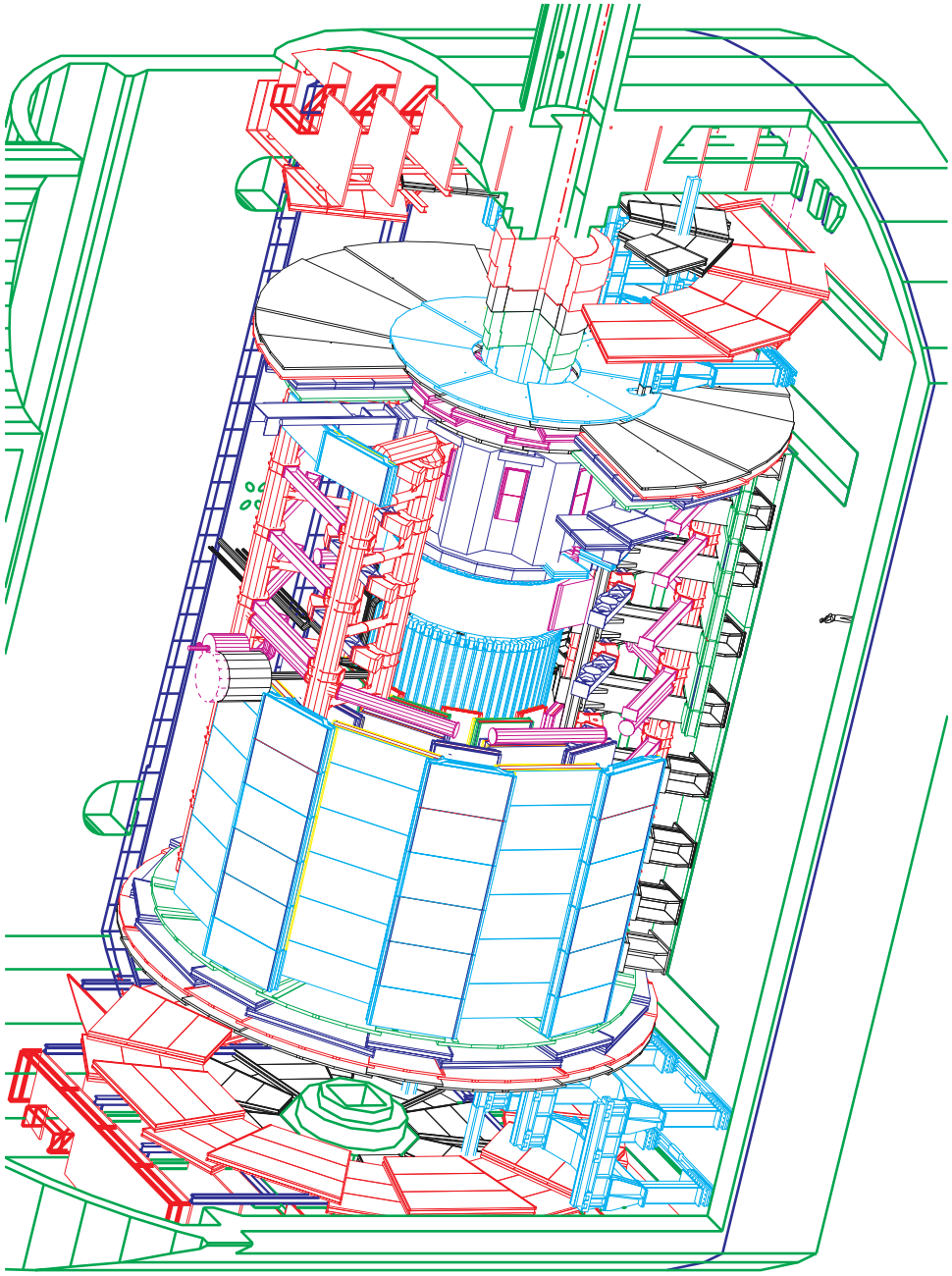

Figure 3.5: The ATLAS spectrometer with a cutaway view of the muon spectrometer.

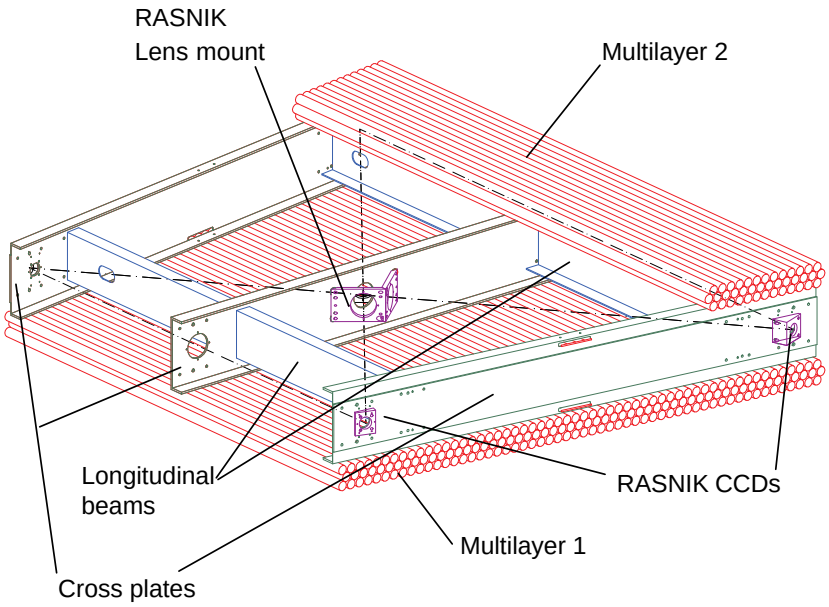

Figure 3.6: Schematic view of an MDT from the endcap region. A RASNIK system is built into the spacer frame to monitor changes in alignment over time.

aligned orthogonal to the anode wires are used for the azimuthal measurement of the muon tracks.

3.3.3 Alignment

A RASNIK system will monitor any change in position of the precision chambers over time. Lenses and CCDs are built into the frames for the MDT chambers (see Figure 3.6 for an example). This system will be able to detect displacements as small as 10 μm.

Measurements of displacements of chambers relative to each other will be performed with bars incorporating RASNIK and a method using transparent silicon strip sensors [48].

The ultimate goal is for sagitta measurements to have a precision of 50 μm. For comparison, a 1 TeV muon at $\eta = 0$ has a sagitta of 500 μm. The alignment system will be able to correct displacements of up to 1 cm. Initial calibration of the alignment system will be done with straight tracks in runs where the magnets are turned off.

3.3.4 Combined Performance with Inner Detector

The muon system and inner detector reconstruct tracks independently. It is advantageous to match tracks found in both systems to identify the origin of a muon because often one wants to reject those coming from K and π in-flight decays and secondary interactions.

For muons with $p_T < 10$ GeV/c, the momentum is best measured in the inner detector and in the muon system for $p_T > 100$ GeV/c. In the intermediate range, the resolutions are approximately the same and are less than $\approx$2%. Corrections to account for the energy loss in the calorimeters must be taken into account both for the momentum measurement and for track matching.

3.4 Trigger

The trigger system of ATLAS [49, 50] is designed to ensure that events of physical interest are collected for study. The beam crossing rate of 40 MHz means that the trigger making decision must be fast as well as effective. To accomplish this goal, ATLAS has a three tier trigger system described below.

The first level trigger (LVL1) reduces the rate at which events are accepted to less than 75 kHz and reduced further to $\sim$1 kHz at the second level. The third level of the trigger system is known as the Event Filter (EF).

A level one trigger decision is made in the central trigger processor (CTP) which receives information from the calorimeter trigger (L1CALO) and the muon trigger (L1MUON). The L1CALO determines the multiplicities and thresholds of

- (EM) photons/electrons
- (TAU) τ/hadrons
- (FJ) forward jet

and calculates

- (TE) total transverse energy
- (XE) missing transverse energy
- (JE) transverse energy from the jets only

The L1MUON uses the RPCs and TGCs to determine the multiplicities of 6 transverse momentum thresholds for muons. L1MUON and L1CALO produce regions of interest (RoI) that indicate the location in η and ϕ of the objects they have found. The CPT is also able to have up to 256 trigger signatures (logical combinations of the input from L1MUON and L1CALO) in its trigger menu. When a level one accept is produced, the second level trigger can proceed processing the event.

The second level trigger (LVL2) gets the trigger type from the CPT as well as the information from L1MUON and L1CALO. In addition, LVL2 uses the RoI information to request additional information from the read out systems for data close to the objects of interest. A LVL2 trigger decision has to be made in 10 ms, so the full detector readout is not used. Characteristics from the RoIs are collected and compared against a menu of signatures; if a match is made, the event is accepted at LVL2.

Full event information is given to the EF for events that pass LVL2. The decision to accept an event is similar to that of LVL2 except a more refined analysis can be made incorporating all the data available. Events passing the EF are written to disk for analysis. Trigger thresholds can be adjusted so selected events are output of the Event Filter (third level trigger) at a rate of 200 Hz regardless of the luminosity. For every event accepted, 1.5 MB is expected to be written to disk.

A large quantity of data will result even after a short period of running at ATLAS. These data will be separated into subsets containing events which are of interest to the various physics subgroups, such as the one working on top physics.

3.5 Initial Detector Configuration

A number of components will be missing from the detector when the first beam is produced in 2007. The middle layer of the pixel detector will not be present which means that b-jet identification will suffer [51]. The TRT wheel "C" is another inner detector component that will be missing. The muon spectrometer will not include the "EE" MDT chambers in the region $|\eta| = 1.0 - 1.3$ affecting the momentum resolution in that region discontinuously over the range in ϕ [52]. Also missing will be half of the CSC chambers affecting the region $|\eta| > 2$. It is foreseen that the full detector as envisioned will eventually be completed.

Chapter 4

Monte Carlo Event Generation and Simulation

A simulation was used to determine how effectively the ATLAS spectrometer can measure ΔN_{LR}, and the detector response to the relevant physics processes. This chapter describes the detector simulation and the methods used to create the data for signal and background events.

4.1 PYTHIA and ATLFAST

The PYTHIA program (Version 6.2) [53] was used to generate the necessary $t\bar{t}$ pairs and backgrounds needed for this study. The program simulates pp collisions and produces the final state of interest, decays particles with short lifetimes, and handles the evolution of outgoing partons into jets. For each event, the program produces a record that lists all of the final state particles along with their 4-momenta, as well as the coordinates of the vertex where each particle originated. This information is passed to a detector simulation program, which produces output that simulates what one would expect from the actual spectrometer.

The processes, $gg \to t\bar{t}$ and $q\bar{q} \to t\bar{t}$, are generated by PYTHIA separately. However,

there are two obstacles to overcome. First, PYTHIA does not have the ability to generate helicity correlated $t\bar{t}$ pairs as predicted the Standard Model, and second, a data set with non-zero ΔN_{LR} is needed. The strategies that were employed to generate CP violating datasets are described in Section 4.2.

ATLFAST [54] is the program that provides the fast simulation of the ATLAS detector. It takes the events generated by PYTHIA and returns values of particle momenta, jet energies, and missing E_T one expects from the fully operational ATLAS detector.

For each event, a calculation is performed to take particles from the list produced by PYTHIA to the location where they intersect with the calorimeter. The simulation assumes a uniform 2 T field. All the energy incident on a particular calorimeter cell is summed. The energy resolutions of each of these cells are parameterized as a function of p_T and η. The cell-level energy measurements are smeared based on results from the full simulation which is currently based on GEANT 4 [55]. Muons are treated similarly with their momentum smeared appropriately based on full simulation results.

For the reconstruction of jets, the cone algorithm [56] is used with a cone size of $\Delta R = \sqrt{(\Delta\eta)^2 + (\Delta\phi)^2} = 0.4$. Photons, electrons, and muons are determined to be isolated and not associated with a jet if they are a distance of $R > 0.4$ from the center of the jet in (η, ϕ) space.

The tagging of b-jets in the fast simulation is based on full simulation results where the b-tagging efficiencies are parameterized with respect to p_T and η of b-jets. The b-tagging efficiency for this study was $\epsilon_b = 60\%$, which gives a corresponding light-jet rejection factor of $\sim 10^2$.

The $t\bar{t}$ pairs were generated assuming the top mass is 175 GeV/c^2, which is close to the currently measured value from the Tevatron experiments. The true top mass may be different from this value by a few GeV/c^2; the effect on a ΔN_{LR} measurement is investigated in Section 6.5.6. Also, the CTEQ5L parton distribution functions [57] were used for this study.

4.2 Dataset Creation

PYTHIA suffers from two drawbacks that does not allow one to directly generate events suitable for this study. The correct physical helicity correlations are not included, and, more importantly, PYTHIA cannot generate data with a non-zero value of ΔN_{LR}. The first issue could have been addressed by supplying suitable matrix elements in the program, but the second issue would still remain because the matrix elements would have to be specific to a particular model and a model independent result is desired.

Both of these problems are handled by noting that the decay products from top quarks have angular distributions with relation to the top helicity in the top rest frame according to Equation 2.2. Top pair events generated with PYTHIA have $\alpha = 0$ resulting in a uniform distribution in $\cos\theta$. The acceptance–rejection method [58] was then used to select events so that the resulting angular distribution for l^+ and the $\bar{d}$, $\bar{s}$ anti-quarks followed $(1/2)[1 + \alpha\cos\theta]$ with $\alpha = -1$ or $+1$ depending on the top quark helicity that was desired.

The acceptance-rejection method is briefly described as follows: consider a uniform distribution $h(\cos\theta)$ from which, for example, a distribution $f(\cos\theta) = (1/2)[1+\cos\theta]$ is desired. First, generate an event from $h(\cos\theta)$ and obtain the $\cos\theta$ for that event. Then, that value of $\cos\theta$ is used to calculate $f(\cos\theta) = (1/2)[1+\cos\theta]$. A random number u is then generated in the interval [0,1] and the event is accepted if

$$2u < f(\cos\theta). \tag{4.1}$$

The factor of 2 is required since the domain of $\cos\theta$ covers the interval [-1,1].

The same procedure was also applied the anti-top in each event. As a result, separate sets of data were created that were entirely $t_R\bar{t}_R$, $t_L\bar{t}_L$, $t_L\bar{t}_R$ and $t_R\bar{t}_L$ top pair polarizations. This selection procedure was performed on all $t\bar{t}$ events and was not limited to the dilepton and lepton-plus-jets channels, because $t\bar{t}$ events with final state τ leptons, for

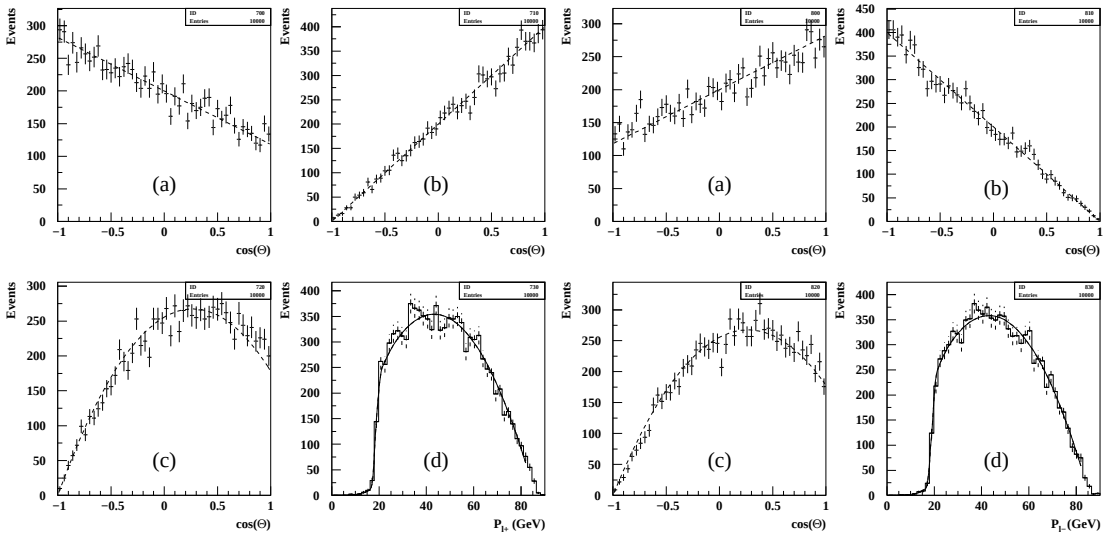

Figure 4.1: Several distributions from the $t_R\bar{t}_R$ data set that confirm events were generated properly: (a) the angle between the b quark momentum and the spin of the top in the top rest frame, (b) the angle between the lepton momentum and the spin of the top in the top rest frame, (c) the angle between the lepton momentum and the b momentum in the W rest frame, and (d) the lepton momentum in the top rest frame. Distributions for the l^+ and l^- are shown on the left and right, respectively. The solid lines show the expected distributions.

example, contribute to the background.

A number of distributions of kinematic variables were checked to ensure that no anomalies were introduced by this procedure. A number of these distributions are shown in Figure 4.1 for leptonically decaying top quarks. Figures 4.1(a) and (b) show that leptonically decaying tops are generated correctly according to Equation 2.2. Figure 4.1(c) shows the distribution of the angle between the lepton and the b-quark in the W rest frame, which at tree level is given by [59]

$$\frac{1}{N}\frac{dN}{d\cos\theta} = (\frac{3}{4})\frac{m_t^2(1-\cos^2\theta) + m_W^2(1+\cos\theta)^2}{m_t^2 + 2m_W^2}. \tag{4.2}$$

Figure 4.1(d) shows the momentum distribution for leptons in the top rest frame. The theoretical distribution assumes the leptons to be massless, which is a good approximation in this case [60]. The correct distributions were also observed for hadronically decaying

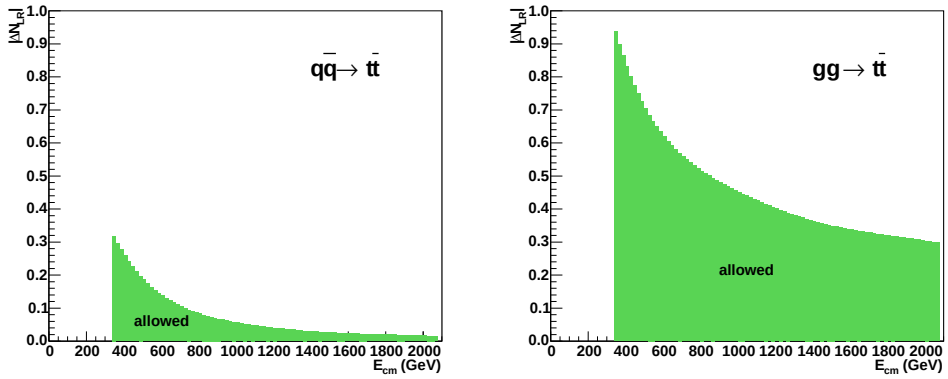

Figure 4.2: Maximum value of ΔN_{LR} as a function of the center of mass of the $t\bar{t}$ system for $q\bar{q} \rightarrow t\bar{t}$ and $gg \rightarrow t\bar{t}$ assuming correlation factors given in Figure 2.2.

$t\bar{t}$ pairs.

The correct number of $t_R\bar{t}_R$, $t_L\bar{t}_L$, $t_L\bar{t}_R$ and $t_R\bar{t}_L$ events were selected to create datasets, each corresponding to various values in ΔN_{LR} and integrated luminosity. The correct distributions in $\sqrt{s}$ and the correlation factor, C, were maintained according to Figure 2.2.

One limitation with the creation of CP violating datasets is that an arbitrarily large value of ΔN_{LR} cannot be chosen. Since the number of correlated pairs cannot exceed $N_{RR} + N_{LL}$, it follows that the difference in the number of correlated pairs, $N_{RR} - N_{LL}$, cannot exceed the total,

$$N_{RR} + N_{LL} \; > \; |N_{RR} - N_{LL}|. \tag{4.3}$$

Given the correlation factor in Figure 2.2, the maximum allowed values of ΔN_{LR} as a function of $\sqrt{s}$ are shown in Figure 4.2. The cross section for $t\bar{t}$ production is dominated by $gg \rightarrow t\bar{t}$, so ΔN_{LR} can potentially take quite large values if nature chooses. It will be seen that even values of ΔN_{LR} less than 10% can easily be seen in the ATLAS experiment.

A number of data sets corresponding to integrated luminosities up to 30 fb^{-1} were created. Since a general, model independent scenario was desired, data sets were created

such that a constant fraction, k, of the maximum allowed value of ΔN_{LR} would be realized over the entire range of $\sqrt{s}$. This results in an average value of ΔN_{LR} for a given set of data that is related to k as

$$\Delta N_{LR} = 0.663k. \tag{4.4}$$

The advantage of this approach is the ability to create datasets with values of ΔN_{LR} up to the maximum allowed value permitted by the correlation coefficient. Otherwise, at large center of mass energies, moderate values of ΔN_{LR} become impossible as the difference $|N_{RR} - N_{LL}|$ becomes larger than the total number of correlated pairs $N_{RR} + N_{LL}$. The use of this method, however, means that ΔN_{LR} is not constant over $\sqrt{s}$. Figure 4.3 shows the dependence of ΔN_{LR} for the $q\bar{q} \to t\bar{t}$ and $gg \to t\bar{t}$ processes and for the dataset as a whole using $\Delta N_{LR} = 0.10$ as an example. The largest contribution is from the gluon-gluon process because it has the largest cross-section.

In Section 5.4, the question regarding the ability to measure the CP-violating Peskin-Schmidt signal in the dilepton channel is briefly investigated. The dataset used was created using the events with pure helicity states, but with the ΔN_{LR} dependence on center of mass energy found in Figure 2.4.

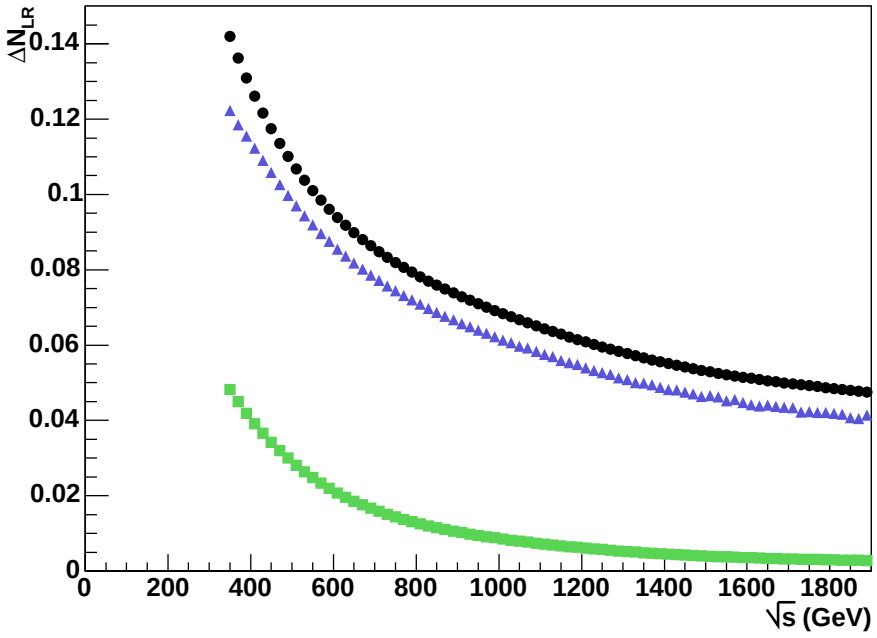

Figure 4.3: Value of ΔN_{LR} as a function of center of mass energy when a constant fraction of the maximum allowed value of ΔN_{LR} is taken over the range of $\sqrt{s}$ for $q\bar{q} \to t\bar{t}$ (green squares), $gg \to t\bar{t}$ (black circles) and for both processes (blue triangles). The value of ΔN_{LR} used in this example is 0.10.

Chapter 5

Observing CP Violation in the Dimuon Channel

The dilepton channel of $t\bar{t}$ decay provides one method of observing non-zero values of ΔN_{LR} in top pair production. In this case, the asymmetry in p_T between positively and negatively charged leptons is taken; finding that this asymmetry is different from the null result indicates that CP is violated.

Peskin and Schmidt (PS) suggested that a non–zero ΔN_{LR} might be detected using the dimuon channel because it provides a clean signature with little background [32]. In fact, the lepton-plus-jets channel will have a larger S/B ratio. Another disadvantage is the branching ratio for $t\bar{t}$ into the dimuon channel ($\approx$1/81) is small. Using both muons and electrons increases the branching ratio to $\approx$4/81. Following Peskin and Schmidt, only muons are considered in this section, but it will be clear that the PS signal is too small to observe in either case.

The focus on this section is on determining the set of cuts that, when applied to dimuon channel events, a large signal-to-background ratio and efficiency is obtained.

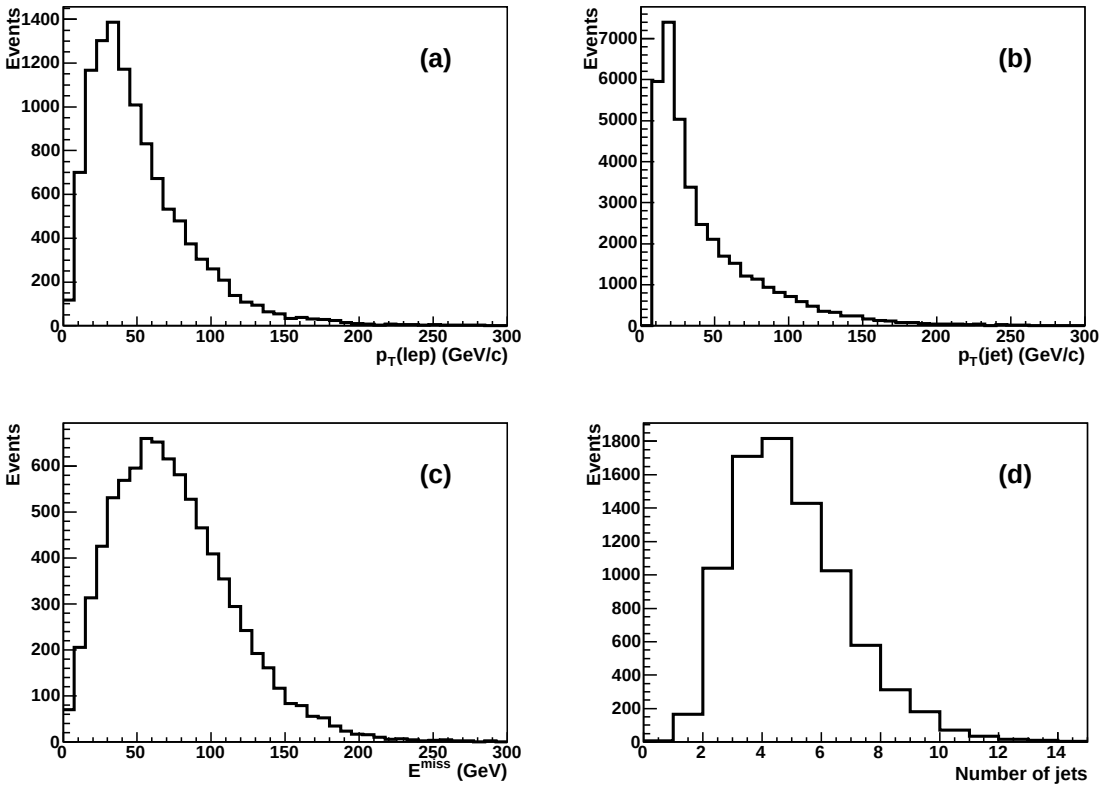

Figure 5.1: Distributions characterizing dilepton signal events: (a) the transverse momentum distributions of the leptons, (b) the transverse momentum distributions of jets, (c) the missing transverse energy distribution, and (d) jet multiplicity.

5.1 Signal Event Topology

The dilepton channel of top pair decay will contain two oppositely charged leptons, two b-jets, and missing energy due to the two neutrinos escaping detection. Distributions of some kinematic variables from this channel are shown in Figure 5.1.

The $t\bar{t}$ system cannot be reconstructed in this channel, so event selection must entirely be based on selecting events with the aforementioned topology with appropriate kinematic cuts. The variables used in event selection are

$$E_T^{\text{miss}}, \tag{5.1}$$

$$p_T(\mathrm{b-jet}), \tag{5.2}$$

$$|m_{\mu\mu} - m_Z|, \tag{5.3}$$

$$\text{and } \ p_T(\mu). \tag{5.4}$$

It will be seen that the backgrounds are difficult to reduce without making hard cuts, and thereby reducing the signal efficiency considerably. To reduce the background from $Z \to \mu\mu$ events, a cut is made so that $m_{\mu\mu}$, the invariant mass of the two muons, is not close to m_Z. The b-jets are also required to have $|\eta| < 2.5$. The effect of different cuts in these variables on efficiency and signal-to-background ratios is investigated later in this chapter.

5.2 Backgrounds

Several processes have similar characteristics to dimuon events and may pass the selection criteria. The background does not contribute to the asymmetry, but will instead will add to the number of events accepted, and therefore reduces the statistical sensitivity.

Table 5.1 lists the processes contributing to the background. These processes can produce muons, missing energy and jets that may be falsely tagged as b-jets. Their cross-sections can also be very large relative to the $t\bar{t}$ production cross-section of $\sim 8 \times 10^5$ fb, so even if a small fraction of background events pass the selection cuts, they cannot be neglected. It is therefore useful to investigate how many signal and background events remain for a given set of selection criteria.

The background events were generated by PYTHIA, and were processed in ATLFAST using the same configuration for the simulation of the $t\bar{t}$ signal events.

BG Process	Cross-section (fb)
$gg, q\bar{q} \to b\bar{b}$	3×10^{11}
$qg \to Wq'$	1.3×10^{8}
$q\bar{q}' \to Wg$	1.6×10^{8}
$qg \to Zq$	6.3×10^{7}
$q\bar{q} \to Zg$	6.4×10^{7}
$q\bar{q} \to WW$	2.5×10^{4}
$q\bar{q}' \to WZ$	2.5×10^{4}
$q\bar{q} \to ZZ$	1.0×10^{4}
$gg, q\bar{q} \to t\bar{t}$ (non-dimuon)	7.6×10^{5}

Table 5.1: Backgrounds to the dimuon channel signal. The cross-sections listed are tree level values for pp collisions at a center of mass energy of 14 TeV.

5.3 Effect of Cuts on S/B and Signal Efficiency

A straightforward way to determine the best cuts to apply for event selection is to generate and simulate the appropriate number of events for a given integrated luminosity and then find the set of cuts that maximizes the number of signal events to the number of background events. However, two problems arise: First, the cross-sections of some background processes is very large, and the fraction of events that pass a given set of cuts is low. Generating an extremely large number of events was not practical. An integrated luminosity of 10 fb^{-1}, for example, yields $\sim10^{12}$ $b\bar{b}$ events, but a 1000 MHz computer can only generate approximately 2×10^{9} events per year. It is impossible to generate sufficient events corresponding to the integrated luminosity expected for a year at the LHC with modest computing resources.

Second, there are several variables that are be used in the selection criteria. To evaluate S/B and efficiency for n variables and m cuts on each of those variables, all of

the signal and background events generated must be read for each cut, and if there are n variables and m cuts on each of those variables, then the data must be read $m \times n$ times. If there is a large number of events to be analyzed, this method is not practical. It is usually possible to take a subset of data and get a reasonable answer, but for processes with large cross-sections and a low probability to pass the selection cuts, one is faced with trying to make conclusions based on low statistics.

It was necessary to develop methods to estimate the number of events passing cuts in kinematic regions where there are no events in a small, limited sample. One method for determining S/B in an efficient manner is presented in the next sections.

5.3.1 Cut Matrix Method

The method presented below addresses the problem where one has a large number of events, and wishes to evaluate S/B and the efficiency for several sets of cuts.

The variables on which cuts are to be applied can be considered to form a multi-dimensional space. A cut can be considered as a partitioning of this space into two regions that are not necessarily connected, where events are accepted in one region, and rejected in the other. The object is to determine where to place this partition in an efficient manner.

The method can best be illustrated if cuts on two variables, A and B are considered, but can be easily generalized to many variables. Figure 5.2 shows a possible cut on both of these variables. If an event falls into a bin defined by $[A_i, A_{i+1}]$ and $[B_j, B_{j+1}]$, the value in that bin, N_{ij}, is increased by one or the weight of the event, as the case may be. The data collection is then processed event by event exactly once and the resulting bin totals N_{ij} are stored. After the data set is evaluated in this way, it is easy to determine the number of events, N_{pass}, passing cuts $A > A_i$ and $B > B_j$ which is given by

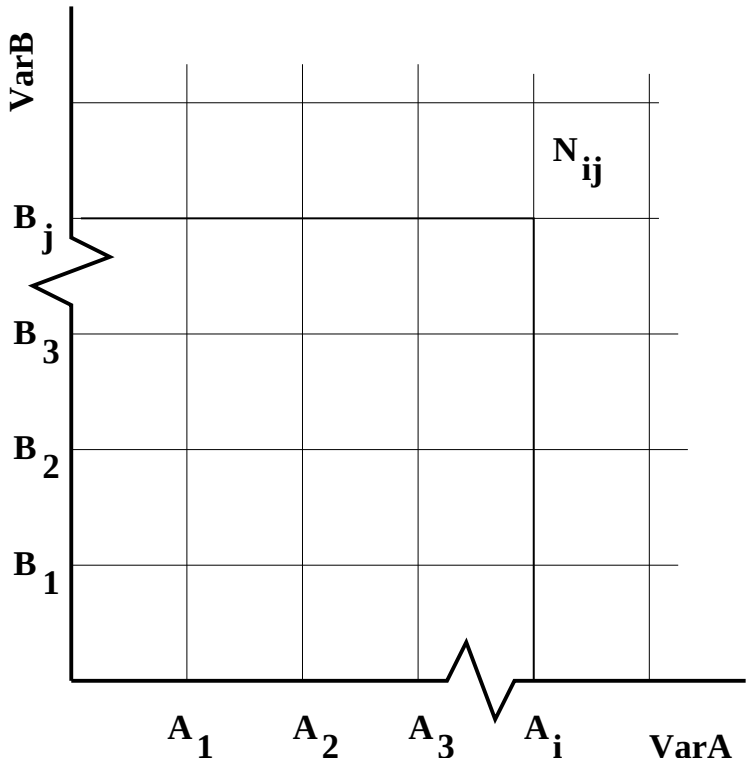

Figure 5.2: Illustration of the cut matrix method shown for two variables. One passes over a data set counting the number of events N_{ij} with a value in variable A in the interval $[A_i, A_{i+1}]$ and variable B in the interval $[B_j, B_{j+1}]$ for all i, j.

$$N_{pass} = \sum_{i,j<k,l} N_{kl}. \tag{5.5}$$

Therefore, instead of repeatedly processing a collection of events to determine an optimal set of cuts, one only needs to access the data once.

This method was applied to the signal and each of the background processes listed in Table 5.1 and the S/B was determined for a number of cuts in the variables in Equations 5.1–5.4.

It is often the case the cut variables are not independent of each other. However, one is not restricted to looking at the effect of making rectilinear cuts as in Equation 5.5. The A-B plane can be separated into two arbitrary regions and the total of the N_{ij} in the region passing the cut can be summed. In the case where the regions do not follow along

the boundaries of each bin but crosses in at some place in the middle, one must make an approximation. For example, if only 20% of a bin is accepted, the corresponding fraction of N_{ij} can be taken. Also, more accurate results can be achieved using smaller intervals in A and B.

5.3.2 Backgrounds with Large Cross-sections

Some of the background processes in Table 5.1 have very large cross-sections which makes it impractical to generate enough events even for a few fb^{-1} of integrated luminosity. This makes it difficult to determine the number of background events for some of the cuts that are applied to determine the best S/B. For example, muons from B meson decay in $b\bar{b}$ events have a low p_T distribution, and few events pass higher cuts in p_T. There could be a significant number of events passing the p_T cut if a large integrated luminosity is considered. Also, if only a few events pass, extrapolating to 10 fb^{-1} would mean a very large uncertainty in the number of events.

One way of dealing with a problem like this is to configure PYTHIA so that only certain decay modes are allowed and final state particles are limited to smaller regions in phase space. However, in the case of $b\bar{b}$ production, muons may come from decaying B-mesons. Generating $b\bar{b}$ events with a high limit on center of mass energy may exclude high p_T muons from low center of mass energy events.

It is still possible to get a reasonably good estimate of background events for larger cuts. Figure 5.3 illustrates how the number of events accepted was estimated for hard cuts. Letting $N_A(N_B)$ be the number of events that pass a cut in variable $A(B)$, the probability that an event passes the cut in A and B is

$$P_A = \frac{N_A}{N_{TOT}} \qquad P_B = \frac{N_B}{N_{TOT}}, \tag{5.6}$$

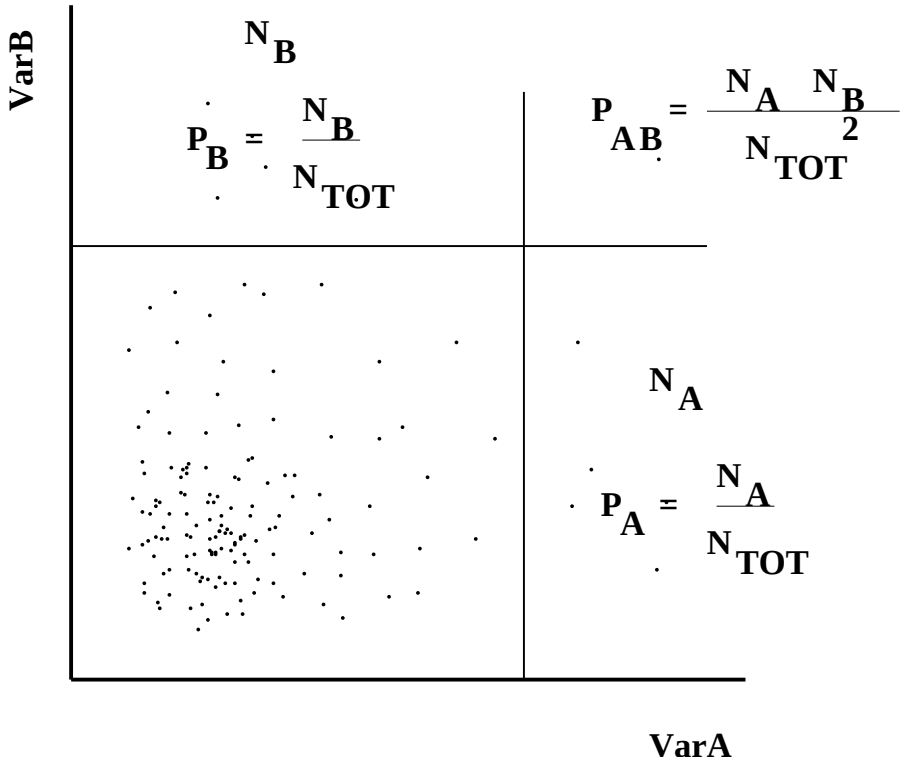

Figure 5.3: Illustration of method to estimate the number of events passing cuts in two variables.

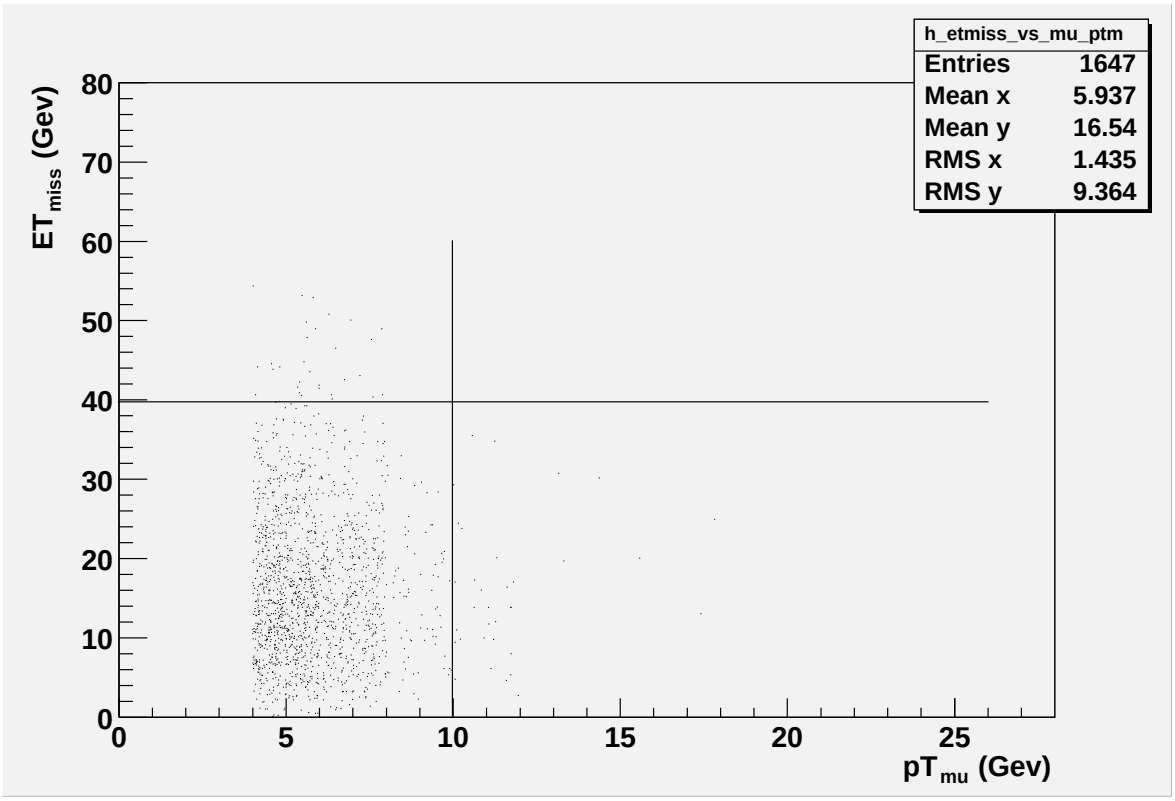

Figure 5.4: Missing transverse energy versus $p_T(\mu)$ for $b\bar{b}$ events with $p_T(\text{jet}) > 14$ GeV/c and $|m_{\mu\mu} - m_Z| > 10$ GeV/c^2. The predicted number of events passing the cuts shown is 0.92.

respectively, where N_{TOT} is the total number of events. The probability of an event passing *both* cuts is then $P_A \cdot P_B$ if there is no correlation between the variables chosen. The number of events, N_{est} estimated to be found passing both cuts is then

$$N_{\text{est}} = N_{TOT} \cdot \frac{N_A}{N_{TOT}} \frac{N_B}{N_{TOT}} = \frac{N_A N_B}{N_{TOT}}. \tag{5.7}$$

This method was tested with cuts loose enough such that several events passed both cuts allowing for a comparison with the calculated estimate. Figure 5.4 shows the distribution of E_T^{miss} for a number of $b\bar{b}$ events where two b-jets and two oppositely charged muons with $|\eta| < 2.5$. A comparison between the predicted number of events passing various cuts to the actual number is shown in Table 5.2.

The processes for which this method was applied are listed in Table 5.3 along with the variables used to make the estimate and the corresponding correlation coefficient.

Cut Variable		Predicted	Actual
E_T^{miss} (GeV)	$p_T(\mu)$ (GeV/c)		
10	8	74.8	82
10	10	23.2	21
15	12	2.2	2
25	9	12.7	11
10	8	570	552

Table 5.2: Comparison of predicted and actual number of $b\bar{b}$ events for several cuts with a small correlation coefficient.

The cross-sections of remaining background are small, and therefore did not require this treatment.

5.3.3 Results for the Dimuon Channel

The maximum value for S/B was found to be 12.1 with a corresponding efficiency of 2.3% for signal events. These values were obtained with the following cuts:

$$E_T^{miss} > 45 \text{ GeV}, \tag{5.8}$$

$$p_T(\text{jet}) > 40 \text{ GeV/c}, \tag{5.9}$$

$$|m_{\mu\mu} - m_Z| > 20 \text{ GeV/c}^2, \tag{5.10}$$

$$p_T(\mu) > 50 \text{ GeV/c}. \tag{5.11}$$

$$\tag{5.12}$$

The resulting S/B ratios are shown in Figure 5.5 as a function of several different cut variables. Only two out of the four variables can be shown on each 2-dimensional plot. For variables not shown, their value are fixed to their value in Equations 5.8–5.11, so the

BG Process	Variables	Correlation Coeff.
$f\bar{f} \to gZ$	E_T^{miss} and p_T(jet)	0.134
$f\bar{f}' \to gW$	E_T^{miss} and $p_T(\mu)$	0.022
$fg \to f'W$	E_T^{miss} and $p_T(\mu)$	0.088
$fg \to fZ$	E_T^{miss} and p_T(jet)	0.138
$f\bar{f} \to Z$	E_T^{miss} and $p_T(\mu)$	0.008
$f\bar{f}' \to W$	E_T^{miss} and $p_T(\mu)$	-0.056
$f\bar{f}, gg \to b\bar{b}$	E_T^{miss} and $p_T(\mu)$	-0.016

Table 5.3: List of background processes with large cross-sections for which an estimation of the number of events were made. The estimation was based on the variables listed. The correlation coefficient for between the two variables used are given.

same maximum S/B of 12.1 is obtained in every plot.

A study [61] which used less restrictive cuts in the same variables obtained a value of $S/B = 8.7$. It is apparent that the signal-to-background improves with tighter cuts.

The corresponding signal efficiencies as a function of selected pairs of variables are presented in Figure 5.6. It can be seen that the signal efficiency is most sensitive to the p_T of the muon and least sensitive to $|m_{\mu\mu} - m_Z|$.

5.4 Momentum Asymmetry for the Peskin–Schmidt Signal

The ability of ATLAS to make a measurement of the Peskin–Schmidt signal using the dimuon channel was investigated. In this model, the maximum value of ΔN_{LR} is 0.3% averaged over all $\sqrt{s}$. This is the smallest value of ΔN_{LR} of all the theories presented, but it is examined because Peskin and Schmidt proposed this method of detecting CP violation in $t\bar{t}$ production.

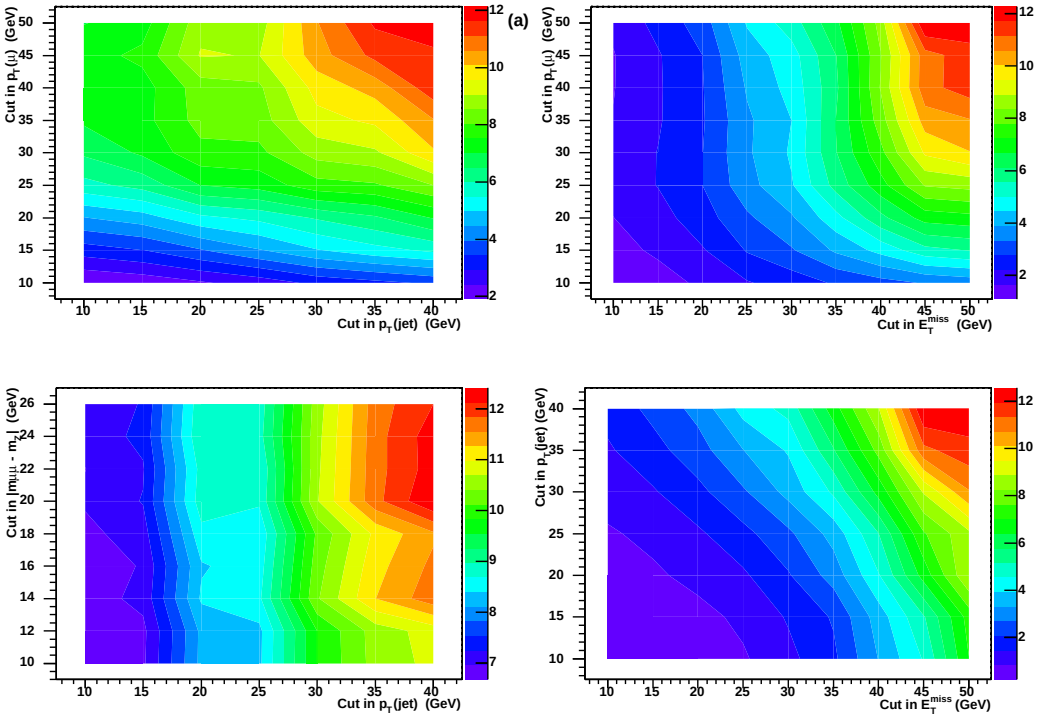

Figure 5.5: The signal-to-background ratio in the dimuon channel for various cuts. The quantities not shown on the axes were fixed to their value in Equations 5.8–5.11, so the same maximum S/B of 12.1 is obtained in every plot.

Figure 5.7 shows the normalized asymmetry in transverse momenta between μ^+ and μ^- corresponding to an integrated luminosity of 500 fb^{-1}. The data shown are MC truth values with no cuts applied and no backgrounds included. Comparing this result with the null hypothesis of $\Delta N_{LR} = 0$, $\chi^2 = 13.4$ (NDF = 20) is obtained. Only muons were used for this result. Assuming lepton universality, the equivalent result in the dilepton case will be that as shown in the figure, but with a corresponding integrated luminosity of 125 fb^{-1}. It is evident that an observation of CP violation due to the PS mechanism will not be achieved at the LHC.

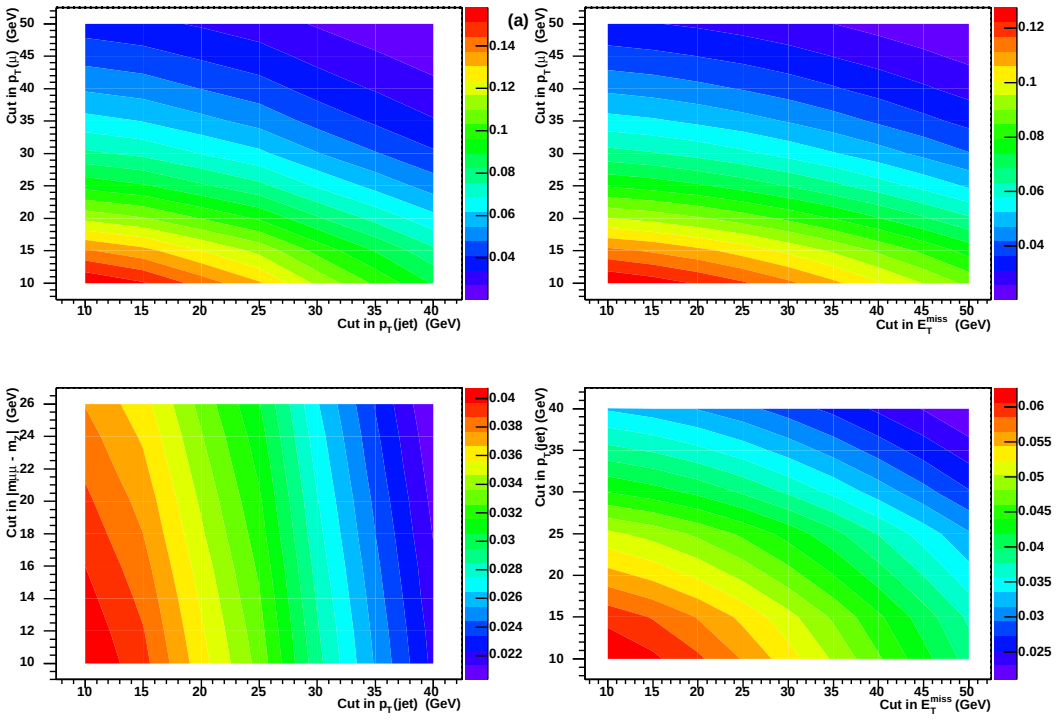

Figure 5.6: The signal efficiency in the dilepton channel for various cuts. The quantities not shown on the axes were fixed to their value in Equations 5.8–5.11, so the same maximum S/B of 12.1 is obtained in every plot.

5.5 Discussion

Cuts in several variables were investigated to determine signal-to-background ratios and signal efficiencies for $pp \to t\bar{t}$ events decaying to the dilepton channel. Methods were developed to reduce the computing time and to make estimates for backgrounds with large cross-sections. However, it is difficult to determine which cuts are the most useful. More restrictive cuts increase the signal-to-background ratio, but at the same time, decrease the signal efficiency. A better question is which set of cuts give the greatest sensitivity to the signal being investigated. This can depend on many factors, such as how well the detector is understood, and how much confidence one has in modeling the signal and backgrounds. This can only be achieved when real data is finally realized at the LHC, because the result will depend on systematic factors and not only on statistics alone.

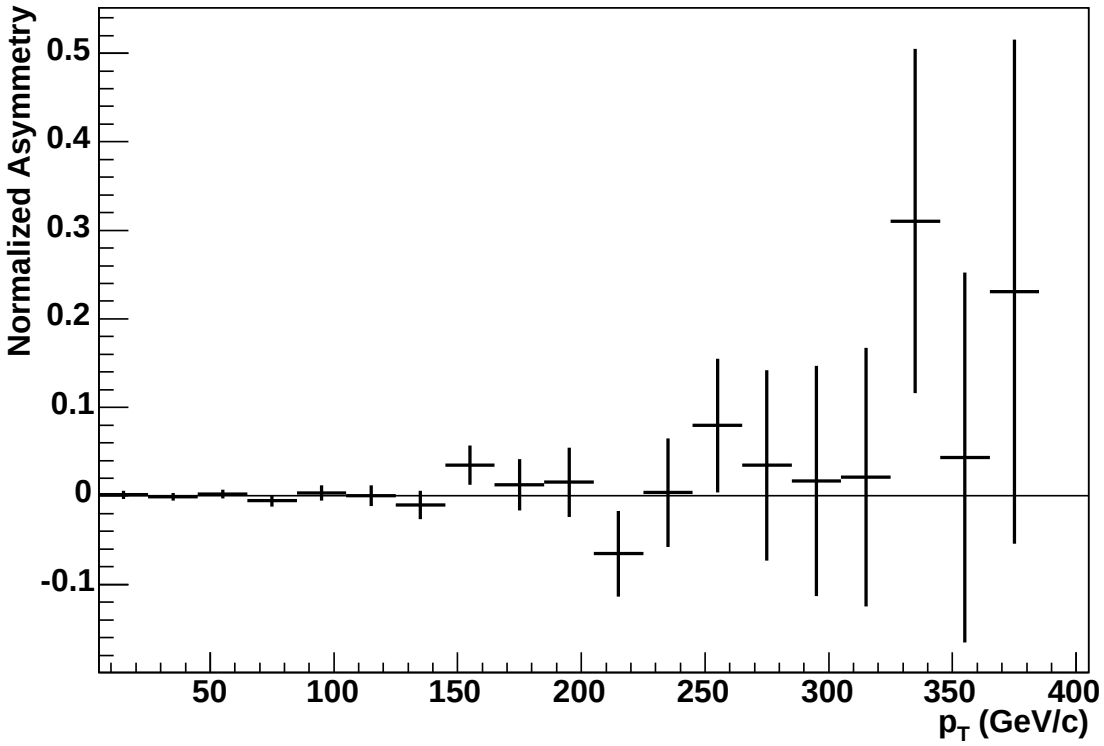

Figure 5.7: Normalized asymmetry in transverse momenta between μ^+ and μ^- for an integrated luminosity of 500 fb^{-1} for the maximum Peskin–Schmidt CP-violating signal of $\Delta N_{LR} = 0.3\%$, averaged over $\sqrt{s}$. These data are Monte Carlo truth values with no cuts applied and no background included.

The signal from the Peskin-Schmidt model was briefly investigated using the dimuon channel. This model predicts the maximum value of ΔN_{LR} to be 0.3%. It was found that the CP violating signal is too small to be seen at the LHC using the dimuon channel. A superior method for determining ΔN_{LR} is presented in the next chapter and it will be confirmed that the PS signal is too small to be detected in the expected lifetime of the ATLAS experiment.

Chapter 6

Measuring CP Violation in the Lepton-plus-Jets Channel

The lepton-plus-jets channel allows one to reconstruct the 4-momentum of both quarks in the $t\bar{t}$ system. The angle between the lepton momentum and the momentum of the leptonically decaying top, $\cos\theta$, can be determined directly for each event. Analysis of the resulting $\cos\theta$ distributions makes a measurement of ΔN_{LR} possible.

The measurement of ΔN_{LR} has been discussed as an ideal case in Section 2.4.2. However, there are a number of issues that arise when the measurement is made in a real experiment such as the ATLAS detector. The main concerns are background events and poor resolution in the $\cos\theta$ measurement. These will be discussed in the following sections.

This chapter first describes the event selection and reconstruction. Then, backgrounds to the lepton-plus-jets channel are discussed. The methods for correcting the $\cos\theta$ distributions are described next. Finally, some systematic errors are considered and results presented.

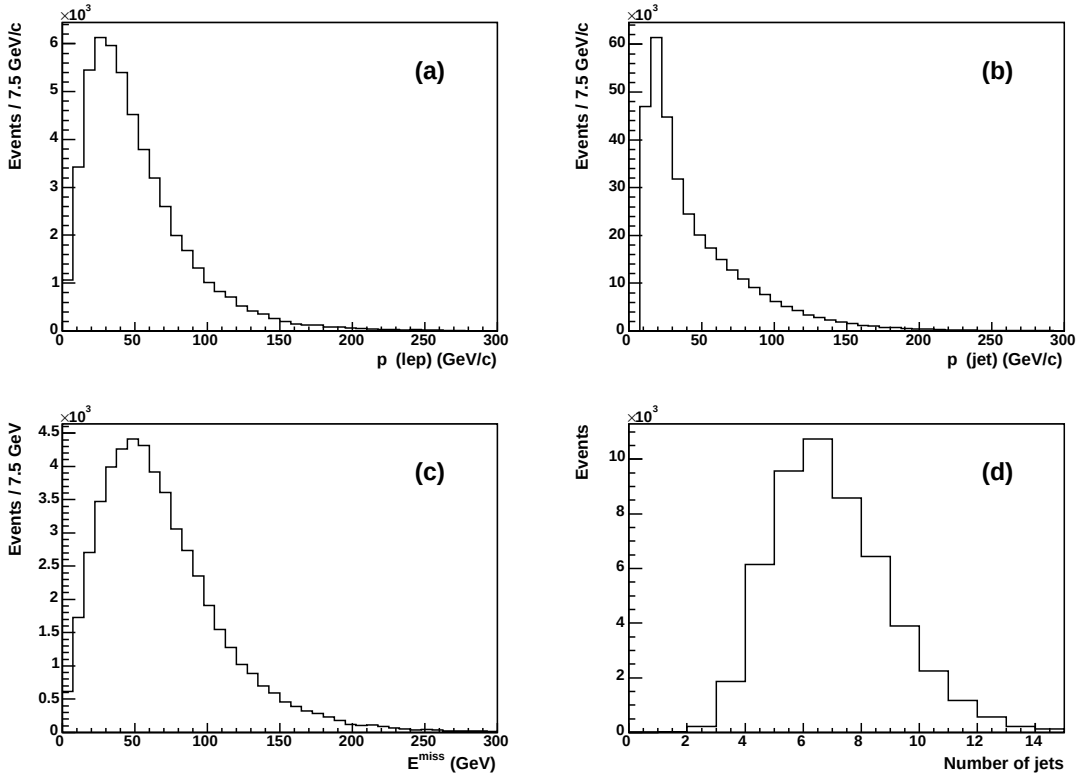

Figure 6.1: Distributions that characterize $t\bar{t}$ events decaying into the lepton plus jets channel: (a) the transverse momentum distributions of the leptons, (b) the transverse momentum distributions of jets, (c) the missing transverse energy distribution, and (d) jet multiplicity.

6.1 Event Selection and Reconstruction of $t\bar{t}$ Pairs

An event in which a $t\bar{t}$ pair decays into the lepton-plus-jets channel includes a lepton (e or μ), missing transverse energy due to the neutrino, and 4 jets of which 2 are tagged as b-jets. Distributions of these kinematic variables characterizing $t\bar{t}$ events are shown in Figure 6.1. Cuts to select $t\bar{t} \rightarrow (bl\nu)(bjj)$ events are based on these parameters. Additional cuts based on the assumption that a $t\bar{t}$ pair decays into the lepton-plus-jets channel are applied to increase the ratio of signal events to background events.

For an event to be selected as a lepton-plus-jets candidate, it must pass the following kinematic cuts. The event must have exactly one lepton with $p_T(l) > 20$ GeV/c in the final state, at least 2 light-quark jets and exactly 2 b-jets with $p_T(\text{jets}) > 40$ GeV/c, and

Cut	All $t\bar{t}$		l+jet events only	
	Remaining	Efficiency (%)	Remaining	Efficiency (%)
None	800000	100.0	234016	100.0
$p_T(l)$>20 GeV/c, $\|\eta\|$ <2.5 exactly one lepton required	207241	25.9	157771	67.4
p_T(jet)>40 GeV/c, $\|\eta\|$ <2.5				
at least 2 non b-jets	109564	13.7	90921	38.8
exactly 2 b-jets	10977	1.4	9513	4.1
E_T^{miss} >20 GeV	9842	1.2	8476	3.6
$\|m_{jj} - m_W^{PDF}\| < 20$ GeV	4368	0.55	3929	1.7
Sol'n for $p_z(\nu)$ exists	3417	0.43	3047	1.3
$\|m_{bjj} - m_t\| < 35$ GeV/c^2 $\|m_{bl\nu} - m_t\| < 35$ GeV/c^2	2527	0.32	2311	0.99

Table 6.1: Cuts used for the selection of lepton-plus-jets events with corresponding signal efficiencies in percent. The numbers for signal events only are shown on the right hand side. The size of the original $t\bar{t}$ sample used corresponds to an integrated luminosity of 1 fb^{-1}.

missing transverse energy of at least 20 GeV. All leptons and jets must also be in the central part of the detector with $|\eta| < 2.5$. After these cuts are applied, 3.6% of the initial number of lepton-plus-jets events remain. The top half of Table 6.1 shows the kinematic cuts and resulting signal efficiencies.

In order to increase the selectivity for $t\bar{t}$ events, an attempt is made to reconstruct the event assuming the top and anti-top quarks assuming the candidate $t\bar{t}$ pair decays into the lepton-plus-jets channel. Specifically, the two b-jets are assumed to be from the decays, $t \to W^+b$ and $\bar{t} \to W^-\bar{b}$, the missing energy and lepton are assumed to be from the decay $W \to l\nu$, and two light jets with an invariant mass closest to m_W are assumed

to be from $W \to jj$. If the reconstructed top masses are close to the best estimate of the true top mass m_t, the event is accepted.

First, a candidate for the hadronically decaying W is sought from the light jets in the event. The invariant mass, m_{jj}, is calculated from all combinations of two light jets. The value of m_{jj} which is closest to the world average for the W boson as reported by the Particle Data Group, m_W^{PDG}, is chosen. The event is tentatively accepted if two light jets are found with $|m_{jj} - m_W^{PDG}| < 20$ GeV.

Next, an attempt is made to determine the momentum of the neutrino from the leptonically decaying W boson. The missing transverse energy in the event is assumed to be entirely from the neutrino, $\vec{E}_T^{miss} = (E_x^{miss}, E_y^{miss}) = \vec{p}_T(\nu)$. A comparison between E_T^{miss} and the MC truth value of $p_T(\nu)$ is shown in Figure 6.2. Determining the z-component of the neutrino momentum is more difficult. The neutrino is assumed to be massless, and $p_{z\nu}$ can be found as one of the solutions of a quadratic equation obtained by assuming that the invariant mass of the lepton and neutrino must be that of a W ie. $m_{l\nu}^2 = m_W^2 = (p_l + p_\nu)^2$. The solutions for $p_{z\nu}$ are given by

$$p_{z\nu} = \frac{-ap_{zl} \pm \sqrt{a^2 p_{zl}^2 - p_{Tl}^2(a^2 - 4E_l^2/c^2)}}{2p_{Tl}^2}, \tag{6.1}$$

where

$$a = m_W^2 - m_l^2 + 2\vec{p}_{Tl} \cdot \vec{p}_{T\nu}, \tag{6.2}$$

and E_l, $\vec{p}_l = (p_{Tl}, p_{zl})$, m_l are the energy, momentum, and mass of the lepton, respectively. For this calculation, $m_W = m_W^{PDG}$ is used. One or two real solutions to the quadratic are required, otherwise the event is rejected at this point.

The invariant masses of the t and $\bar{t}$ are then calculated from all possible combinations of the two solutions for $p_{z\nu}$ and the two b-jets: $m_{bl\nu}^2 = (p_l + p_\nu + p_{bjet})^2$ and $m_{bjj}^2 = (p_{ljet} + p_{ljet} + p_{bjet})^2$. The combination that makes

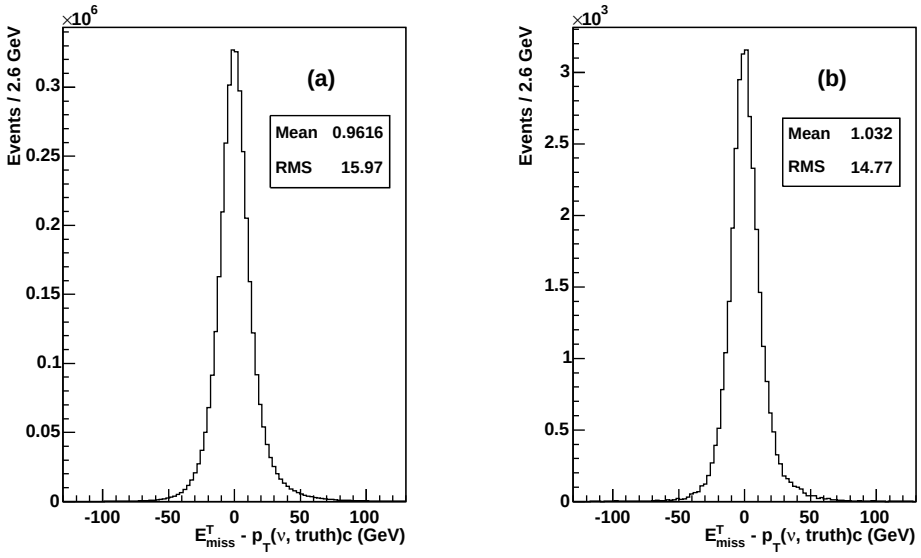

Figure 6.2: Comparison between E_T^{miss} and the generator level value of $p_T(\nu)$ is shown for (a) all lepton-plus-jets events and (b) only those lepton-plus-jets events which pass all selection cuts.

$$(m_{bjj} - m_t)^2 + (m_{bl\nu} - m_t)^2 \tag{6.3}$$

the smallest is taken. If $|m_{bjj} - m_t| < 35$ GeV/c^2 and $|m_{bl\nu} - m_t| < 35$ GeV/c^2, then the event is accepted as a lepton-plus-jets event. The top mass, m_t, is taken to be 175 GeV/c^2, which is the value used in the generation of the events. The effect of using different values of m_t in the reconstruction is addressed in Section 6.5.6. Figure 6.3 shows the distributions of the reconstructed top quark masses.

To determine $\cos\theta$ for each event, the lepton-neutrino-b-jet system is boosted into the top rest frame, assuming the mass of the top is 175 GeV/c^2. The angle θ is defined by

$$\cos\theta = \frac{\vec{p}_l^{\,*} \cdot \vec{p}_t^{\,*}}{|\vec{p}_l^{\,*}||\vec{p}_t^{\,*}|}, \tag{6.4}$$

where $\vec{p}_l^{\,*}$ is the momentum of the lepton in the top rest frame, and $\vec{p}_t^{\,*}$ is the momentum of the top in the lab frame. The latter is the direction in which the top must be boosted

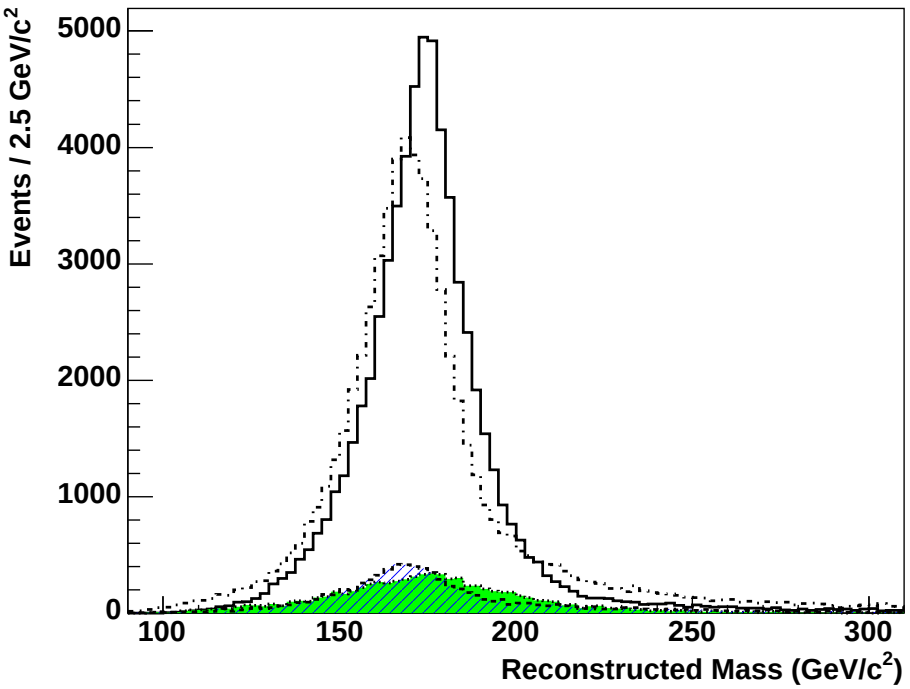

Figure 6.3: The reconstructed mass distributions $m_{bl\nu}$ (solid) and m_{bjj} (dash-dot). Events with $|m_{bjj} - m_t| < 35$ GeV/c^2 and $|m_{bl\nu} - m_t| < 35$ GeV/c^2 are accepted where $m_t = 175$ GeV/c^2. The $t\bar{t}$ backgrounds for $m_{bl\nu}$ and m_{bjj} are shown by the dotted and dashed lines, respectively.

to go from rest to the lab frame. The direction of this vector defines the axis from which $\cos\theta$ is found. The charge of the lepton determines whether it originated from the top quark or the anti-top quark of the $t\bar{t}$ pair.

Figure 6.4 shows the distribution in $\cos\theta$ of positively charged leptons for an integrated luminosity of 30 fb^{-1} and $\Delta N_{LR} = 0$. The original distribution is flat, but the event selection cuts introduce distortions. The low acceptance of events near $\cos\theta = -1$ is due to the cut on $p_T(l)$ because, in this case, the leptons are emitted in the direction opposite of the motion of the top quark in the lab frame and therefore have a smaller momentum on average.

The decay products from the lepton-plus-jets channel satisfy many of the triggers that will be implemented at ATLAS such as the b-jet trigger, high p_T muon trigger and the

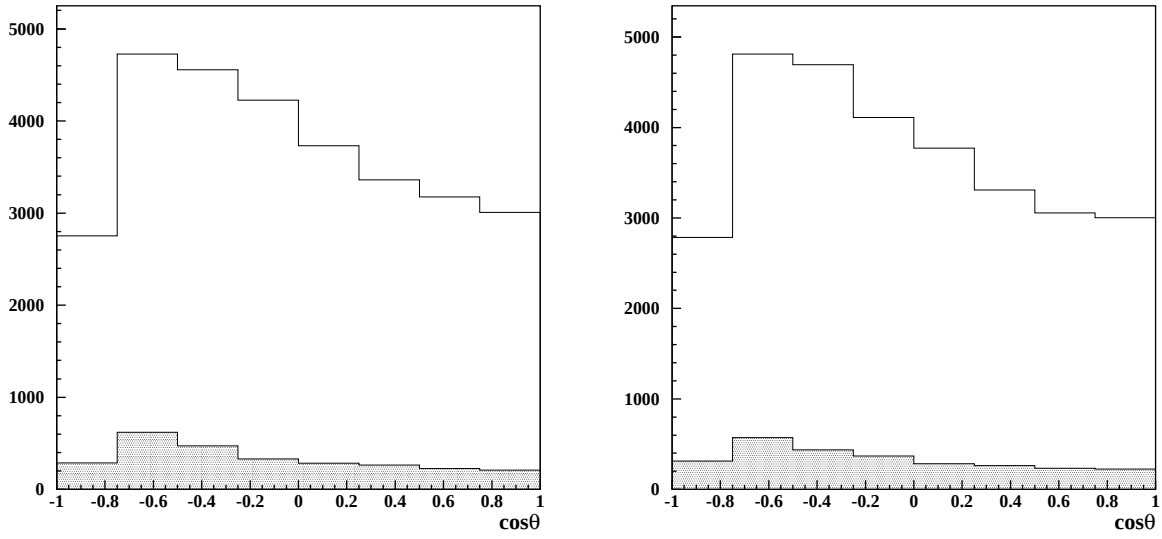

Figure 6.4: The $\cos\theta$ distribution for positively charged leptons (left) and negatively charged leptons (right) with the contribution of the $t\bar{t}$ background (shaded) after event selection cuts are applied. The distributions above correspond to data with $\Delta N_{LR} = 0$ and an integrated luminosity of 30 fb^{-1}.

e/γ trigger. The data that will constitute the top physics sample will be a combination of events that satisfy one or more of these triggers. It has not been decided which physics triggers will have priority or will be pre-scaled in the experiment [50]. Hence, there was no trigger criteria applied in the event selection for this study. The trigger efficiencies for objects in the p_T range that are used for selecting lepton-plus-jets are very good [38]. A conservative estimate would be an overall efficiency of 90% which can be applied to the integrated luminosities found in this study. For example, a result for 30 fb^{-1} might be closer to the same result for 33 fb^{-1} if true trigger efficiencies were considered. This assumption should not effect the results of this study in any significant way.

Channel		Fraction (%)
tau plus jets	$(\tau\nu)(jj)$	86.7
tau and muon	$(\tau\nu)(\mu\nu)$	4.2
tau and electron	$(\tau\nu)(e\nu)$	3.9
all jets	$(jj)(jj)$	2.3
muon and electron	$(\mu\nu)(e\nu)$	0.9
ditau	$(\tau\nu)(\tau\nu)$	0.8
dielectron	$(e\nu)(e\nu)$	0.6
dimuon	$(\mu\nu)(\mu\nu)$	0.6
total $t\bar{t}$ BG		100

Table 6.2: The background from $t\bar{t}$ events in the lepton-plus-jets channel. The right-hand column indicates the fraction of background events remaining after the cuts described in Section 6.1 are applied.

6.2 Backgrounds

The backgrounds in the lepton-plus-jets channel can be separated into two categories: those arising from non-$t\bar{t}$ pair production such as W+jets events, and those backgrounds associated with $t\bar{t}$ events.

6.2.1 Backgrounds from $t\bar{t}$ Events

This background is dominated by events where one W decays into a τ lepton and a neutrino, and the other W decays hadronically. The τ can then decay leptonically which produces a muon or an electron and additional missing energy. Table 6.2 shows the contribution of all backgrounds from $t\bar{t}$ events. Over 90% of this background involves a $W \to \tau\nu$ decay. The contribution of this background varies with $\cos\theta$ in the range from 7 to 13% after the application of event selection cuts and is shown in Figure 6.4.

Non-$t\bar{t}$ BG	Fraction (%)
W+jets	86.3%
Z+jets	12.1%
WW	0.5%
WZ	0.4%
ZZ	0.7%

Table 6.3: Fraction of events that are background from non-$t\bar{t}$ events [38]. The largest contribution to the non-$t\bar{t}$ background is from W+jets events.

6.2.2 Non-$t\bar{t}$ Backgrounds

The non-$t\bar{t}$ backgrounds are reduced to the level of S/B $\sim$ 30 by the kinematic event selection cuts [38]. Table 6.3 shows the relative contribution of the backgrounds from non-$t\bar{t}$ events. The main contribution to this background is from W+jets events.

The non-$t\bar{t}$ background will contain more events with positively charged leptons because of the pp initial state. This has implications for the measurement of ΔN_{LR}, and are discussed in Section 6.5.1.

6.3 Resolution of the $\cos\theta$ Measurement

The value of $\cos\theta$ is measured on an event-by-event basis. The quality of the measurement is important since the distribution in $\cos\theta$ is used to determine ΔN_{LR}. One critical factor is the resolution of the $\cos\theta$ measurement. Figure 6.5 shows how the resolution varies over several intervals of $\cos\theta$(MC truth). It can be seen the resolution gets worse as the value of $\cos\theta$ increases.

The largest contribution to the poor $\cos\theta$ resolution is the identification of E_T^{miss} with $p_T(\nu)$ in the reconstruction of the event. This was determined by comparing the reconstructed and MC truth values for $\cos\theta$ a number of times, each time replacing one

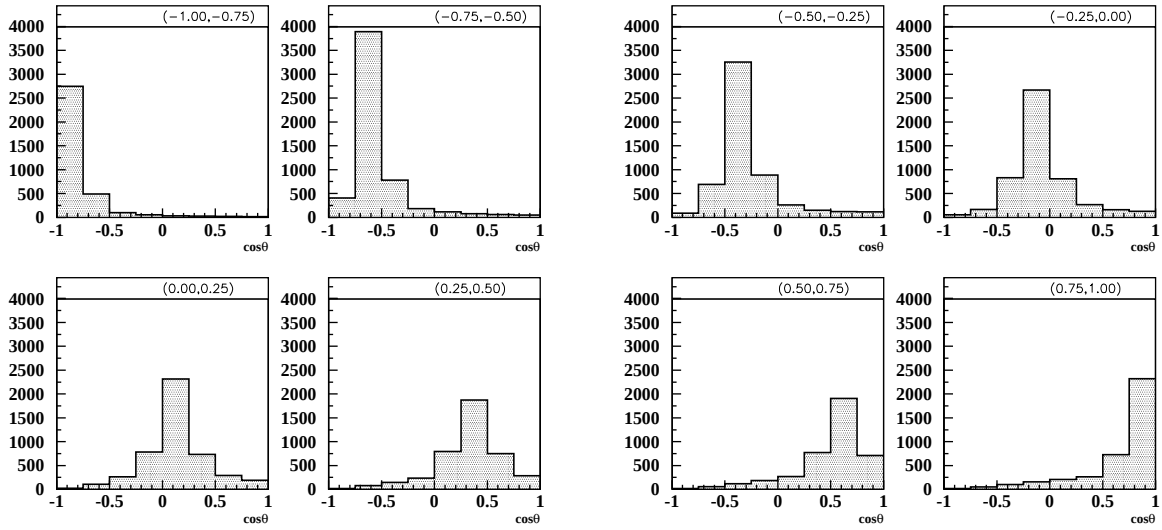

Figure 6.5: The resolution in measured values of $\cos\theta$ as a function of $\cos\theta$. Each distribution represents one interval of the MC truth values as shown above each plot.

factor with the corresponding MC truth value. For example, in one case the reconstructed lepton was replaced with the MC truth lepton. In another case the b-jet momenta were replaced by the b-quark momenta, and so on. There was negligible improvement in all cases except when E_T^{miss} was replaced by the missing transverse energy of the neutrino. Unfortunately, there is no strategy to decrease $|E_T^{miss} - p_T(\nu)|$ and therefore no way to improve the resolution in $\cos\theta$.

Since the resolution in $\cos\theta$ distorts the true distribution, it is necessary to make a correction. The simulation provides the true value of $\cos\theta$ for each lepton-plus-jets event, so a correction can be made using a deconvolution. However, the deconvolution will most effective when the purity in each bin is large. The purity is defined as the number of Monte Carlo truth events remaining in a bin divided by the total number of events in that bin. The purity can be increased by decreasing the number of bins in the $\cos\theta$ distribution. Figure 6.6 shows the purity in each bin for different choices for the number of bins used. The purity becomes 80% when two bins are used which is the minimum

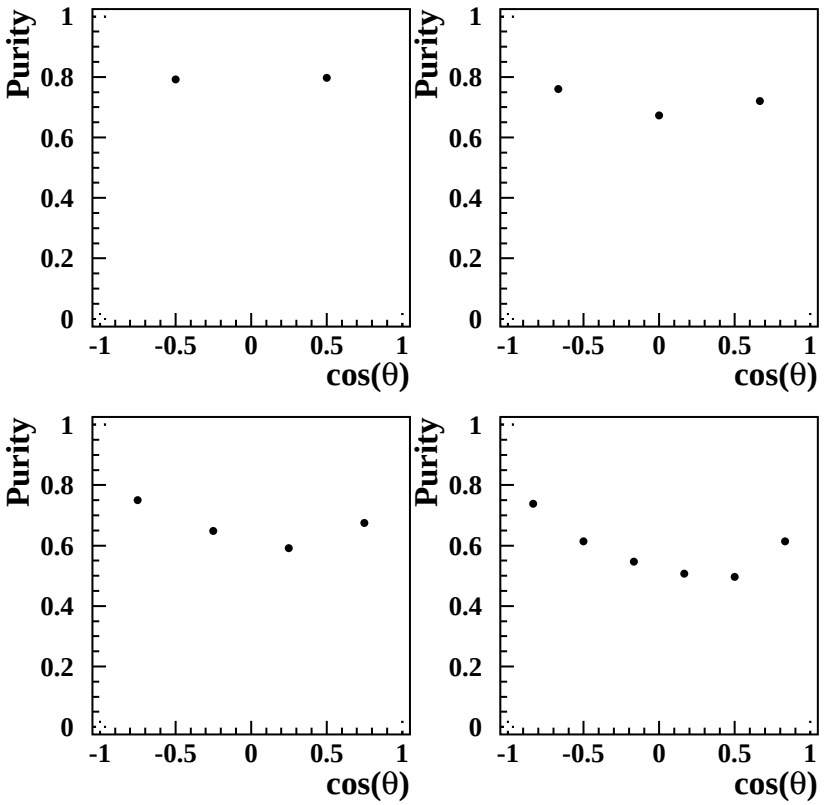

Figure 6.6: The purity in each bin for different numbers of bins in $\cos\theta$. The cases for 2, 3, 4, and 6 bins are shown.

number needed to make a measurement of ΔN_{LR}.

6.4 Direct Measurement of ΔN_{LR}

The measurement of ΔN_{LR} in an ideal experiment has been discussed in Section 2.4.2. However, there are a number of issues that arise when the measurement is made in a real experiment such as the ATLAS detector. The main problems are background events and a poor resolution in $\cos\theta$.

The section describes the strategy for correcting the measured distributions of $\cos\theta$ to arrive at a distribution that is the best estimate of the true distribution. The first

step is to subtract the background due to non-lepton-plus-jets $t\bar{t}$ events. The resulting distribution is then corrected for the distortion resulting from the poor resolution in $\cos\theta$. The third step corrects for the detector acceptance. To show how the distributions evolve as each correction is applied, the case of $\Delta N_{LR} = 6.6\%$ will be used for illustration.

The distributions for positive and negative leptons are treated separately until the very end where the difference is taken to obtain an asymmetry. Since it rarely happens that an equal number of events with opposite charge are obtained after event selection, the events are weighted such that the area under both histograms is the same before any corrections are applied.

6.4.1 Subtraction of Non-Lepton-Plus-Jets $t\bar{t}$ Background

The first step is to remove the background contribution due to $t\bar{t}$ events from the measured distributions of $\cos\theta$. This is accomplished by a Monte Carlo background subtraction whereby the fraction of background events in each bin is determined using the fast simulation. Only the background from $t\bar{t}$ events is considered here. The contribution from non-$t\bar{t}$ background events is $\sim$3% level and is treated as a systematic uncertainty in Section 6.5.1.

The fraction of background events due to $t\bar{t}$ production is given in Table 6.4. The results are based on 30 fb^{-1} of integrated luminosity. The errors are included here, but in principle can be made much smaller as they depend on the number of events simulated. The effect of the background subtraction step is shown in Figure 6.7.

6.4.2 Deconvolution in $\cos\theta$

After the background subtraction, the resolution effects can be corrected by performing a deconvolution on the background-subtracted $\cos\theta$ distribution to yield a "true" distribution [62, 63]. That is, one that results from the effect of the cuts and the acceptance of the detector only.

Bin	BG Fraction (%)
-1 $< \cos\theta <$ 0	10.1 ± 0.2
0 $< \cos\theta <$ 1	6.9 ± 0.2

Table 6.4: Fraction of events that are background from $t\bar{t}$ events for each bin in the measured $\cos\theta$ distribution after event selection. The background fraction is defined as $N_{BG}/(N_{SIG} + N_{BG})$.

A deconvolution can be described as follows: Let y_i be the number of counts in the ith bin of the "true" distribution. The observed distribution, x_i, is the result of a response function, R, where the R_{ij} is the probability given that the true value falls in bin j is actually observed in bin i. The observed distribution is given by

$$x_i = \sum_{j=1}^{N_{bins}} R_{ij} y_j, \tag{6.5}$$

where N_{bins} is the number of bins in the distribution.

The elements of R_{ij} were obtained using the data in Figure 6.5 and using $N_{bins} = 2$. The choice of $N_{bins} = 2$ is to reduce the size of the off-diagonal elements of the response function as much as possible while still retaining the ability to measure ΔN_{LR}.

The inverse of R is found so that the "true" $\cos\theta$ distribution can be obtained from the measured $\cos\theta$ distribution. The maximum likelihood estimators, $\hat{y}_i$, for each bin are given by

$$\hat{y}_i = \sum_{j=1}^{N_{bins}} R_{ij}^{-1} \hat{x}_j, \tag{6.6}$$

where $\hat{x}_j$ is the actual measured distribution. The data used to find R_{ij} was independent of the the data to which the correction was applied. The response function that was used is given as

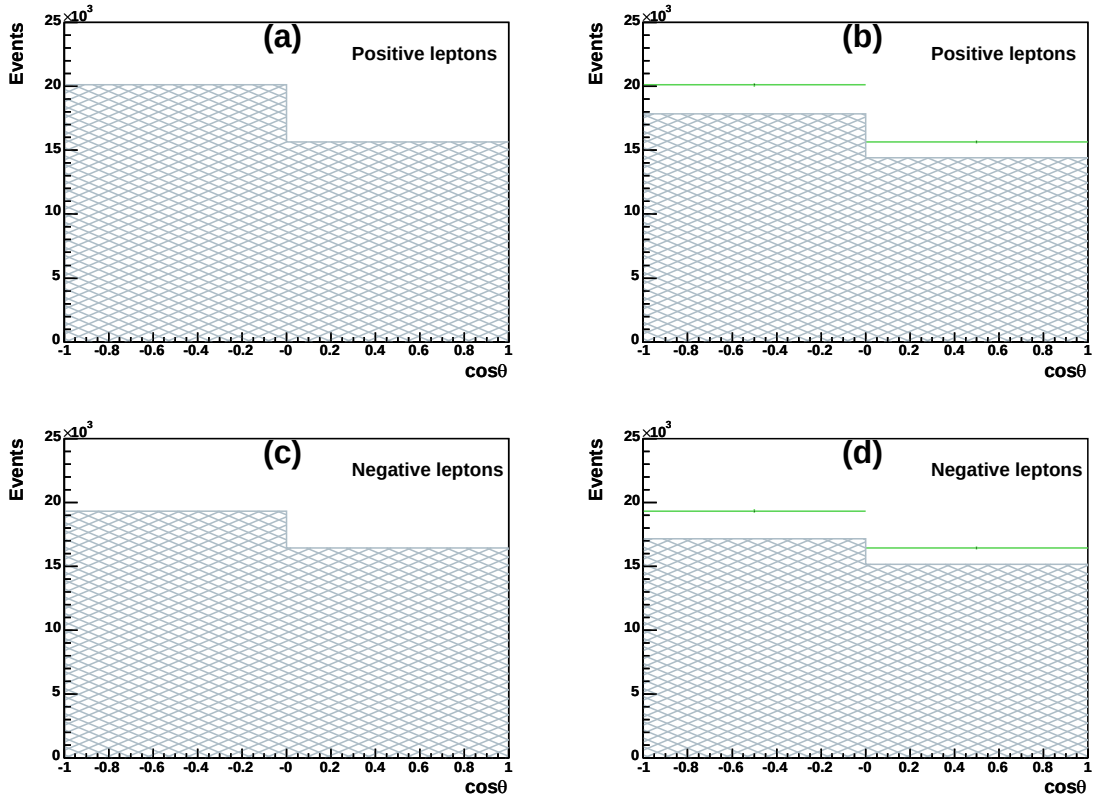

Figure 6.7: The $\cos\theta$ distribution before (a and c) and after (b and d) the $t\bar{t}$ background is subtracted for a data set with $\Delta N_{LR} = 6.6\%$ and an integrated luminosity of 30 fb^{-1}. Figures (a) and (b) are for the positive leptons; figures (c) and (d) are for the negative leptons. The lines on the plots on the right hand side show the number of events before the correction was applied.

$$R = \begin{pmatrix} 0.878 & 0.122 \\ 0.143 & 0.857 \end{pmatrix}. \tag{6.7}$$

The effect of the deconvolution is shown in Figure 6.8.

6.4.3 Acceptance Correction

Scaling the $\cos\theta$ distribution to account for the acceptance of the detector and the effect of the cuts is the last step. This correction yields the distributions one would obtain if

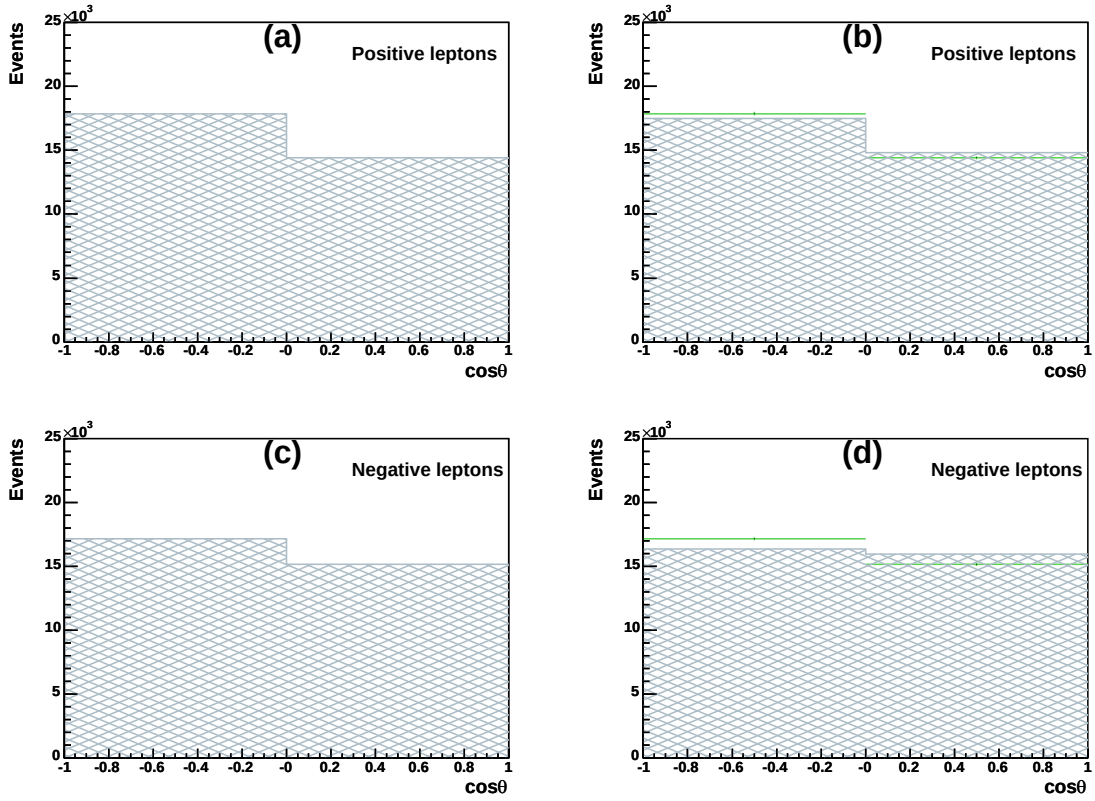

Figure 6.8: The $\cos\theta$ distribution (a and c) before and (b and d) after the deconvolution step for a data set with $\Delta N_{LR} = 6.6\%$ and an integrated luminosity of 30 fb^{-1}. Figures (a) and (b) are for the positive leptons; figures (c) and (d) are for the negative leptons. The lines on the plots on the right hand side show the number of events before the correction was applied.

an ideal detector was used. There is a dependence due to the acceptance of the detector on the $\cos\theta$ distribution; that is, the cuts and acceptance are a function of $\cos\theta$ as was seen in Figure 6.4. The scaling factors for each bin in $\cos\theta$ are listed in Table 6.5. Since the scaling factor is derived from a finite number of simulated events, it has an error associated with it. The asymmetry in the $\cos\theta$ distribution, before and after the acceptance correction, is shown in Figure 6.9.

Once the background subtraction, deconvolution, and acceptance correction have been applied to a set of events, the ΔN_{LR} measurement is made. The data set illustrating the corrections was created with $\Delta N_{LR} = 6.6\%$. Using Eqn. 2.12, a value of $\Delta N_{LR} =$

Bin	Scaling Factor
$-1 < \cos\theta < 0$	104.0 ± 0.6
$0 < \cos\theta < 1$	114.9 ± 0.7

Table 6.5: The scaling factors to correct for the acceptance of the detector.

$7.1 \pm 1.5\%$ is obtained from asymmetry shown in Figure 6.9(b).

The uncertainty in ΔN_{LR} provides a way to quantify the sensitivity we have in the measurement of ΔN_{LR}. The uncertainty of the measurement above corresponds to $\pm 1\sigma$. The confidence level of a measurement of ΔN_{LR} as a function of integrated luminosity is shown in Figure 6.15. The dependence of the uncertainty will go as $1/\sqrt{\int \mathcal{L} dt}$. As the integrated luminosity increases to very large values, the uncertainty will asymptotically approach the systematic uncertainty which is discussed next.

6.5 Systematic Effects

Systematic effects for a direct measurement of ΔN_{LR} in the lepton-plus-jets channel will come from a number of sources and are considered below. It is important to understand how large these effects can be in order to know when the measurement of ΔN_{LR} becomes limited by systematics rather than statistics. Since the ΔN_{LR} measurement is made by taking the asymmetry of $\cos\theta$ distributions from oppositely charged leptons, systematic effects that do not depend on the charge of the lepton cancel out in the asymmetry.

6.5.1 Non-$t\bar{t}$ Backgrounds

The largest number of background events come from $t\bar{t}$ production itself where the leptonically decaying W yields a τ lepton. This type of background was described in Section 6.2 and Section 6.4.1. Other types of background from non-$t\bar{t}$ events will certainly be present after event selection cuts, but their contribution will be quite small at the 3% level [38].

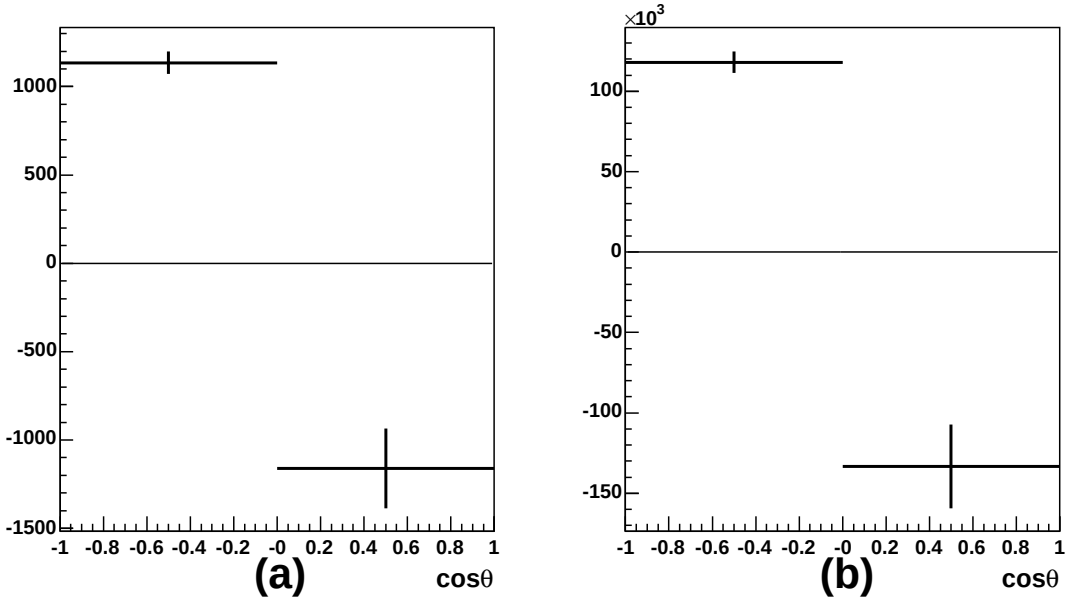

Figure 6.9: The asymmetry of the $\cos\theta$ distribution (a) before and (b) after the acceptance correction has been applied. (a) is obtained from difference of Figures 6.8(b) and (d). The data set was created with a $\Delta N_{LR} = 6.6\%$ and an integrated luminosity of 30 fb^{-1}. The measured value for ΔN_{LR} in this case is 7.1±1.5%.

To simulate the effect of non-$t\bar{t}$ backgrounds, a number of events were added to the $\cos\theta$ distributions after the selection cuts, and before any corrections were made. The total number of background events were divided between the $\cos\theta$ distributions for l^+ and l^-. The fraction of the background that was added to each of the two bins in $\cos\theta$ was also varied. This latter variation was the same for both positive and negative $\cos\theta$ distributions. The variation in the ΔN_{LR} measurement can be seen in Figure 6.10 for the case of 3% total added background.

The initial proton-proton state means that the non-$t\bar{t}$ background will contribute more to the $\cos\theta$ distribution of positively charged leptons. For the W+jets channel, where the W decays leptonically, 58% of the background contains positively charged leptons. This fraction varies only 1% when different parton distribution functions are used.

The background passing the event selection cuts may also favour one of the two bins

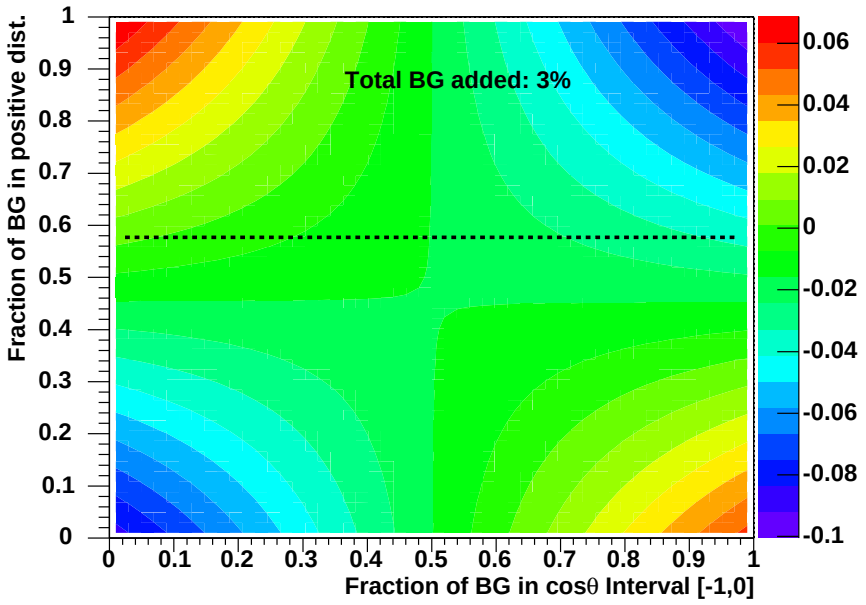

Figure 6.10: The effect on a ΔN_{LR} measurement with the addition of non-$t\bar{t}$ background at a level of 3%. The value ΔN_{LR} is shown as a function of fraction of background added to the $\cos\theta$ distribution of the positively charged leptons, and as a function of the fraction of the added background that was added to the $\cos\theta$ interval [0,1]. The fraction of positively charged leptons in the W+jets and Z+jets backgrounds is 58%. The original dataset had $\Delta N_{LR} = 0$ and an integrated luminosity of 20 fb^{-1}.

in $\cos\theta$ The background also does not have to be evenly distributed between the two bins, but may favour one $\cos\theta$ bin over another. To determine this is difficult because many of the backgrounds have a large cross-section and a small chance of surviving the selection cuts, so it is very difficult, without massive computing resources, to ascertain which bin in $\cos\theta$ is favoured.

6.5.2 Muon Spectrometer Alignment

Misaligned MDT stations in the muon spectrometer can lead to an asymmetry in the p_T measurements between positively and negatively charged muons. Since the reconstruction of the leptonically decaying top depends on the muon information to determine the

top quark rest frame, the $\cos\theta$ measurement is shifted in opposite senses for leptons of opposite charge, and the ΔN_{LR} measurement can be affected. The effect of the misalignment on the first level muon trigger will be negligible because the position resolution on the RPC chambers is large (1 cm).

To investigate how large this effect can be, an estimate was made of the change in momentum a muon would experience if the sagitta measurement of its track was shifted due to a misalignment of the middle MDT stations. A "worst-case" scenario was considered where the middle MDT stations were shifted such that all p_T measurements for μ^+ were increased and all measurements for μ^- were decreased. Assuming a uniform magnetic field in the muon spectrometer, the momentum shift of the muon Δp_T in units of MeV/c is given by

$$\Delta p_T = \frac{(6.66 \times 10^{-9}) p_T^2 \cos^2\theta \Delta d}{e D^2 B} \tag{6.8}$$

where Δd is the shift of the middle MDT station in μm, $B = 0.6$ T is the magnetic field in Tesla, θ is the angle of the track with respect to $\eta = 0$, e is the unit of elementary charge, and $D = 3.0$ m is the distance between MDT stations. The p_T of any electrons was left unchanged since they do not reach the muon spectrometer.

Figure 6.11 shows how a measurement of ΔN_{LR} changes with global shifts of the middle MDT stations in the range of [-150 μm, $+150$ μm]. The result is a linear dependence on the shift of the stations with a slope of -1.5×10^{-4} μm^{-1}.

The range chosen for the MDT misalignment is much larger the magnitude of any possible misalignment. An effect of this magnitude on the muon p_T distribution will show up in other processes that have a much larger cross-section such as $Z \to \mu\mu$. The p_T spectrum for the oppositely charged muons in this well-defined resonance should be identical and will be a good indicator for systematic misalignments in the muon spectrometer. This is especially true for processes that yield straighter, high p_T tracks.

The goal for the maximum allowable error of the sagitta measurement in the muon

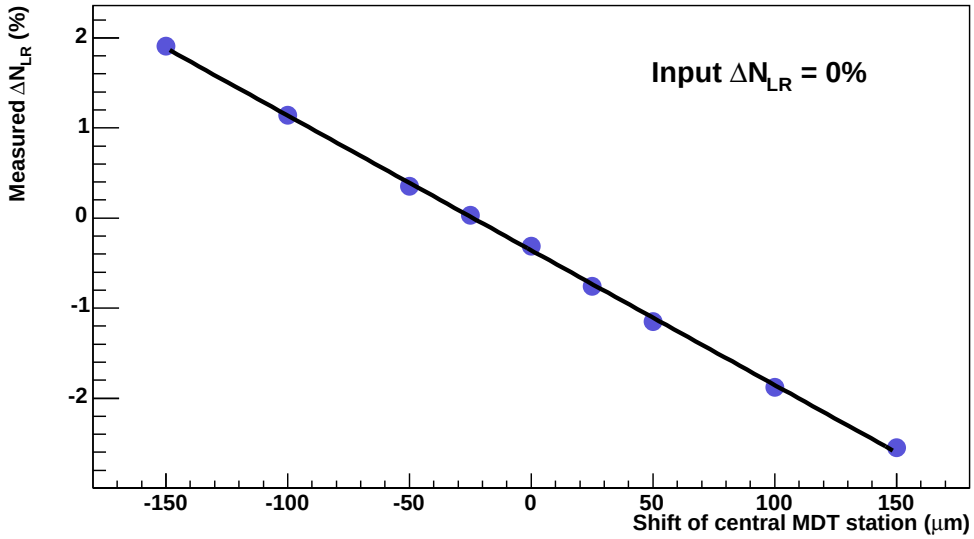

Figure 6.11: Systematic variation in ΔN_{LR} from a global shift of the middle MDT stations in the muon spectrometer. The residuals are much smaller than the statistical error ($\pm 1.78\%$), therefore the error bars have been omitted.

system is 30 μm. The worst-case scenario where all middle MDT stations are shifted uniformly gives a systematic uncertainty of $\pm 0.45\%$ in ΔN_{LR}. A scenario where 224 possible station misalignments are distributed normally with a standard deviation of 30 μm, the uncertainty in the mean becomes ± 2 μm. The systematic error in ΔN_{LR} is then $\pm 0.03\%$. The MDTs are attached to a common structure, so misalignments will not be totally independent. The systematic error will lie somewhere between these two extremes.

6.5.3 Detector Acceptance/Trigger Effects

The ATLAS detector has many areas not instrumented due to the presence of structural elements, data cables, and the various services required, such as the cryogenics. The most problematic region is the transition between the barrel and the endcap at $|\eta| \approx 1.5$. While efforts have been made to minimize the impact of this, they remain as unavoidable

obstacles. The degradation in resolution in these areas is parameterized in the fast simulation, but cracks and holes are not.

Cracks and holes may just be the right shape to allow greater number of positive leptons to be detected than negative leptons, since the Lorentz force on oppositely charged particles in a magnetic field will make them curve in different directions. Fortunately, this is not a concern at all since this can not discriminate between leptons coming from a $t_R\bar{t}_R$ or a $t_L\bar{t}_L$ pair. Therefore, there will be no effect on a measurement due to the detector acceptance. The same argument applies to the muon and EM triggers. That is, a preference in lepton charge will not yield a preference for events with a particular helicity and therefore can not introduce a false signal for ΔN_{LR}.

The lepton triggers are designed to give an accept at a well defined momentum regardless of the particle's charge. A non-zero value for ΔN_{LR} means that the momentum spectrum between l^+ and l^- will not be the same. For $\Delta N_{LR} > 0$, for example, the l^+ will have a larger average momentum as illustrated in Figure 2.9. Events that pass the event selection cuts will have a higher fraction of positively charged leptons. The fraction will increase with increasing ΔN_{LR} and is illustrated in Figure 6.12. There will be a preference for $t_L\bar{t}_L$ pairs over $t_R\bar{t}_R$ pairs, so the trigger may significantly enhance the measured value of ΔN_{LR}. The degree to which this will happen will depend on the amount of CP violation since the l^+-l^- momentum asymmetry increases with ΔN_{LR}.

For small ΔN_{LR}, the effect will be small since the p_T distributions for l^+ and l^- will be virtually identical. For larger values, the effect is more important when the difference between the number of selected events with l^+ and l^- is larger than expected from statistics alone. The size of this effect was attempted to be seen with datasets of 20 fb^{-1} and is shown in Figure 6.13. For values of ΔN_{LR} ranging between 0 and 40%, there is a clear indication that events with a positively charged lepton are favoured. However, the measured value of ΔN_{LR} does not significantly increase even at the 40% level.

It is clear from Figure 6.13 that for a limited amount of data such as one obtains for

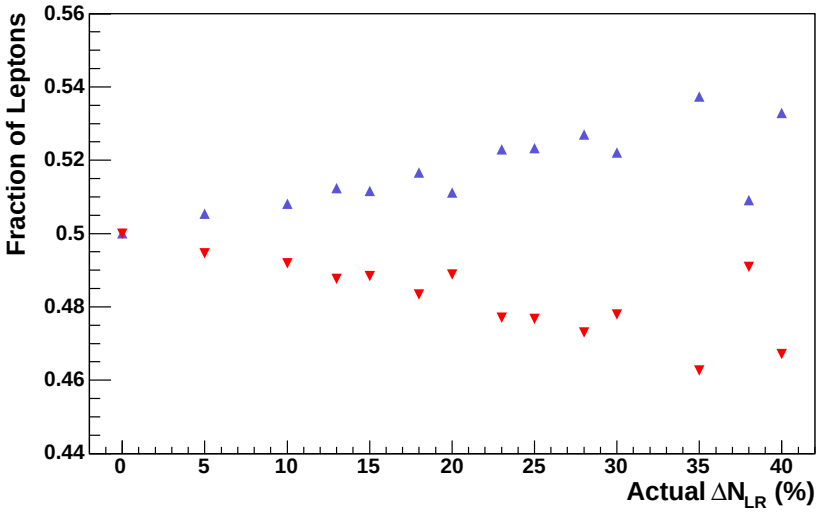

Figure 6.12: The effect on the fraction of events with positively and negatively charged leptons passing cuts for increasing values of ΔN_{LR}. As ΔN_{LR} increases, the number of positive (negative) leptons passing all selection criteria increases (decreases). Negative and positive leptons are indicated by inverted and upright triangles, respectively. All datasets used had an integrated luminosity of 20 fb^{-1}.

20 fb^{-1}, there is no significant effect on the measured ΔN_{LR} value beyond the statistical uncertainty. This makes it difficult to ascertain the size of this systematic effect. For small values of ΔN_{LR}, this effect will be small. If a large value of ΔN_{LR} were to be found, this effect could be corrected by using a larger set of Monte Carlo events.

6.5.4 pp Initial State

Protons contain three valence quarks, gluons, and a sea of quark–anti-quark pairs. On average, therefore, the quarks in a proton carry more momentum than the anti-quarks. Through the $q\bar{q} \to t\bar{t}$ process at the partonic level, the top will have more momentum than the anti-top due to QCD corrections. Consequently, a positively charged lepton from a top decay will also have a larger average p_T than the negatively charged lepton. The resulting p_T asymmetry between positively and negatively charged leptons is equivalent

to $\Delta N_{LR} \approx -2 \times 10^{-4}$ [32]. However, the lepton p_T asymmetry is not used to find ΔN_{LR} in the lepton-plus-jets channel. Any systematic effect will result from the apparent value of ΔN_{LR} changing a small amount, leading to a change in the number of positive versus negative charged leptons passing the trigger. As discussed in Section 6.5.3, for small ΔN_{LR}, the effect will be small. Any systematic change in ΔN_{LR} on the order 10^{-4} will be negligible.

6.5.5 Charge Misidentification

Particles with high transverse momentum have very straight tracks which makes it difficult to determine the sign of their charge. The inner detector is designed to limit charge misidentification to <2% and <5% for 1 TeV/c muons and electrons, respectively. At 500 GeV/c, these numbers fall to ∼0.2% for muons and ∼1.4% for electrons [36]. Charge misidentification is not done in the fast simulation, but the effect of should be considered in the context of the ΔN_{LR} measurement.

The p_T distribution for leptons coming from $t\bar{t}$ events has a maximum at approximately 30 GeV/c and an average of 50 GeV/c. There are very few leptons with $p_T > 250$ GeV/c (see Figure 6.1). The curvature of tracks in this momentum range is more pronounced, so the probability for charge misidentification for leptons from $t\bar{t}$ becomes very small. The combined probability of a lepton having a momentum greater than 250 GeV/c and simultaneously measuring the sign of the lepton charge incorrectly means that the effect of charge misidentification on the ΔN_{LR} measurement will be negligible.

One method to determine the amount of charge misidentification in the real data would be to take events with same-sign leptons, calculate the invariant mass of the leptons, and measure the size of a resonance such as $Z \to l^+ l^-$.

6.5.6 Top Mass

The top mass is assumed to be 175 GeV/c^2 in the reconstruction of the $t\bar{t}$ events. This is also the value of m_t with which the events were generated. To first order, the $\cos\theta$ distributions for both lepton charges are affected in a similar way when the mass used for reconstruction is changed. When $\Delta N_{LR} = 0$, the $\cos\theta$ distributions for positively and negatively charged leptons are equal, so the measured value of ΔN_{LR} is not affected. However, when $\Delta N_{LR} \neq 0$, the $\cos\theta$ distributions for the positively and negatively charged leptons are different, so if the top mass used in the reconstruction is not the same as the true top mass, a systematic error in ΔN_{LR} will arise.

To measure the shift in a ΔN_{LR} measurement due to a difference between the top mass used in the reconstruction and the true mass, the selection and reconstruction of the t and $\bar{t}$ events were performed using values of m_t in the range 165–185 GeV/c^2, using the same set of data each time. The measurement was repeated with several sets of data with different values of ΔN_{LR}: two sets of 30 fb^{-1} integrated luminosity with $\Delta N_{LR} = -1.6\%$ and -6.6%, two sets of 10 fb^{-1} integrated luminosity with $\Delta N_{LR} = -3.3\%$ and -9.9%, and one set of 20 fb^{-1} integrated luminosity with $\Delta N_{LR} = 6.6\%$.

Figure 6.14 shows that the measured value of ΔN_{LR} increases as the top mass used to reconstruct the events increases for $\Delta N_{LR} < 0$. For $\Delta N_{LR} > 0$, the measured of ΔN_{LR} decreases as the top mass increases. The mass of the top will be known only to within 1–2 GeV/c^2 as measured by ATLAS [64], but a much larger range in m_t was used to reduce the uncertainty of a fit. A straight line was found to be a good fit to each set of data. The slopes do not increase monotonically with increasing $|\Delta N_{LR}|$ due to statistical fluctuations between datasets. However, the size of the systematic uncertainty is estimated: the slopes for the data with $\Delta N_{LR} < 0$ have a weighted average value of 0.12 (GeV/c^2)$^{-1}$; the slope measurements from the 30 fb^{-1} datasets were given three times the weight. The systematic uncertainty of a ΔN_{LR} measurement can be as large as 0.12–0.24% depending on the precision of the top mass measurement assuming ΔN_{LR}

Systematic	Comment	$\delta(\Delta N_{LR})$ (%)
Muon spectrometer misalignment		0.03
Non $t\bar{t}$ background	S/B ~ 65	~ 1
Lepton trigger		negligible
pp initial state		none
Total		~ 1

Table 6.6: Summary of the systematic uncertainties of the ΔN_{LR} measurement.

is on the order of a few percent.

This systematic can be eliminated if the parameters used for the corrections were determined using the best measured value of ΔN_{LR}. That is, at the end of an iterative procedure where the correction parameters are adjusted each time after determining ΔN_{LR}, stopping when the value of ΔN_{LR} no longer changes.

6.6 Summary of ΔN_{LR} Measurement

A method of measuring ΔN_{LR} using $t\bar{t}$ events has been presented. To summarize, selection cuts are used to obtain a sample of events decaying into the lepton-plus-jets channel, the top and anti-top quarks are reconstructed, and the value of $\cos\theta$ is determined for each event. Distributions of $\cos\theta$ for events with l^+ and l^- are obtained. A number of corrections are made to the distributions to remove the effect of background events, the the resolution in $\cos\theta$, and the acceptance of the detector. The asymmetry of the corrected $\cos\theta$ distributions yields a value for ΔN_{LR}.

A number of systematic effects were considered. Table 6.6 summarizes the size of these systematic uncertainties in decreasing order. The largest contribution to the systematic uncertainty depends on the difference between the true top mass and the mass used in event reconstruction.

The statistical uncertainty as calculated represents one standard deviation. The confidence level that a measured value of ΔN_{LR} will be different from the null hypothesis as a function of integrated luminosity is shown in Figure 6.15. The cross-hatched area shows the contribution of the systematic uncertainty.

6.7 Measurement of ΔN_{LR} as Function of $\sqrt{s}$

In general, ΔN_{LR} is a function of the center of mass energy $\sqrt{s}$ of the $t\bar{t}$ system. How ΔN_{LR} varies with $\sqrt{s}$, and the ability to find this dependence, can help one distinguish which model is responsible if a non-zero CP violating signal is present. The center of mass energy can be found on an event-by-event basis because the $t\bar{t}$ can be fully reconstructed.

In this section, the ability of the ATLAS detector to measure ΔN_{LR} as a function of $\sqrt{s}$ is presented. The general strategy is to separate events into separate bins in $\sqrt{s}$, then measure ΔN_{LR} in each bin. To find a suitable size of bin, the resolution in the measurement of $\sqrt{s}$ is first determined.

6.7.1 Resolution of the Center of Mass Energy

The $t\bar{t}$ state is fully reconstructed in the lepton-plus-jets channel which allows the center of mass energy to be measured. The distribution of center of mass energy for signal events is shown in Figure 6.16 where it can be seen most events are produced just above the threshold of $2m_t$. The resolution of the center of mass energy measurement is found by comparing the reconstructed $\sqrt{s}$ to the MC truth value and varies with $\sqrt{s}$ as shown in Figure 6.17.

To measure ΔN_{LR} as a function of $\sqrt{s}$, events must be separated into bins according to their measured center of mass energy. The bin size chosen should be greater than the resolution at a given value of $\sqrt{s}$ and the resolution decreases with increasing $\sqrt{s}$. If it is desired to have a similar number of events in each bin, the bin size must increase

with $\sqrt{s}$.

As the number of bins increases, the number of events in each bin decreases. Consequently, the statistical uncertainty in each bin increases. Table 6.7 shows one choice of event binning for an integrated luminosity of 30 fb^{-1}. The number in each of the 3 bins in the range 350–700 GeV have approximately the same number as the total number of events that would be found with an integrated luminosity of 8 fb^{-1}. The uncertainty of a measurement of ΔN_{LR} in those bins will therefore be about $\pm 3.0\%$.

Bin #	Range in $\sqrt{s}$ (GeV)	Events for 30 fb^{-1}	Percent of total	$t\bar{t}$ background (%)	
				$\cos\theta < 0$	$\cos\theta > 0$
1	350–450	18468	26.2	10.4	8.3
2	450–550	19912	28.2	10.6	8.2
3	550–700	17180	24.3	11.4	7.4
4	700–950	10777	15.3	12.6	7.3
5	950+	4193	6.0	13.6	6.4

Table 6.7: Example of bin definition in $\sqrt{s}$. The number of events found after cuts and the fraction of $t\bar{t}$ background for each bin are presented.

Once the choice of bins are made, ΔN_{LR} can then be measured in each $\sqrt{s}$ separately. The parameters used to perform the corrections for the background, $\cos\theta$ resolution, and acceptance must be determined separately for each bin because, in general, they vary as a function of center of mass energy.

6.8 Conclusions

A method for making a direct measurement of the CP violating observable ΔN_{LR} in the lepton-plus-jets channel was presented. It is based on determining the difference in angular distribution of the leptons in the decay of right- and left-handed top quarks.

Several systematic effects were investigated. The most important was due to the uncertainty of the distribution of the non-$t\bar{t}$ background in $\cos\theta$. However, the ΔN_{LR} measurement has a much larger statistical error. For an integrated luminosity of 30 fb^{-1} a measurement of ΔN_{LR} which is as large as 2% can be made at the 75% confidence level.

The measurement of ΔN_{LR} as a function of center of mass energy was also discussed. This is an important measurement to make because it allows a way to differentiate between models that predict this type of CP violation. A much larger quantity of data would be required to make accurate measurements in each bin.

There is no reason why ΔN_{LR} has to be uniformly positive or negative in $\sqrt{s}$. For example, if ΔN_{LR} was large and positive for small $\sqrt{s}$ and negative for large $\sqrt{s}$, a measurement of ΔN_{LR} may yield a measurement that is consistent with zero. Measuring ΔN_{LR} as a function of center of mass energy would make the large variation in ΔN_{LR} apparent.

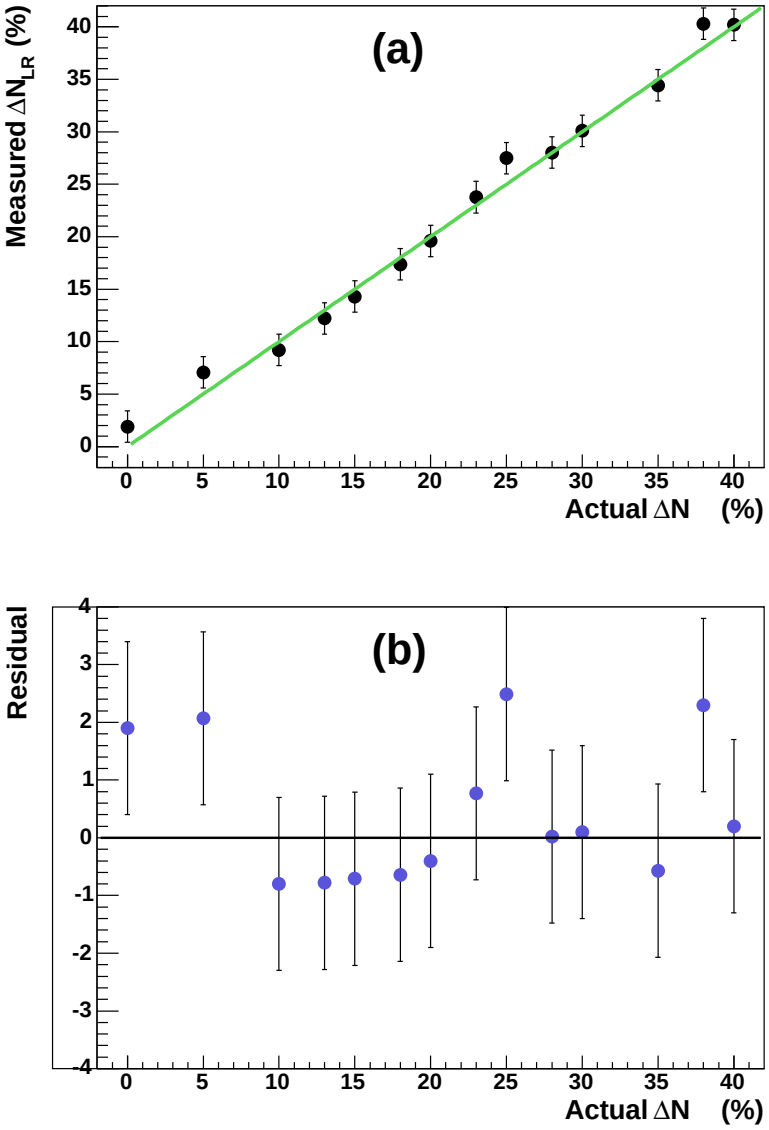

Figure 6.13: The effect of the trigger on a ΔN_{LR} measurement for various values of ΔN_{LR}. In (a), the measured value ΔN_{LR} is shown as a function of ΔN_{LR} of the dataset. The green line is the function $\Delta N_{LR}(\text{measured}) = \Delta N_{LR}(\text{dataset})$. The residuals from (a) are shown in the lower plot (b). All datasets used had an integrated luminosity of 20 fb^{-1}.

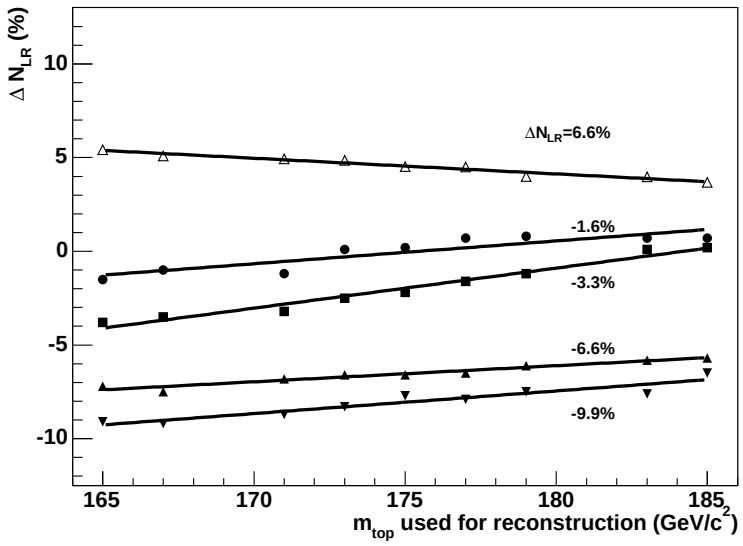

Figure 6.14: Systematic variation in ΔN_{LR} from using different values of the top mass in the reconstruction $t\bar{t}$ pair. The data were simulated using a top mass of 175 GeV/c^2. Starting at the top of the graph, the values of $\Delta N_{LR}(\int \mathcal{L}dt)$ for each dataset are $+0.066(20\ \text{fb}^{-1})$, $-0.016(30\ \text{fb}^{-1})$, $-0.033(10\ \text{fb}^{-1})$, $-0.066(30\ \text{fb}^{-1})$, and $-0.099(10\ \text{fb}^{-1})$. The error bars on the individual ΔN_{LR} measurements are not shown; they are much larger than the residuals of the linear fits.

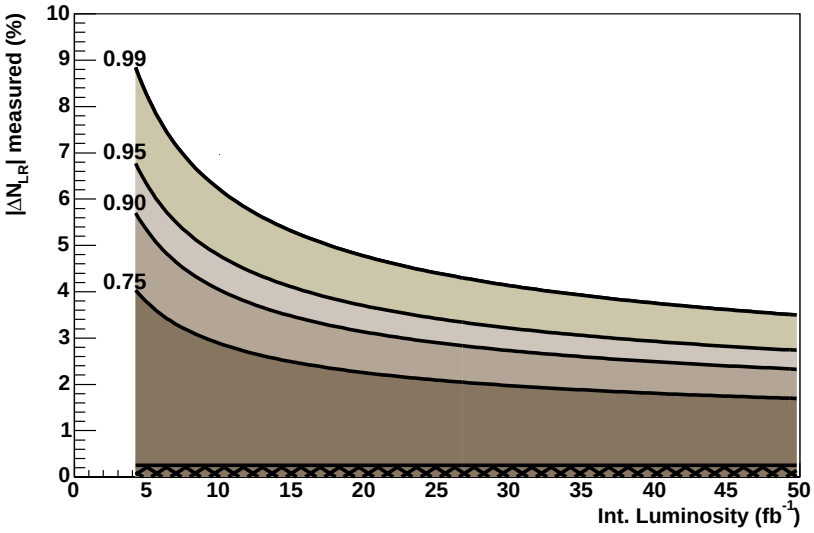

Figure 6.15: The minimum values of ΔN_{LR} that can be measured as a function of integrated luminosity at various confidence levels. For comparison, the total size of the systematic contribution is shown in red at the bottom.

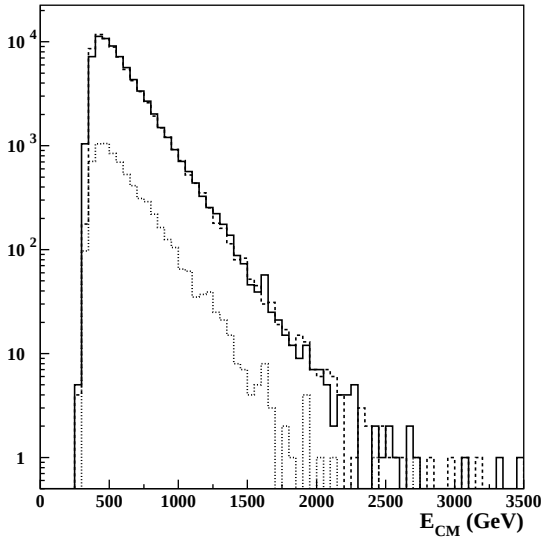

Figure 6.16: Distribution of $\sqrt{s} = E_{cm}$ for $t\bar{t}$ events passing the selection cuts. The solid (dashed) line is the measured (MC truth) distribution. The dotted line is the distribution for $t\bar{t}$ background events.

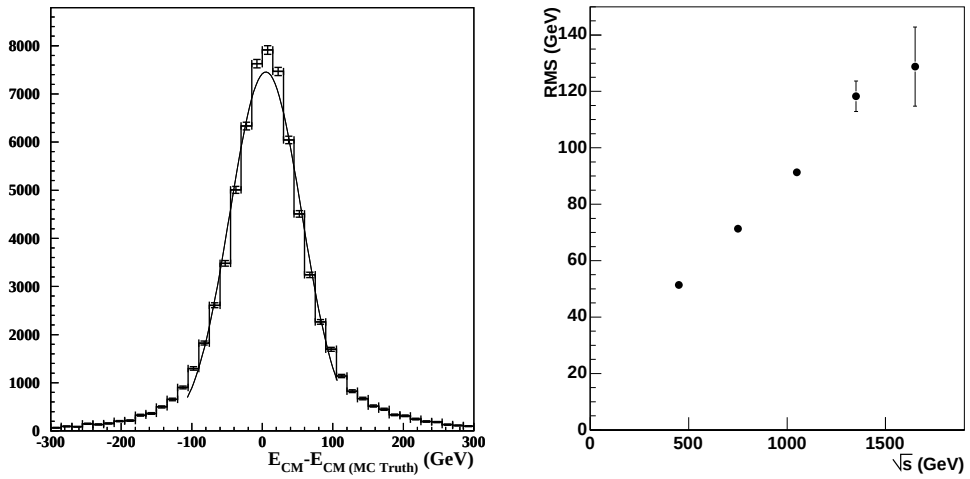

Figure 6.17: The resolution of the center of mass energy for $t\bar{t}$ events passing selection cuts. The left-hand plot shows the resolution for all events passing the selection cuts. The right-hand plot shows the resolution as a function of $\sqrt{s}$.

Chapter 7

Conclusions

Several non-Standard Model theories predict the possibility of CP violation in top pair production. Specifically, they predict that the number of right-handed top pairs ($t_R\bar{t}_R$) produced may differ from the number of left-handed top pairs ($t_L\bar{t}_L$). The CP violating observable is known as $\Delta N_{LR} = (N_{LL} - N_{RR})/N_{TOT}$ where $N_{LL(RR)}$ are the number of $t_R\bar{t}_R(t_L\bar{t}_L)$ pairs produced and N_{TOT} is the total number of $t\bar{t}$ pairs found. At the LHC, there will be a large fraction of $t\bar{t}$ pairs produced with correlated helicities making this the best facility to search for this signal at the present time. This is an important measurement to make even if the result is found to be consistent with zero. A null result will allow limits to be placed on the parameters that produce CP violation in the theories that predict it. A non-zero result will mean that new physics beyond the Standard Model has been found.

The dimuon channel was proposed by Peskin and Schmidt as a way to detect the CP violating signal. This method was investigated in Chapter 5 starting with a study of how the signal-to-background ratio and signal efficiencies change as a function of selection cuts. Several strategies were employed to handle the backgrounds that have a large cross-section and low probability to pass selection cuts.

The maximum CP violating signal as predicted by Peskin and Schmidt in the 2HDM

model is small at the $\Delta N_{LR} = 0.3\%$ level. The asymmetry between $p_T(\mu^+)$ and $p_T(\mu^-)$ was taken for a set of simulated data corresponding to 500 fb^{-1} of integrated luminosity with no selection cuts and no background events added. The resulting asymmetry remained consistent with the null hypothesis. This possible CP violating signal will go undetected at the LHC.

A large drawback to the dilepton channel is that while one may observe an asymmetry in the lepton p_T distributions, it is impossible to determine the value of ΔN_{LR} without first assuming which model is responsible for the CP violation as ΔN_{LR} in general is a function of $\sqrt{s}$.

The best method to measure ΔN_{LR} was via the lepton-plus-jets channel. In this channel, the top and anti-top can be reconstructed, and the angle $\cos\theta$ at which the lepton is emitted can be found. By comparing the $\cos\theta$ distributions for leptons coming from the t and $\bar{t}$, a value for ΔN_{LR} can be obtained.

The center-of-mass energy $\sqrt{s}$ of the $t\bar{t}$ system can be determined in this decay channel. Separating events into bins of $\sqrt{s}$ means that the uncertainty of a ΔN_{LR} measurement in each bin increases, but the dependence of ΔN_{LR} on $\sqrt{s}$ can be measured. Differentiation between CP violating models becomes possible.

The measurement of ΔN_{LR} in the lepton-plus-jets channel will be limited by the statistical uncertainty even after several hundred fb^{-1} of integrated luminosity. The uncertainty in the top mass will be the source of the largest systematic error at a level of $\pm 0.24\%$. The uncertainties due to the jet energy scale, muon spectrometer misalignment, the lepton trigger, and the non-$t\bar{t}$ background are small or negligible in comparison.

A large amount of computing resources was needed to complete this study. This is characteristic of the field of high energy physics where huge quantities of data are obtained and large, complex detectors must be simulated. Fast simulation software was used for this study which used parameterizations based on full simulation results. This reduced significantly the time to simulate events, but does not take into account some

aspects in the real experimental environment like pile-up and the possibility of dead channels in parts of the spectrometer. These factors will degrade the overall performance of the spectrometer, but they will also be included in future simulations that reflect the conditions in the detector once it is operational.

The CP violating signal that is the subject of this thesis is only one of a whole range of interesting physics studies that will be carried out at ATLAS. The center-of-mass energy that will be produced at the LHC has never been achieved at any accelerator. It will be interesting to see if CP violation really happens in top pair production and if any other signatures of new physics are detected.

Appendix A

Contribution to ATLAS

The following is a list of contributions made to the ATLAS collaboration:

- Performed shifts for the assembly of the forward calorimeter component, FCAL2, at the University of Toronto.
- Participated in the ATLAS Data Challenge 1 [65] on the behalf of the University of Toronto. DC1 was an exercise to test computing resources on a large scale.
- Presented a talk on top quark physics on behalf of the ATLAS collaboration at the APS-DPF April Meeting 2003 in Philadelphia.
- Presented a talk on top quark physics on behalf of the ATLAS collaboration at the BEACH 2004 Conference in Chicago [66].

Bibliography

[1] E. Rutherford. The Scattering of α and β Particles by Matter and the Structure of the Atom. *Philosophical Magazine, Series 6*, 21:669–688, 1911.

[2] J.J. Thomson. Cathode Rays. *Philosophical Magazine*, 44:293, 1897.

[3] D. J. Gross and Frank Wilczek. Ultraviolet behavior of non-abelian gauge theories. *Phys. Rev. Lett.*, 30:1343–1346, 1973.

[4] H. David Politzer. Reliable perturbative results for strong interactions? *Phys. Rev. Lett.*, 30:1346–1349, 1973.

[5] S. L. Glashow. Partial symmetries of weak interactions. *Nucl. Phys.*, 22:579–588, 1961.

[6] Abdus Salam and J. C. Ward. Electromagnetic and weak interactions. *Phys. Lett.*, 13:168–171, 1964.

[7] Steven Weinberg. A model of leptons. *Phys. Rev. Lett.*, 19:1264–1266, 1967.

[8] Peter W. Higgs. Broken symmetries, massless particles and gauge fields. *Phys. Lett.*, 12:132–133, 1964.

[9] C. S. Wu, E. Ambler, R. W. Hayward, D. D. Hoppes, and R. P. Hudson. Experimental test of parity conservation in beta decay. *Phys. Rev.*, 105:1413–1414, 1957.

[10] J. H. Christenson, J. W. Cronin, V. L. Fitch, and R. Turlay. Evidence for the 2 π decay of the K(2)0 meson. *Phys. Rev. Lett.*, 13:138–140, 1964.

[11] K. Abe et al. Observation of large CP violation in the neutral B meson system. *Phys. Rev. Lett.*, 87:091802, 2001.

[12] B. Aubert et al. Observation of CP violation in the B^0 meson system. *Phys. Rev. Lett.*, 87:091801, 2001.

[13] N. Cabibbo. Unitary symmetry and leptonic decays. *Phys. Rev. Lett.*, 10:531–532, 1963.

[14] Makoto Kobayashi and Toshihide Maskawa. CP violation in the renormalizable theory of weak interaction. *Prog. Theor. Phys.*, 49:652–657, 1973.

[15] R. D. Peccei. The Strong CP Problem. In C. Jarlskog, editor, *CP Violation*, pages 503–551. World Scientific, 1989.

[16] P. G. Harris et al. New experimental limit on the electric dipole moment of the neutron. *Phys. Rev. Lett.*, 82:904–907, 1999.

[17] Maxim Pospelov and Adam Ritz. Theta induced electric dipole moment of the neutron via QCD sum rules. *Phys. Rev. Lett.*, 83:2526–2529, 1999.

[18] R. D. Peccei and Helen R. Quinn. CP conservation in the presence of instantons. *Phys. Rev. Lett.*, 38:1440–1443, 1977.

[19] K. Zioutas et al. First results from the cern axion solar telescope (CAST). *Phys. Rev. Lett.*, 94:121301, 2005.

[20] The Large Hadron Collider: Conceptual design. CERN-AC-95-05-LHC.

[21] (Ed.) Brüning, O. et al. LHC Design Report. Vol. I: The LHC main ring. CERN-2004-003-V-1.

[22] (Ed.) Brüning, O. et al. LHC Design Report. 2. The LHC infrastructure and general services. CERN-2004-003-V-2.

[23] (Ed.) Benedikt, M., (Ed.) Collier, P., (Ed.) Mertens, V., (Ed.) Poole, J., and (Ed.) Schindl, K. LHC Design Report. 3. the LHC injector chain. CERN-2004-003-V-3.

[24] F. Abe et al. Observation of top quark production in anti-p p collisions. *Phys. Rev. Lett.*, 74:2626–2631, 1995.

[25] S. Abachi et al. Observation of the top quark. *Phys. Rev. Lett.*, 74:2632–2637, 1995.

[26] Erik Brubaker (*for the CDF collaboration*). Top quark mass measurements at CDF. 2006. To appear in the proceedings of 41st Rencontres de Moriond on Electroweak Interactions and Unified Theories, La Thuile, Aosta Valley, Italy, 11-18 Mar 2006. (hep-ex/0605092, FERMILAB-CONF-06-124-E).

[27] Roberto Bonciani, Stefano Catani, Michelangelo L. Mangano, and Paolo Nason. NLL resummation of the heavy-quark hadroproduction cross- section. *Nucl. Phys.*, B529:424–450, 1998.

[28] T. Stelzer and S. Willenbrock. Spin correlation in top-quark production at hadron colliders. *Phys. Lett. B*, 374:169–172, 1996. (hep-ph/9512292).

[29] Gregory Mahlon and Stephen J. Parke. Angular correlations in top quark pair production and decay at hadron colliders. *Phys. Rev.*, D53:4886–4896, 1996.

[30] K. G. Chetyrkin, R. Harlander, T. Seidensticker, and M. Steinhauser. Second order QCD corrections to $\Gamma(t \to wb)$. *Phys. Rev.*, D60:114015, 1999.

[31] Ikaros I. Y. Bigi, Yuri L. Dokshitzer, Valery A. Khoze, Johann H. Kuhn, and Peter M. Zerwas. Production and decay properties of ultraheavy quarks. *Phys. Lett.*, B181:157, 1986.

[32] M. Peskin and C. Schmidt. Probe of CP violation in top quark pair production at hadron supercolliders. *Phys. Rev. Lett.*, 69(3):410–413, 1992. (SLAC-PUB-5788).

[33] S. Weinberg. Unitary constraints on CP nonconversation in higgs-boson exchange. *Phys. Rev. D*, 42(3):860–866, 1990.

[34] C. Schmidt. A top quark CP-violating asymmetry in supersymmetric models. *Phys. Lett. B*, 293:111–116, 1992. (SLAC-PUB-5878).

[35] M. Beccaria, S. Bentvelsen, M. Cobal, F. M. Renard, and C. Verzegnassi. Special supersymmetric features of large invariant mass unpolarized and polarized top antitop production at LHC. *Phys. Rev.*, D71:073003, 2005.

[36] ATLAS Inner Detector TDR, 1997. CERN/LHCC/97–16, CERN/LHCC/97–17.

[37] E. Ros. ATLAS Inner Detector. *Nucl. Phys. Proc. Suppl.*, 120:235–238, 2003.

[38] ATLAS Detector and Physics Performance TDR, 1999. CERN/LHCC/99–15.

[39] J.D. Jackson. *Classical Electrodynamics, 2nd Edition.* John Wiley & Sons, 1975.

[40] I. Gavrilenko. Description of Global Pattern Recognition Program (XKalman), 1997. ATLAS Note (ATL-INDET-97-165).

[41] R. Clifft and A. Poppleton. IPATREC: Inner detector pattern-recognition and track-fitting, 1994. ATLAS Note (ATL-SOFT-94-009).

[42] ATLAS Liquid Argon Calorimeter TDR, 1996. CERN/LHCC/96–41.

[43] ATLAS Tile Calorimeter TDR, 1996. CERN/LHCC/96–42.

[44] M. Sapinski. Expected performance of ATLAS for measurements of jets, b- jets, tau-jets, and E_T(miss). *Eur. Phys. J. direct*, C4S1:08, 2002.

[45] S. Binet. Light jet energy scale *in situ* calibration using a resonance decay in the $t\bar{t}$ channel with ATLAS, 2005. ATLAS Internal Note (ATL-COM-SOFT-2005-001).

[46] ATLAS Muon Spectrometer TDR, 1997. CERN/LHCC/97–22.

[47] G. Kowarik, M. Marchesotti, S. Schuh, R. Da Silva, R. Voss, and V. Zhuravlov. Study of Long-Term Geometry Stability of ATLAS Muon Monitored Drift Tube Chambers, 2005. ATLAS Internal Note (ATL-COM-MUON-2006-001).

[48] W. Blum, H. Kroha, and P. Widmann. Transparent silicon strip sensors for the optical alignment of particle detector systems. *Nucl. Instrum. Meth.*, A377:404–408, 1996.

[49] Level 1 Trigger TDR LHCC 98-14, High-Level Trigger, Data Acquisition and Controls TDR (CERN/LHCC/2003-022).

[50] Johannes Haller and Stefan Tapprogge. Trigger operation in physics running, 2005. ATLAS Internal Note (ATL-DAQ-INT-2005-001).

[51] N. Bosman et al. B-physics performance with Initial and Complete Inner Detector Layouts in Data Challenge 1, 2005. ATLAS Note (ATL-PHYS-2005-002).

[52] J. F. LaPorte, A. Ouraou, et al. Impact of the initial layout on the ATLAS muon spectrometer performance, 2005. ATLAS Note (ATL-COM-MUON-2005-009), ATL-MUON-PUB-2005-001.

[53] T. Sjöstrand, P. Edèn, C. Friberg, L. Lönnblad, G. Miu, S. Mrenna, and E. Norbin. High-energy physics event generation with PYTHIA 6.1. *Computer Physics Commun.*, 135:238, 2001.

[54] E. Richter-Was. ATLFAST 2.0: A fast simulation package for ATLAS, 1998. ATLAS Internal Note (ATL-PHYS-98-131).

[55] S. Agostinelli et al. GEANT4: A simulation toolkit. *Nucl. Instrum. Meth.*, A506:250–303, 2003.

[56] Gerald C. Blazey et al. Run II jet physics. pages 47–77, 2000. *Batavia 1999, QCD and weak boson physics in RunII.*

[57] H. L. Lai et al. Global QCD analysis of parton structure of the nucleon: CTEQ5 parton distributions. *Eur. Phys. J.*, C12:375–392, 2000.

[58] J. von Neumann. Various Techniques Used in Connection with Random Digits. *U.S. National Bureau of Standards Applied Mathematics Series*, 12:36–38, 1951.

[59] Gregory Mahlon. Spin polarization in single top events. 1998.

[60] Andrzej Czarnecki, Marek Jezabek, and Johann H. Kuhn. Lepton spectra from decays of polarized top quarks. *Nucl. Phys.*, B351:70–80, 1991.

[61] A. Lagatta, L. La Rotonda, and M. Cobol. Top mass evaluation in the $t\bar{t}$ dilepton decay channel, 1999. ATLAS Internal Note (ATL-COM-99-044).

[62] V. Blobel. Unfolding methods in high-energy physics experiments. Lectures given at 1984 CERN School of Computing, Aiguablava, Spain, Sep 9-22, 1984.

[63] G. Cowan. A survey of unfolding methods for particle physics. Prepared for Conference on Advanced Statistical Techniques in Particle Physics, Durham, England, 18-22 Mar 2002.

[64] I. Borjanovic et al. Investigation of top mass measurements with the ATLAS detector at LHC, 2004. ATLAS Scientific Note (SN-ATLAS-2004-040), hep-ex/0403021.

[65] R. Sturrock et al. A step towards a computing grid for the LHC experiments: ATLAS Data Challenge 1. CERN-PH-EP-2004-028.

[66] F. K. Martens. Top physics capabilities at the LHC. *Nucl. Phys. Proc. Suppl.*, 142:416–419, 2005.